HOKKAIDO UNIVERSITY

Title	First-principle Molecular Simulations of Vibrational Spectroscopy and Reaction Dynamics in Noble-gas Matrix Environments: Noble-gas Compounds and Photodissociation Dynamics
Author(s)	新見, 佳祐
Citation	北海道大学. 博士(理学) 甲第11920号
Issue Date	2015-03-25
DOI	10.14943/doctoral.k11920
Doc URL	http://hdl.handle.net/2115/63043
Type	theses (doctoral)
File Information	Keisuke_Niimi.pdf

Instructions for use

Hokkaido University Collection of Scholarly and Academic Papers : HUSCAP

First-principle Molecular Simulations of Vibrational Spectroscopy and Reaction Dynamics in Noble-gas Matrix Environments: Noble-gas Compounds and Photodissociation Dynamics

（マトリックス効果を考慮した振動と反応の第一原理シミュレーション：
希ガス化合物の振動分光と蟻酸の光解離反応への適用）

Keisuke Niimi

Graduate School of Chemical Sciences and Engineering
Hokkaido University

March 2015

Contents

1. General Introduction **1**

1-1. Matrix isolation spectroscopy 1

1-2. Conformation memory 7

1-3. Purpose 9

1-4. Overviews of thesis 10

1-5. References 11

2. Theoretical method **15**

2-1. Born-Oppenheimer approximation 15

2-2. Vibrational Schrödinger equations 17

2-2-1. One-dimensional harmonic approximations 17

2-2-2. Multi-dimensional harmonic approximations 19

2-2-3. Discrete variable representations methods (DVR) 23

2-2-4. Potential-optimized discrete variable representations methods (PO-DVR) 25

2-3. Molecular Simulation methods 26

2-3-1. Markov chain Monte Carlo methods (MCMC) 26

2-3-2. Multiple Markov chain Monte Carlo methods (Multi-MCMC) 29

2-4 References 30

3. Competing effects of rare gas atoms in matrix isolation spectroscopy: A case study of vibrational shift of BeO in Xe and Ar matrices **31**

3-1. Introduction 31

3-2. Simulation Methods 33

3-2-1. *Ab initio* calculations 36

3-2-2. Potential-Optimized DVR 37

3-2-3. Monte Carlo simulation 38

3-3. Results and Discussion 40

3-3-1. *Ab initio* calculations for BeO, XeBeO, and ArBeO 40

3-3-1. Potential energy surfaces for XeBeO-Xe, XeBeO-Ar, and ArBeO-Ar 42
3-3-2. Monte Carlo simulations for XeBeO-Xe$_N$, XeBeO-Ar$_N$, and ArBeO-Ar$_N$. 44
3-4. Conclusion 51
3-5. References 52

4. Vibrational Shifts of HXeCl in Matrix Environments 53
4-1. Introduction 53
4-2. Computational Details 55
4-2-1. *Ab initio* calculations 56
4-2-2. Potential-Optimized DVR and Monte Carlo simulation 58
4-3. Results and Discussion 60
4-3-1. Equilibrium structure and vibrational analysis of HXeCl 60
4-3-2. Potential energy surfaces and vibrational frequencies of HXeCl–Ng 61
4-3-3. Monte Carlo simulations for HXeCl–Ng$_N$ 66
4-4. Conclusion 76
4-5. References 77

5. Matrix Site Effects on Vibrational Frequencies of HXeCCH, HXeBr, HXeI, and HXeH: A Hybrid Quantum-Classical Simulation 79
5-1. Introduction 79
5-2. Computational Details 82
5-3. Results and Discussion 86
5-3-1. Equilibrium Structures and Vibrational Analysis of HXeCCH, HXeBr, and HXeI 86
5-3-2. Equilibrium Structures and Vibrational Analysis of HXeCCH–Ng, HXeBr–Ng, and HXeI–Ng (Ng = Ne, Ar, Kr, Xe) 89
5-3-3. Hybrid Quantum-Classical Simulations of Vibrational Spectroscopy in Matrix Environments 97
5-4. Conclusions and Outlook 103
5-5. References 103

6. HXeI and HXeH in Ar, Kr, and Xe Matrices: A Hybrid Quantum-Classical Simulation 111
6-1. Introduction 107
6-2. Computational Details 109

6-3. Results and Discussion 113
6-3-1. HXeY monomers and the HXeY···Ng complexes (Y = I and H; Ng = Ar, Kr, and Xe) 113
6-3-2. HXeI and HXeH in Matrix Environments 119
6-4. Conclusion 122
6-5. References 125

7. QM/MM-MD study on conformation memory in 193 nm photolysis of formic acid: Excited-state dynamics controlled by the initial electronic state and the cage effect 127

7-1. Introduction 127
7-2. Computational details 127
7-2-1. Determination of the Morse potential parameters for QM/MM simulations 130
7-2-2. Dynamics Simulations 132
7-3. Results and discussion 135
7-3-1. S_0-QM/MM-MD simulations for *cis*-HCOOH and *trans*-HCOOH 135
7-3-2. S_2- MD simulations for *cis*-HCOOH 137
7-3-3. The ratio of CO/CO_2 145
7-4. Conclusions 147
7-5. Reference 148

8. General Conclusions 151

1. General Introduction

1-1. Matrix isolation spectroscopy

Spectroscopy is the study of the interaction between electromagnetic radiation and matter [1,2]. Spectroscopic measurements provide scientists valuable information about the properties of matters and they are frequently used for the identification of unknown materials. The experimental techniques in spectroscopy are roughly categorized into the infrared (IR) [3], ultraviolet-visible (UV/Vis) [4] and nuclear magnetic resonance (NMR) [5,6], depending on the wavelength of the radiation light, and the irradiation on molecules leads to electronic excitations, vibrational excitations, nuclear spin orientations, etc.

The IR spectroscopy is a particularly important tool in the area of analytical chemistry because its measurement causes no damage on a target molecule, and any special preparation is not required before the measurements [7]. However, perturbations originating from the surrounding environments sometimes contaminate the spectra, and therefore the precise assignments of the observed peaks become difficult tasks.

As a technique for preparing the "ideal" sample, *matrix isolation* method has been proposed [8-13]. In this method, a target compound is diluted into the inert gases (usually, noble-gases) and the measurements are performed at a very low temperature. The initial purpose of the matrix isolation technique was to try to measure the spectrum of unstable species, such as reaction transients or radicals by exploiting the feature that the lifetimes of such unstable compounds are prolonged under the environment of noble gas solids [10-12]. Later, the application of matrix isolation method has been extended to measurements of stable molecules such as CO [14] or H_2O [15]. The advantage of the method is now being more appreciated, and the technique becomes a standard tool for studying stable molecules. The isolation of monomeric molecules in an inert environment reduces intermolecular interaction and rotation, leading to a sharp peak in

the absorption spectrum, in contrast to the situation in other condensed phases environments [13]. This matrix isolation technique now finds the wide applicability in most of the fields in spectroscopy, particularly in IR, UV, and ESR.

It has been recognized for long time that the vibrational shifts due to the matrix environments exist to some extent, but these effects are assumed to be very small. In fact, it has not been paid much attention thus far. There is a book that compiles a large amount of data about experimental vibrational and electronic energy levels of polyatomic transient molecules [16]. Here I quote the following sentences and also figures from this book about the matrix shifts.

"Matrix shifts for covalently bonded molecules trapped in solid neon or argon often are quite small. Figure1 compares the observed matrix shifts for the ground-state fundamental vibrations of transient molecules trapped in solid neon and argon. For neon matrices, the maximum in the distribution lies near 0.0%, and for argon matrices, near 0.2%. For both neon and argon matrices, fewer than one-tenth of the matrix shifts are greater than 1%."

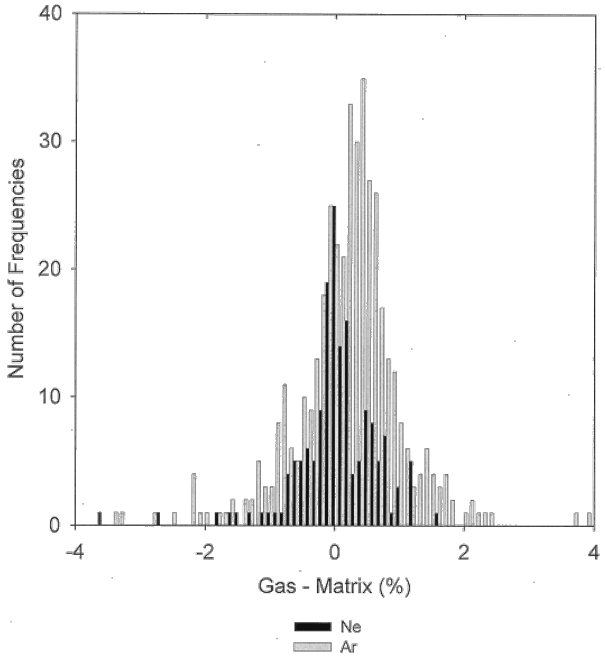

Figure 1. *Comparison of ground-state vibrational frequencies reported for transient molecules (2-16 atoms) in neon and argon matrices with corresponding values obtained from gas-phase measurements* [16].

Some molecules such as small hydrides or polarized molecules, however, do not follow the tendency pointed out above. These molecules are expected to show the nonnegligible shifts in matrix-isolation spectroscopy (see chap. 4.2.9 in ref. 13), but the reasons for these shifts have not been understood, because most experimentalists believed that the matrix shifts in these molecules are exceptional. However, with the accumulation of spectroscopic data of unstable molecules, the necessity for understanding matrix shifts has emerged. Furthermore, there has been a notable growth in the area of noble-gas chemistry [17-20], which will be described below and much attention has been paid to the matrix shifts.

Noble-gas elements, belonging to group 18 in the periodic table are chemically inactive because they enjoy the dominant stability expected from the concept of "octet valence configuration". Therefore, it had been widely and blindly believed that they cannot form any chemical bonding. However, in 1933, Pauling predicted the existence of XeF_6 and KrF_6, led by the intuition that noble-gas atoms might be chemically activated in powerfully oxidizing condition, such as under fluoride environment [21]. In 1962, nearly thirty years after the prediction by Pauling, Bartlett succeeded in synthesizing $Xe^{+}[PtF_6]^{-}$, which became the first real compound of the noble-gas atom. This breakthrough had prompted the further searching for the new noble-gas compounds, and the noble-gas chemistry had gradually developed to be one of disciplines in chemical sciences and now have covered from the problem of "missing xenon" in the earth atmosphere [23,24] to the usage of compounds as the storage of noble gases in a dense form [25].

For the first few decades since 1962, most of the newly discovered noble-gas compounds had been limited to relatively heavier noble-gas atoms like Kr and Xe [17, 18]. In these compounds, the bonding mainly originates from ionic interactions. In order to attract noble-gas atoms, very electronegative groups are needed. Actually, most of these noble-gas compounds have the bonding to fluorine or fluorine-containing groups.

The second breakthrough in noble-gas chemistry was the discovery of

noble-gas hydrides, with a common formula HNgY, where Ng is a noble-gas atom and Y is an electronegative fragment. As a family of noble-gas hydrides, Khriachtchev et al. reported the synthesis of HArF in 2000, the first neutral Ar compound [26]. A bonding motif of noble-gas hydrides is quite unique and different from the previous noble-gas compounds. It is represented in the form $(H\text{-}Ng)^{+}Y^{-}$, where $(H\text{-}Ng)^{+}$ is the covalent bond while the binding between $(H\text{-}Ng)^{+}$ and Y^{-} is ionic. Its stability comes from this bonding mechanism, where the energetic disadvantage of the ionization of Ng by the affinity of Y^{-} is compensated by the formation of covalent bond by sharing each unpaired electron from Ng and H. Since the discovery of HArF, the search for novel noble-gas hydrides has been carried out. Until now, over 20 members have already been discovered, including noble-gas organic compounds like HXeCCH [20, 27-29].

Through the search for new noble-gas compounds, quantum chemical calculations play an important role. The data obtained by quantum chemical calculations provide the valuable information about properties of already-known noble-gas compounds, but also it helps to predict the existence of new ones. For example, when NgBeO (Ng = Ar, Kr, Xe) was firstly identified in matrix-isolated IR spectroscopy [30], it had already been predicted by quantum chemical calculations [31]. As a recent case, several groups have discussed the possibility of helium complexes, and theoretical calculations predicted that HHeF is stable, although it is not experimentally prepared yet [20, 32-34].

Recently, there have been more reports on matrix-isolation spectroscopy for noble-gas hydrides. Noble-gas hydrides are synthesized in matrix environments. For example, HXeI is produced by irradiation of ultraviolet light to HI diluted in Xe matrix. HI is radicalized into H + I, followed by the neutral reaction channel of H + Xe + I → HXeI [35-37]. For the identification of the products, IR measurement is usually carried out. However, due to its unique bonding character (relatively weak bonding and large dipole moments), the molecule experiences strong effects from the surrounding noble-gas matrix. When the H-Xe stretching vibrational frequency is measured in matrix-isolated IR spectroscopy, the observed values in Xe, Kr and Ar are 1193 cm^{-1}, 1239 cm^{-1} and 1238 cm^{-1}, respectively. The differences in frequencies among noble-gas matrices are relatively large, which implies the large frequency shifts from

the gas phase values. This kind of matrix shifts is generally found in other noble-gas hydrides, which makes the reliable spectroscopy measurements difficult.

Additionally, it has been also reported that noble-gas compounds can be unexpectedly formed in the noble-gas matrix. Ono et al. preformed *ab initio* calculations of the bending vibrational frequency of NiCO and compared with the experimental values measured in Ar matrix (409.1 cm^{-1}) [38]. They found that the calculated frequencies are 361.1 and 403.5 cm^{-1} for NiCO and Ar−NiCO, respectively, and the value for Ar−NiCO is much closer to the experimental one. They pointed out that the binding between Ar and NiCO is stronger than a typical Van der Waals force, which implies that NiCO is likely to exist as Ar−NiCO in Ar matrix. The possibility of the formation of noble-gas compounds in matrix environments had not been considered at that time. They also performed *ab initio* calculations for NiN_2 and CoCO and reached the similar conclusions. Based on that, they suggested to check carefully again the spectroscopic data of the transition metal compounds in matrix-isolation method and, if necessary, to correct these data by taking into account the effects of chemical bonding with noble-gas atoms.

In accordance with the development of noble-gas chemistry, the applicability of matrix isolation technique has been expanding. It is very advantageous that the obtained spectrum becomes clear and the assignments of the peaks become easy. Currently, the spectroscopic data of many kinds of molecules are accumulated as a database. Noble-gas matrix isolation is originally based on a preconceived idea: noble-gas atoms are inert enough to have no influence on the target molecule. However, this assumption was questioned because of successive discoveries of noble-gas compounds and a number of papers appear reporting the mismatches between calculations and experiments. Therefore, there has been much demand from experimentalists involved in the matrix-isolation spectroscopy to provide a quantitative estimation of the matrix effects. Theoretical calculations are now strongly desired.

Theoretical works investigating the influence of the matrix environments are relatively scarce. The estimation of the vibrational shifts by placing two or three noble-gas atoms around the target molecule might not provide a clear picture of the

matrix shifts. As detailed from Chapter 3 to Chapter 5, it will be clear that the accumulation of forces coming from myriads of noble-gas atoms can only account for the substantial shift. Also, it will be shown that the morphology around the target molecule formed by noble-gas atoms is an important factor affecting the vibrational shifts. As shown in this thesis, the precise modeling incorporating the thermal motion of thousands of noble-gas atoms is necessary to reproduce the matrix shift. There have been very little theoretical works to estimate the vibrational frequencies considering such effects. If such a theoretical tool is available, it will be very beneficial, especially for researchers involved in the spectroscopic measurements. It will be of great help to predict the "true" vibrational frequency even for an unstable molecule that exits only in matrix environments.

1-2. Conformation memory

From the successful discoveries of unique noble-gas hydrides, photodissociation reactions using the matrix-isolation techniques have been investigated for different kinds of molecules [39-45]. Some of these experiments exhibit curious reactions, where photo-products obtained in noble-gas matrix are significantly different from those in the gas phase. For example, by the irradiation of UV light (193 nm) a formamid dissociates into the dominant product of NH_3 + CO in the gas phase. However, the major product is HNCO + H_2 in Xe matrix [41]. As an important factor affecting the photo-products in different noble-gas environments, "cage effect" is suggested [46]. As an another example, when *trans*-HCOOH is irradiated at 193nm inside Xe, Kr and Ar matrices, the dominant product is CO_2 + H_2 in Xe matrix, while it is CO + H_2O in Kr and Ar matrices [47]. It is noted that HCO + OH is observed as the major product in the gas phase [48].

In addition, there is another peculiar phenomenon under noble-gas matrix environments, which was observed in the photodissociation of HCOOH in Ar matrix [40]. The isomerization from *trans*-isomer, which is the most stable conformer, to *cis*-isomer is achieved by combining IR vibrational excitation with the matrix-isolated method [49]. After the irradiation of UV light at 193 nm, the dominant channel was CO + H_2O for *trans*-isomer, while it was CO_2 + H_2 for *cis*-isomer. The CO/CO_2 branching ratios were 5.0 and 0.42 for *trans*-isomer and *cis*-isomer, respectively. Such an observation depends heavily on initial conformers and this property is called "conformation memory". However, the experimental evidence of conformational selective reactions is limited, because in most cases the isomerization barrier is much lower than the photo-excitation energy or barrier for chemical transformations. Nevertheless, conformationally specific photodissociation dynamics has been recently discovered in some systems, such as 1-iodopropane cation ($1\text{-}C_3H_7I^+$) [50] and propanal cation ($C_3H_6O^+$) [51-53]. Theoretical calculations, such as reaction path analysis approach or dynamics simulations, have revealed the mechanisms of conformationally selective reactions by investigating the landscape of the excited-state potential energy surfaces. However, the photodissociation mechanisms in matrix environments have not been elucidated adequately. After reviewing the theoretical approach for investigating the photolysis

in matrix environments, I examine the cage effect on the conformational selectivity. In this thesis, the origin of conformational memory for HCOOH in Ar matrix is investigated by the excited-state quantum mechanics/molecular mechanics (QM/MM) molecular dynamics (MD) simulations.

1-3. Purpose

The purpose of this thesis is to clarify the effects of noble-gas matrices on vibrational spectroscopy and photodissociation dynamics.

As for the vibrational spectroscopy, I have developed a novel tool to calculate the vibrational frequencies of the embedded molecule under the influence of the surrounding noble-gas atoms. I have applied this method to several noble-gas compounds where the prominent vibrational shifts are observed in matrices. Specifically, I have investigated the following noble-gas compounds: XeBeO, ArBeO, HXeCl, HXeBr, HXeI, HXeCCH and HXeH. My method is based on the theory of vibrational frequency calculations and also on the numerical methods of molecular simulations. In order to obtain accurate vibrational frequencies, I have adopted discrete variable representation (DVR) method, which includes the anharmonicity and also coupling between different vibrational modes. I have also employed the Markov chain Monte Carlo (MCMC) method for efficiently sampling the configuration space of the system composed of hundreds of noble-gas atoms.

As for the photodissociation dynamics in matrix environments, I have performed the excited-state QM/MM-MD simulation for the formic acid in Ar matrix. In particular, I have examined the dissociation path of *cis*-isomer starting from the S_2 state. Transitions between electronic states is described by the trajectory surface hopping (TSH) method and the excited-state potential energies are evaluated at the multi-state complete active space second-order perturbation theory (MS-CASPT2) level. To the best of my knowledge, this work provides the first decisive answer for the origin of the conformational memory in the photodissociation dynamics of two HCOOH isomers in Ar matrix.

1-4. Overviews of thesis

This thesis is organized as follows. The basic theory of the theoretical approach is presented in Chapter 2. In particular, the focus is on the molecular vibrational theory and the numerical techniques of molecular simulations. From Chapter 3 to Chapter 6, the various applications are described. The vibrational shift of BeO in Xe and Ar matrices is discussed in Chapter 3. In Chapter 4, the unique tendency of the vibrational shifts of H-Xe stretching motion in HXeCl in different noble-gas matrices is discussed. In Chapter 5, I extend to the other members of noble-gas hydrides: HXeI, HXeBr and HXeCCH and summarize matrix shifts observed for the noble-gas hydrides. In Chapter 6, I applied for HXeH and HXeI in the similar approach and compared the experimental results for them. In Chapter 7, I perform the excited-state QM/MM-MD simulation of photodissociation dynamics of HCOOH in Ar matrix. Starting from *cis*-HCOOH in the S_2 state, I discuss the origin of conformational memory. In Chapter 8, summary and outlook of the present work are presented.

1-5. References

1. G. R. Kirchhoff, Untersuchungen über das Sonnenspectrum und die Spectren der chemischen Elemente (1859)
2. R. W. Bunsen and G. R. Kirchhoff, Chemische Analyse durch Spectralbeobachtung (1860)
3. W. W. Coblentz, *Investigations of Infra-Red Spectra*, (Carnegie Institution of Washington, Washington, D.C. , 1905)
4. I. R. Altemose, *J. Chem. Educ*. **63**, A216 (1986)
5. F. Block, W. W. Hansen and M. E. Packard, *Phys. Rev.* **69**, 127 (1946)
6. E. M. Purcell, H. C. Torrey and R. V. Pound. Phys. Rev. **69**, 127 (1946)
7. B. C. Smith. *Fundamentals of Fourier Transform Infrared Spectroscopy, Second Edition* (CRC Press, New York, 2011)
8. G. N. Lewis, D. Lipkin and T. T. Magel, *J. Amer. Chem. Soc.* **63**, 3005 (1941)
9. G. N. Lewis and D Lipkin, *J. Amer. Chem. Soc.* **64**, 2801 (1942)
10. I. Norman and G. Porter, *Nature* **174**, 508 (1954)
11. E. Whittle, D. A. Dows and G. C. Pimentel, *J. Chem. Phys.*, **22** 1943 (1954)
12. E. D. Becker and G. C. Pimentel, J. Chem. Phys. **25**, 244 (1956)
13. H. E. Hallam (Ed.), *Vibrational Spectroscopy of Trapped Species*, Wiley (1973)
14. G. E. Leroi, G. E. Ewing and G. C. Pimentel, *J. Chem. Phys.* **40**, 2298 (1964)
15. M. Van Thiel, E. D. Becker and G. C. Pimentel, *J. Chem Phys.* **27**, 486 (1957)
16. Marilyn E. Jacox, *Vibrational and Electronic Energy Levels of Polyatomic Transient Molecules* (http://webbook.nist.gov/chemistry/polyatom/)
17. W. Grochala., *Chem. Soc. Rev.* **36**, 1632 (2007)
18. K. O. Christe, *Angew. Chem., Int. Ed.* **40**, 1419 (2001)
19. M. Zhou, L. Andrews, C. W. Bauschlicher, *Chem. Rev*. **101**, 1931 (2001)
20. Khriachtchev, M. Räsänen, and R. B. Gerber, *Acc. Chem. Res*. **42**, 183 (2009).
21. L. Pauling, *J. Am. Chem. Soc.* **55**, 1895 (1933)
22. N. Bartlett, Proc. Chem. Soc. **218** (1962)
23. W. A. Caldwell, J. H. Nguyen, B. G. Pfrommer, F. Mauri, S. G. Louie and R. Jeanloz, *Science* **277**, 930 (1997)

24. C. Sanloup, B. C. Schmidt, E. M. C. Perez, A. Jambon, E. Gregoryanz and M. Mezouar, *Science* **310**, 1174 (2005)
25. G. D. Enright, K. A. Udachin, I. L. Moudrakovski and J. A. Ripmeester, *J. Am. Chem. Soc.* **125,** 9896 (2003)
26. L. Khriachtchev, M. Pettersson, N. Runeberg, J. Lundell and M. Räsänen, *Nature* **406**, 874 (2000).
27. V. I. Feldman, F. F. Sukhov, A. Y. Orlov and I. V. Tyuipina, *J. Am. Chem. Soc.* **125**, 4698 (2003)
28. H. Tanskanen, L. Khriachtchev, J. Lundell, H, Kiljunen and M. Räsänen, *J. Am.Chem. Soc.* **125**, 4696 (2003)
29. V. Poterya, O. Votava, M. Fárník, M. Oncák, P. Slavícek, U. Buck and B. Friedrich, *J. Chem. Phys.* **128**, 104313 (2008)
30. G. Frenking, W. Koch, J. Gauss, and D. Cremer, J. Am. Chem. Soc. **110**, 8007 (1988)
31. C. A. Thompson and L. Andrews, *J. Am. Chem. Soc.* **116**, 423 (1994)
32. G M. Chaban, J. Lundell and R. B. Gerber, *J. Chem. Phys*. **115,** 7341 (2001)
33. T. Takayanagi and A. Wada, *Chem. Phys. Lett.* **352,** 91 (2002)
34. A. Lignell, L. Khriachtchev, M. Pettersson and M. Räsänen, *Chem. Phys.* Lett. **390**, 256 (2004)
35. M. Pettersson, J. Lundell and M. Räsänen, *J. Chem. Phys.* **102**, 6423 (1995)
36. M. Pettersson, J. Nieminen, L. Khriachtchev and M. Räsänen*, Chem. Phys.* **107**, 8423 (1997)
37. J. Lundell, M. Pettersson, L. Khriachtchev, M. Räsänen, G. M. Chaban, R. B. Gerber, *Chem. Phys. Lett*. **322**, 389 (2000)
38. Y. Ono and T. Taketsugu, *Monatshefte für Chemie - Chemical Monthly* **136**, 1087, (2005)
39. M. J. Almond and N. Goldberg, *Annu. Rep. Prog. Chem., Sect. C: Phys. Chem.* **103**, 79 (2007)
40. L. Khriachtchev, E. Mocoas, M. Pettersson, M. Räsänen, *J. Am. Chem. Soc.* **124,** 10994 (2002)
41. J. Lundell, M. Krajewska and M. Räsänen, *Phys. Chem. A* **102**, 6643 (1998)
42. H. M. Knuttu and J. A. Seetula, *Phys. Chem. Chem. Phys.* **189,** 273 (1994)
43. E. T. Ryan and E. Weitz,*J. Chem. Phys.* **99,** 1004 (1993)

44. F. T. Prochaska and L. Andrews, *J. Chem. Phys.* **67**, 1091 (1977)
45. M. Sałdyka and Z. Mielke, *Phys. Chem. Chem. Phys.* **5**, 4790 (2003)
46. M. Eckert-Maksic, M. Vazdar, M. Ruckenbauer, M. Barbatti, T. Muller and H. Lischka, *Phys. Chem. Chem. Phys*. **12,** 12719 (2010)
47. I. Lundell and M. Räsänen, *J. Mol. Struct.* **349**, 436 (1997)
48. R. S. Irwin, D. L. Singleton, G. Paraskevopoulos and R. McLaren, *Int. J. Chem. Kinet.* **26,** 219 (1994)
49. M. Pettersson, J. Lundell, L. Khriachtchev and M. Räsänen, *J. Am. Chem. Soc.* **119,** 11715 (1997)
50. S. T. Park, S. K. Kim and M. S. Kim, *Nature*, **415,** 306 (2002)
51. M. H. Kim, L. Shen, H. L. Tao, T. J. Martinez and A. G. Suits, *Science* **315,** 1561 (2007)
52. P. C. Singh, L. Shen, M. H. Kim and A. G. Suits*, Chem. Sci.* **1** 552, (2010)
53. H. L. Tao, L. Shen, M. H. Kim, A. G. Suits and T. J. Martinez, *J. Chem. Phys.* **134,** 054313 (2011)

2. Theoretical method

2-1. Born-Oppenheimer approximation [1]

In quantum chemistry, Schrödinger equation is used to govern the movements of electrons and nucleus correctly. However, in trying to solve them, treating two different particles on an equal footing is terribly unreasonable. Accordingly, Born-Oppenheimer approximation comes as the first step to reduce the difficulties in solving Schrödinger equations. It introduces the separation of movements of electrons from that of nucleus on the ground that nucleus are much heavier than electrons. Therefore, the nucleuses are regarded being stationary in the space from the view of electrons. Hence, the Hamiltonian and Schrödinger equation for electrons is written like the below.

$$H_e = -\sum_{i=1}^{N_e} \frac{1}{2m_e} \nabla_i^2 + \frac{e^2}{4\pi\varepsilon_0^2} \left(\sum_{i=1}^{N_e} \sum_{j>i}^{N_e} \frac{1}{r_{ij}^2} + \sum_{i=1}^{N_e} \sum_{A=1}^{M} \frac{Z_A}{r_{iA}^2} + \sum_{i=1}^{M} \sum_{A=1}^{M} \frac{Z_A Z_B}{R_{AB}^2} \right) \qquad (1)$$

$$H_e \Phi_e = E_e \Phi_e \qquad (2)$$

In the above equation, N_e and M is the number of electrons and that of nuclei of the system, respectively. $r_{ij,}$ r_{iA} and R_{AB} is the distance between two electrons, that between an electron and a nucleus and that between two nuclei, respectively. m_e is the mass of electron. e and ε_0 represents elementary charge and permittivity of vacuum, respectively. Z_A exhibits atomic number of nucleus A. ∇^2 means the sum of the square of differentiation with respect to coordinates.

The above equations are solved for positions of electrons as variants and give the electronic energies E_e in the determined positions of nuclei as eigenvalues. The

wave function and the potential energy as the solutions for electronic Schrödinger equations depend parametrically on the nuclear coordinates, which leads to the interpretation the nuclei move on the potential energy surface.

Denoting the potential energy as the function following the nuclei positions as variables, $E_e(\mathbf{R})$, the Hamiltonian for nuclei is written like

$$H_{tot} = -\sum_{a=1}^{M} \frac{1}{2M_a} \nabla_i^2 + E_e(\mathbf{R}) \qquad (3)$$

The separation between the movement of electrons and that of nuclei in such a way is called Born-Oppenheimer approximation. This approximation is relatively good for almost all cases except for when two adjusted potential energy surfaces come close to each other.

Actually, the case you must solve the total Schrödinger equations (eq. 3) are limited. Many chemical processes are explained adequately by treating the movements of nuclei classically. However, quantum properties must be considered for the phenomena where the movements of light-atom like hydrogen matter, which is called tunneling process or the more common one where nuclei are tightly banded under the well-curved potential energy, which is vibration. The theory of vibration is discussed from the next chapter.

2-2. Vibrational Schrödinger equations

2-2-1. One-dimensional harmonic approximations [2]

I start to define the Hamiltonian of one-dimensional harmonic oscillator in classical mechanics with the coordinate ***x*** and its conjugate momentum ***p***.

$$H = \frac{p^2}{2\mu} + \frac{1}{2}\mu\omega x^2 \qquad (4)$$

This dynamical system can be looked as the movements of two mass points binding with each other through one spring and is the simplest model for the vibration of a diatomic molecule. μ and ω is reduced mass and ω angular frequency, respectively.
This dynamical system can be looked as the movements of two mass points connecting with each other through the spring and is the simplest model for the vibration of a diatomic molecule. μ is reduced mass and ω is angular frequency.

The quantization of the physical system can be accomplished by quantizing the physical quantities, which means, in this case, by corresponding physical quantities to physical operators such as $p \to -i\hbar\frac{\partial}{\partial x}$ and $x \to x$, the Hamiltonian (eq. 4) is rewritten like the following, to represent the quantum mechanics.

$$H = -\frac{\hbar^2}{2\mu}\frac{\partial^2}{\partial x^2} + \frac{1}{2}\mu\omega^2 x^2 \qquad (5)$$

Introducing mass-weighted coordinates($q \to \sqrt{\mu}x$), the Hamiltonian becomes simplified.

$$H = -\frac{\hbar^2}{2}\frac{\partial^2}{\partial q^2} + \frac{1}{2}\omega^2 q^2 \qquad (6)$$

When the Hamiltonian is given as (eq. 6), the Schrödinger equations can be solved analytically, which gives eigenvalue E and eigenfunction φ like the following.

$$\phi_n(q)=\left(\frac{1}{2^n n!}\right)^{\frac{1}{2}} H_n\left(\sqrt{\frac{\omega}{\hbar}}q\right)e^{-\frac{1}{2}\left(\sqrt{\frac{\omega}{\hbar}}q\right)^2} \qquad (7)$$

$$E_n=\hbar\omega\left(n+\frac{1}{2}\right) \qquad (8)$$

H_n is the Hermite polynomial and n is the vibration quantum number. When n is zero, it corresponds to the vibration ground state. When n is bigger than zero, it represents vibration excite state.

Particularly, the vibration energy in the ground state (n=0) is called the zero point energy, which is the least possible energy in the vibration. The vibration energy constantly must be bigger than zero point energy.

2-2-2. Multi-dimensional harmonic approximations [2]

I extend the discussion in the previous chapter to *N*-particles molecule. When the mass and position coordinate of *i*-th atom is set to M_i and (x_i, y_i, z_i), respectively, the kinetic energy of the molecule is represented as

$$T = \sum_{i=1}^{N} \frac{M_i}{2}\left(\dot{x}_i^2 + \dot{y}_i^2 + \dot{z}_i^2\right) \qquad (9).$$

By rewriting the expression of the mass and coordinates to more general forms,

$$\begin{aligned} \xi_{3i-2} = x_i,\ \xi_{3i-1} = y_i,\ \xi_{3i} = z_i \quad (i = 1 \ldots N) \\ m_{3i-2} = m_{3i-1} = m_{3i} = M_i \quad (i = 1 \ldots N) \end{aligned} \qquad (10)$$

the kinetic energy is represented simpler like the below.

$$T = \sum_{i=1}^{3N} \frac{m_i}{2}\dot{\xi}_i^2 \qquad (11)$$

On the other hand, potential energy term V can be described in the function of the general coordinates. It can be approximated into the polynomial function through Taylor expansion. If the molecule is assumed to be exist near the equilibrium, over third order terms is much small enough to be neglected. As a result, potential function may well be written like

$$V = \frac{1}{2}\sum_{i=1}^{3N}\sum_{j=1}^{3N}\left(\frac{\partial^2 V}{\partial\xi_i \partial\xi_j}\right)_e \xi_i \xi_j \qquad (12)$$

As the same reason as before, I introduce the mass weighted coordinates.

$$\eta_i = \sqrt{m_i}\,\xi_i \quad (i = 1 \ldots 3N) \qquad (13)$$

Finally, the Hamiltonian is written like the following.

$$H = T + V = \frac{1}{2}\sum_{i=1}^{3N}\dot{\eta}_i^2 + \frac{1}{2}\sum_{i=1}^{3N}\sum_{j=1}^{3N} c_{ij}\eta_i\eta_j \qquad (14)$$

$$c_{ij} = \frac{1}{\sqrt{m_i}\sqrt{m_j}}\left(\frac{\partial^2 V}{\partial\xi_i\partial\xi_j}\right)_e \qquad (15)$$

Here, the matrix C, each of whose elements is derived from the second differential coefficient of potential function is called Hessian matrix.

In order to transform the form of the Hamiltonian to get the analytical solution for the Schrödinger equation and get the intuitive interpretation toward the molecular vibration, I introduce the linier transformation of mass-weighted coordinates from the diagonalization of the matrix C.

$$CL = L\Lambda \qquad (16)$$

Λ is the diagonal matrix. For the diagonal elements, $\Lambda_{ii} = \omega_i^2$ are set.
Adopting the vector expression of mass-weighted coordinates,

$$\eta = \begin{pmatrix} \eta_1 \\ \eta_2 \\ \vdots \\ \eta_{3N} \end{pmatrix} \qquad (17)$$

the kinetic and potential term is expressed like the following.

$$T = \frac{1}{2}{}^t\dot{\eta}\dot{\eta} \qquad (18)$$

$$V = \frac{1}{2}{}^t\eta C\eta \qquad (19)$$

By substituting the transformed coordinates, which are obtained from multiplying the inverse matrix of the transformation matrix with the coordinates vector,

$$Q = L^{-1}\eta \qquad (20)$$

the kinetic and potential term is represented much simpler.

$$T = \frac{1}{2}{}^{t}\left(L\dot{Q}\right)\left(L\dot{Q}\right) = \frac{1}{2}{}^{t}\dot{Q}\left({}^{t}LL\right)\dot{Q} = \frac{1}{2}{}^{t}\dot{Q}\dot{Q} \qquad (21)$$

$$V = \frac{1}{2}{}^{t}\left(LQ\right)C\left(LQ\right) = \frac{1}{2}{}^{t}Q\left({}^{t}LCL\right)Q = \frac{1}{2}{}^{t}Q\Lambda Q \qquad (22)$$

$$H = \frac{1}{2}{}^{t}\dot{Q}\dot{Q} + \frac{1}{2}{}^{t}Q\Lambda Q = \sum_{i=1}^{3N}\left(\frac{1}{2}\dot{Q}_i^2 + \frac{1}{2}\omega_i^2 Q_i^2\right) \qquad (23)$$

The Hamiltonian is qunatitized in the similar way with the one-dimensional case by substituting through $Q_i \to Q_i$ and $\dot{Q}_i = P_i \to -i\hbar\frac{\partial}{\partial Q_i}$,

$$H = \sum_{i=1}^{3N}\left(-\frac{\hbar^2}{2}\frac{\partial}{\partial Q_i^2} + \frac{1}{2}\omega_i^2 Q_i^2\right) = \sum_{i=1}^{3N} H_i \qquad (24)$$

Consequently, it makes clear that the Hamiltonian for the movements of N nuclei is deformed to the summation of that of one-dimension harmonic oscillator by introducing the linear-transformed coordinates.

Therefore, the wave function and the total energy are obtained as the analytical solutions.

$$\phi_{\mathbf{n}}\left(Q\right) = \prod_{i=1}^{3N}\phi_{n_i}\left(Q_i\right) \quad \phi_{n_i}\left(Q_i\right) = \left(\frac{1}{2^{n_i}n_i!}\right)^{\frac{1}{2}} H_{n_i}\left(\sqrt{\frac{\omega_i}{\hbar}}Q_i\right)e^{-\frac{1}{2}\left(\sqrt{\frac{\omega_i}{\hbar}}Q_i\right)^2} \qquad (25)$$

$$E_{\mathbf{n}} = \sum_{i=1}^{3N} E_{n_i} \qquad E_{n_i} = \hbar\omega_i \left(n_i + \frac{1}{2} \right) \tag{26}$$

$$\mathbf{n} = \left(n_1, n_2, \ldots, n_{3N} \right) \tag{27}$$

In multi-dimensional case, the vibrational state is represented as the vector like (eq. 27). As same with the one-dimension, $\mathbf{n} = \mathbf{0}$ stands for the vibrational ground state. The transformed coordinates derived from the diagonalization of Hessian matrix are called normal mode coordinates.

Among 3N modes, they are categorized into 3 (3) translations, 3 (2) rotations and 3N-6 (3N-5) vibrations for nonlinear (linear) molecule.

2-2-3. Discrete variable representations methods (DVR) [3,4]

If you hope for more reliable descriptions for the vibration, that is, more accurate vibrational frequency values, it is necessary to include the anharmonicity beyond the previous approximations. The Schrödinger equations can be solved analytically for the harmonic potential. However, it can't for more general potential. In such a case, it is effective way to expand enough basis sets to represent the desirable wave function. Through this procedure, the problem to have a solution for Schrödinger equation is reduced to the one to obtain eigenvalues from Hamiltonian matrix.

First, we assume to use the N basis set to get the matrix representation for Hamiltonian. Normal mode is employed as coordinate system. When performing numerical calculations for every matrix element of the Hamiltonian H = T + V, it is the most computational demanding to calculate the integral of the potential energy term.

$$V_{jk} = \left\langle \varphi_j \middle| \hat{V} \middle| \varphi_k \right\rangle \qquad (28)$$

As a way to overcome this difficulty, it is proposed to use the eigenfunctions of coordinate operator x as basis sets, which makes the costly numerical calculation entirely unnecessary.

First, you are required to prepare for the eigenfunction given as the solution of the following eigenequation.

$$\hat{x}\left| \chi_\alpha \right\rangle = x_\alpha \left| \chi_\alpha \right\rangle \qquad (29)$$

Assuming $\left\{ \varphi_j(x) \right\}_{j=1}^{N}$ to be the primitive basis sets, eigenfunctios are written like

$$\chi_\alpha(x) = \sum_{j=1}^{N} \varphi_j(x) U_{j\alpha} \qquad (30)$$

Potential energy depends only on the structure of the molecule. i.e. position coordinates, and so the potential operator can be interpreted as the function of coordinates operator, which means $\hat{\mathrm{V}} = \mathrm{V}(\hat{\mathrm{x}})$. Therefore, by using (eq. 29), the matrix element of the

potential energy term is descripted in the simple form.

$$V_{\alpha\beta}^{DVR} = \left\langle \chi_\alpha \middle| V(\hat{x}) \middle| \chi_\beta \right\rangle = V\left(x_\beta\right)\left\langle \chi_\alpha \middle| \chi_\beta \right\rangle = V\left(x_\beta\right)\delta_{\alpha\beta} \qquad (31)$$

The above equation doesn't require the numerical calculation at all. The matrix element of the potential term corresponds to the potential energy value at the position given as the eigenvalue from (eq. 29).

Furthermore, the matrix elements for the kinetic energy are derived from the analytical calculation of the integral. As a result, the computational efficiency on the whole is fully improved.

In the applications in this paper, sinc functions are adopted as primitive basis sets.

$$\begin{gathered} \varphi_n(x) = \sqrt{\frac{2}{b-a}} \sin\left(\frac{n\pi(x-a)}{b-a}\right) \qquad n = 1,\ldots,N-1 \\ \varphi_n\left(x_0 \equiv a\right) = \varphi_n\left(x_N \equiv b\right) = 0; \end{gathered} \qquad (32)$$

In this case, the eigenvalues x of (eq. 29) become the equal-divided grids between two endpoints.

Finally, the matrix element for the Hamiltonian is written in the following equation (eq. 33).

$$H_{\alpha\beta}^{DVR} = \sum_{j=1}^{N} \frac{U_{j\alpha}^{*} U_{j\beta}}{2} \left(\frac{k\pi}{b-a}\right)^2 + V\left(x_\alpha\right)\delta_{\alpha\beta} \qquad (33)$$

2-2-4. Potential-optimized discrete variable representations methods (PO-DVR) [5]

The normal DVR method, which is explained in the last chapter, is well enough for the application of one-dimensional systems. However, when you think to apply for multi-dimensional systems, the problem occurs. The larger the degree of freedoms become, the exponentially larger the necessary number of grids becomes. This means the size of Hamiltonian matrix increases equally, which leads to much demanding in the diagonalization. In this application, because we must do DVR calculations a lot of times in Monte Carlo iterations, the size of Hamiltonian must be as small as possible.

The accuracy of vibration calculations as well as that of electronic state calculations greatly depends on the quality of basis sets. As a way to reduce computational cost while maintaining the precision, basis sets can be optimized by using the eigenfucntions of the referenced potential as basis sets.

$$H_{q_N}^{ref}\varphi_{q_N}^{PO}(x) = \varepsilon_{q_N}^{ref}\varphi_{q_N}^{PO}(x) \qquad (34)$$

This equations is solved by the normal-DVR method using the primitive basis sets and the wavefunctions for the reference potential are obtained. Among them, wavefuctions corresponding for the relatively higher states can be truncated because the interest is usually in the first or second excited state only. The number of truncations is determined based on the balance between the accuracy of the targeted frequency values and the efficiency of calculation.

By using the chosen basis sets, you can solve (eq. 29) and get the eigenfunctions for the coordinate operator $\chi_{q_N}^{PO}(x)$. Finally, employing these products $\chi_{q_1}^{PO}(x)\chi_{q_2}^{PO}(x)\ldots\chi_{q_N}^{PO}(x)$ as the basis sets for the original Hamiltonian, you can solve the Schrödinger equations in the same way with normal-DVR.

2-3. Molecular Simulation methods

2-3-1. Markov chain Monte Carlo methods (MCMC) [6]

The distribution function for canonical ensemble is equivalent to the Boltzmann one like

$$\rho(\mathbf{R}) = \frac{1}{Z}\exp\left(-\frac{V(\mathbf{R})}{k_B T}\right) \qquad (35)$$

Z, k_B and T means partition function, Boltzmann constant and the temperature, respectively. For example, the average value in this ensemble for the physical quantity A is represented like the following, using $\rho(\mathbf{R})$

$$\langle A \rangle = \int \rho(\mathbf{R}) A(\mathbf{R}) d\mathbf{R} \qquad (36)$$

When the targeted system is composed by N particles, (eq. 36) means the integration over the space of 3N degrees. If N is just about two-digit numbers, the calculation is too massive to be possible in the ordinary manner.

Instead of treating all possible positioning configurations in the space with equal importance, it is much more efficient to prior to consider the configurations with the higher likelihood. Consequently, the ensemble average of the quantity A is given as the arithmetic average of the value of A obtained at the configuration sampled following the probability generated from the distribution function $\rho(\mathbf{R})$.

$$\langle A \rangle = \frac{1}{M}\sum_{k=1}^{M} A(\mathbf{R}) \qquad (37)$$

Such sampling method is generally called “importance sampling”.

Here, there is one problem; how such probabilities can be defined from the distribution function? So, we assume M discrete states exist in the 3N dimensional space and the move between two states happens probabilistically. For example, such

transition probability from state i to state j is represented by $p_{ij}(=\{\mathbf{P}\}_{ij})$. It depends on the only two, the former and the latter states and isn't entirely affected from the history of the past path. Such stochastic process is called "Markov chain". Defining the set of probabilities for all possible states at the step n as the vector like ${}^t\mathbf{p}(n) =\{p_1(n),p_2(n),\ldots p_M(n)\}$, where $p_i(n)$ is the probability of state i, it can be represented by the product of the state vector at step n-1 and the transition probability matrix.

$$ {}^t\mathbf{p}(n) = {}^t\mathbf{p}(n-1)\mathbf{P} \qquad (38) $$

leads to,

$$ {}^t\mathbf{p}(n) = {}^t\mathbf{p}(0)\mathbf{P}^n \qquad (39) $$

Due to the nature of "Markov chain", as the chain continues($n\rightarrow\infty$), the information of the initial state will be vanished and the state distribution will converge to the constant one characterized by the transition probability matrix.

If the following detailed balanced condition shown in (eq. 40) is satisfied and the probability process is aperiodic and irreducible, the Markov chain convergence to the constant distributions is guaranteed.

$$ \Pi_j p_{ji} = \Pi_i p_{ij} \qquad (40) $$

Summing the equation (eq. 40) for all states,

$$ \begin{aligned} \sum_j \Pi_j p_{ji} &= \sum_j \Pi_i p_{ij} \\ &= \Pi_i \sum_j p_{ij} = \Pi_i \end{aligned} \qquad (41) $$

Because (eq. 41) stands for all states (i=1..M), it is rewritten in the matrix form like the below.

$$\Pi \mathbf{P} = \Pi \qquad (42)$$

This equation means that when performing the stochastic process represented by the transition probability matrix meeting the detailed balanced condition (eq. 41), this stochastic process will converge to the state distribution of Π.

However, the transition probability is not determined uniquely from the condition of (eq. 40). Here, we introduce the most famous method, "Metropolis algorisms". In this method, the transition probability is defined as

$$P_{ij} = \min\left[1, \frac{\Pi_j}{\Pi_i}\right] \qquad (43)$$

Because the targeted distribution given by eq. 35, the probability defined in (eq. 43) is evaluated in the following way.

$$P_{ij} = \min\left[1, \exp\left(-\frac{V(\mathbf{R}_j) - V(\mathbf{R}_i)}{k_B T}\right)\right] \qquad (44)$$

2-3-2. Multiple Markov chain Monte Carlo methods (Multi-MCMC) [7]

When the normal MCMC method is used in this application, attaining the convergence of ensemble is much difficult in terms of the efficiency of simulation because one burdensome DVR calculation must be performed in every step of iterations. This difficulty can be avoided by using the approximated potential when judging the acceptance over dozens of steps.

I assume to start from the configuration $\mathbf{R_i}$, to iterate the move for a certain number of steps following the distribution function of approximated potential $V_{AP}(\mathbf{R})$ and finally reach to the configuration $\mathbf{R_j}$. In such a case, the acceptance probability from $\mathbf{R_i}$ to $\mathbf{R_j}$ is based on the difference between the original potential and the approximate one.

$$P\left(\mathbf{R}_i \to \mathbf{R}_j\right) = \min\left[1, \exp\left[-\frac{1}{k_B T}\left\{\left(V\left(\mathbf{R}_j\right) - V_{AP}\left(\mathbf{R}_j\right)\right) - \left(V\left(\mathbf{R}_i\right) - V_{AP}\left(\mathbf{R}_i\right)\right)\right\}\right]\right] \qquad (45)$$

It is important to choose the approximate potential which satisfies two conditions it is close to the original and ones its calculation is an easy task, both of which enhance the efficiency of the whole simulation. In the application for my research, we choose the interaction potential between the frozen molecule and the surrounding noble gas atoms, which doesn't require DVR calculation, as the approximate one. As a result, even if the number of the iterated moves in the approximate potential performed every step original potential N_s is set to 100, 95% can be ensured as the acceptance ratio.

2-4. References

1. F. Jensen, Introduction to computational chemistry, Wiley (2006)
2. 山内薫, 『岩波講座現代化学への入門４　分子構造の決定』、岩波書店 (2002)
3. J. C. Light, I. P. Hamilton and J. V. Lill, *J. Chem. Phys*. **82**, 1400 (1985)
4. D. T. Colbert and W. H. Miller, *J. Chem. Phys.* **96**, 1982 (1992)
5. J. Echave, D. C. Clary, *Chem. Phys. Lett.* **190,** 225 (1992)
6. R. Q. Topper et al, *Reviews in Computational Chemistry,* **19,** 1 (2003)
7. L. D. Gelb, *J. Chem. Phys.* **118**, 7747 (2003)

3. Competing effects of rare gas atoms in matrix isolation spectroscopy: A case study of vibrational shift of BeO in Xe and Ar matrices

3-1. Introduction

Matrix isolation spectroscopy is a powerful tool to measure various properties of chemical species by isolating them in an ideal condition for spectroscopic measurements, and therefore sometimes it allows us to obtain valuable information even on unstable molecules.[1] Since these spectra are usually obtained at very low temperatures, they are almost free from perturbations due to thermal fluctuations, thus enabling one to perform highly precise measurements. Rare gas atoms are almost exclusively used as a matrix medium, and since they are chemically inert, it is naturally assumed that the effect of surrounding rare gas atoms is marginal and in fact spectral shifts due to the presence of rare gas atoms are typically less than 0.5 %.

However, there have been several studies which reported that the rare gas atoms can form chemical complexes with some molecules, [2-4] and in some cases their interactions are strong enough that they are regarded as more like chemical compounds. In these situations, nonnegligible spectral shifts are observed upon formation of rare gas complexes, and it is necessary to take into account this shifts when analyzing the spectroscopic data if obtained in matrix environments.

Beryllium oxide (BeO) has long been studied in this context since it is known to form chemical complexes with rare gas atoms (Rg = Ar, Kr, Xe) [5]. When the

RgBeO complex is formed, the blue-shift in vibrational spectrum is observed. [6] Veldcamp and Frenking performed *ab initio* calculations on these complexes and found that charge-induced dipole interaction is the source of these complex formation. [7] They reproduced the vibrational shift to higher wave number observed in the experiments. In their calculations, the shifts upon formation of XeBeO and ArBeO were estimated to be 110 cm^{-1} and 122 cm^{-1}, respectively. However, the shift in XeBeO (ArBeO) complex is larger than that observed in the Xe (Ar) matrix experiments[8], which was about 34 (62) cm^{-1}, and it is anticipated that the effect of surrounding media may not be negligible. At the best of my knowledge, there is no report which investigates the effects of surrounding rare gas atoms on vibrational shifts for these complexes quantitatively. The spectroscopic data obtained experimentally for BeO and RgBeO in various rare gas matrices are tabulated in Table I.

In this paper, I investigate the vibrational shift of BeO in Xe matrix as well as in Ar matrix environments with mixed quantum-classical simulation and examine the origin of spectral shift in details from the viewpoints of complex-formation and perturbations from surrounding atoms. In particular, I examine the vibrational shift of XeBeO in Xe and Ar matrices and ArBeO in Ar matrix, where the experimental data are available.

Table I. Vibrational frequency (in cm^{-1}) of Be-O stretching motion of RgBeO complexes observed in various rare gas matrices.

	BeO	ArBeO	KrBeO	XeBeO
gas phase	1464[a]	—	—	—
in Ar matrix	—	1526[b]	1522[b]	1517[b]
in Kr matrix	—	—	1512[c]	—
in Xe matrix	—	—	—	1498[c]

[a]Reference [9], [b]Reference [6], [c]Reference [8]

3-2. Simulation Methods

In this section I briefly describe the simulation method used to obtain the vibrational spectra of a target molecule in rare gas matrix environments. The total system is divided into quantum and classical parts, where the quantum part consists of the target molecule represented by N_q normal coordinates while the classical part is composed of N rare gas atoms. The hybrid quantum-classical Hamiltonian of the whole system is then assumed to have the following pairwise-additive form:

$$H = \sum_{i=1}^{N_q} \frac{1}{2} \hat{p}_i^2 + \sum_{i=1}^{N} \frac{1}{2} \mathbf{P}^{(i)} + V_{\text{qm}}(\hat{\mathbf{q}}) + \sum_{i=1}^{N} V_{\text{qm-Rg}}(\hat{\mathbf{q}}, \mathbf{R}^{(i)}) + \sum_{i<j}^{N} V_{\text{Rg-Rg}}(|\mathbf{R}^{(i)} - \mathbf{R}^{(j)}|) \qquad (1)$$

where $\hat{\mathbf{q}} = \{\hat{q}_i; i = 1, \text{K}, N_q\}$ and $\hat{\mathbf{p}} = \{\hat{p}_i; i = 1, \text{K}, N_q\}$ represent the normal coordinates and their conjugate momenta of the target molecule, respectively. $\mathbf{R} = \{\mathbf{R}^{(i)}; i = 1, \text{K}, N\}$ and $\mathbf{P} = \{\mathbf{P}^{(i)}; i = 1, \text{K}, N\}$ are the coordinates and momenta of rare gas atoms, respectively. Here the center-of-mass and rotational motions of the molecule are treated classically and they are not included in the above Hamiltonian. In this work, vibrational-rotational coupling is neglected. $V_{\text{qm-Rg}}$ is the interaction potential between the molecule and rare gas atoms and it is obtained from the high-level *ab initio* calculations described below. $V_{\text{Rg-Rg}}$ is an interaction potential of rare gas atoms and this part is also determined by *ab initio* calculations.

The target molecule, which is treated quantum mechanically, is first set as a BeO molecule and the validity of the above pairwise-additive form to describe the total potential is examined in the case of BeO-Xe_N complexes. The BeO-Xe interaction potential is obtained by *ab initio* calculations, which will be described below, with BeO distance fixed at an equilibrium value, and the two-dimensional contour plot of the potential energy surface for BeO-Xe is shown in Figure 1. As seen in the figure, there is a deep minimum on the Be side in collinear geometry, which has a binding energy of 19.65 kcal/mol. When I employ the following pairwise-additive form for the potential of a BeO-Xe_2 complex,

$$V_{\text{BeO-Xe}}(\mathbf{R}^{(1)}) + V_{\text{BeO-Xe}}(\mathbf{R}^{(2)}) + V_{\text{Xe-Xe}}(|\mathbf{R}^{(1)} - \mathbf{R}^{(2)}|) \quad (2)$$

the minimum energy structure becomes Y-shaped, where two Xe atoms are equidistant from the Be atom as shown in Figure 2 and the total interaction energy is estimated to be 29.14 kcal/mol. *Ab initio* calculation predicts the interaction energy of 20.17 kcal/mol for this Y-shaped configuration and it is far different from the energy given by eq. (2). On the other hand, for the collinear configuration, which is determined by the *ab initio* method as a local minimum structure, the interaction energies are calculated to be 20.12 and 20.56 kcal/mol by the pairwise-additive form and *ab initio* method, respectively, and they agree well with each other (see also
Figure **2**). As can be apparently seen from the energies of the Y-shaped structure, potential energy defined by eq. (2) is not appropriate to represent the interaction for BeO-Xe_N complexes.

From these results, it is found that the electronic structure of the Xe atom that is bound to the Be atom is strongly perturbed by the BeO molecule and a stable chemical complex XeBeO is formed, as was predicted in the previous work.[6] The electronic structure of the Xe atom in this complex would be very different from the other surrounding Xe atoms. Similar observations are seen for BeO-Ar_2, and therefore I set the XeBeO (or ArBeO) complex as a QM part in this simulation and the total potential energy term for the RgBeO-Rg_N complexes is represented as

$$V_{\text{RgBeO}}(\hat{\mathbf{q}}) + \sum_{i=1}^{N} V_{\text{RgBeO-Rg}}(\hat{\mathbf{q}}, \mathbf{R}^{(i)}) + \sum_{i<j}^{N} V_{\text{Rg-Rg}}(|\mathbf{R}^{(i)} - \mathbf{R}^{(j)}|) \quad (3)$$

The validity of the above expression will be examined in the next section.

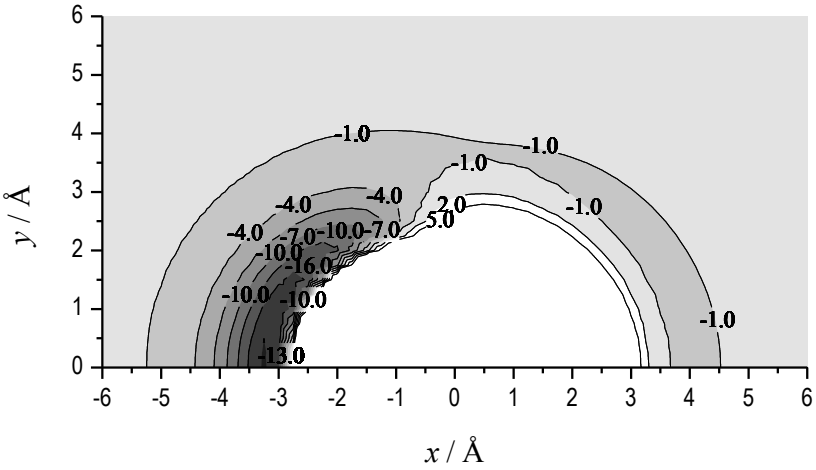

Figure 1. Two-dimensional contour plot of the potential energy surface (in units of kcal/mol) for BeO-Xe. The internal coordinates of BeO are fixed at the equilibrium values and the origin is set to the center-of-mass of BeO. The positions of Be and O are (−0.85, 0.0) and (0.48, 0.0), respectively.

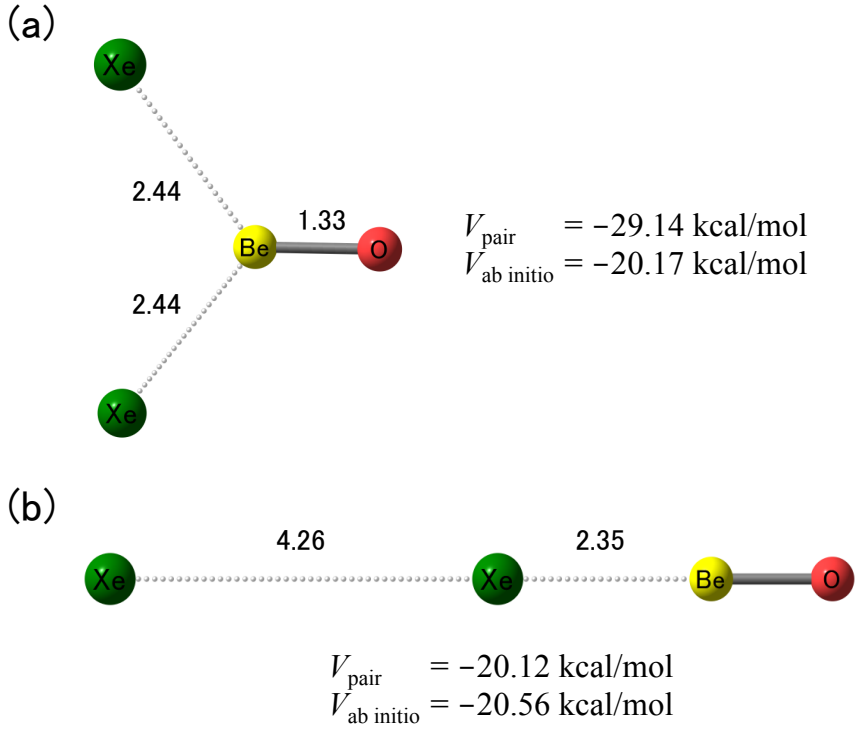

Figure 2. Minimum energy structures of Xe_2BeO obtained by (a) the pairwise-additive model and (b) *ab initio* calculations. Bond lengths are given in unit of Å.

3-2-1. *Ab initio* calculations

All *ab initio* potential energies are calculated by the coupled-cluster singles and doubles including the perturbative contributions of connected triple excitations [CCSD(T)] method. The excitations from Be 1*s* orbital are also included in the calculation. The cc-pCVQZ basis set is used for Be and the aug-cc-pVQZ basis sets are employed for O and Ar atoms. For Xe atoms, Stuttgart RLC ECP is employed.[10] As a preliminary calculation, the Xe-Xe potential energy curve is computed with this method. The equilibrium distance and binding energy are calculated to be r_{min} = 4.561 Å and D_e = 0.430 kcal/mol, respectively. These values are in good agreement with those of the Lennard-Jones parameters[11], r_{min} = 4.602 Å and D_e = 0.442 kcal/mol, which are commonly used in simulations of solid xenon. The BSSE-corrected binding energy that is obtained by the counterpoise method becomes D_e = 0.265 kcal/mol and it is much smaller than that of the Lennard-Jones parameters, therefore the BSSE correction is not applied to the XeBeO-Xe interaction. For Ar-Ar interaction, the potential energy curve with the BSSE correction exhibits r_{min} = 3.827 Å and D_e = 0.238 kcal/mol, which agree well with the reported values of Lennard-Jones parameters r_{min} = 3.822 Å and D_e = 0.238 kcal/mol. Therefore, XeBeO-Ar and ArBeO-Ar interactions are corrected by the counterpoise method. The XeBeO-Xe, XeBeO-Ar, and ArBeO-Ar interaction potential energies are calculated for every normal coordinates of RgBeO (**q**) at predetermined points represented by polar coordinates (r, θ), where r is the distance of Rg from the center-of-mass of RgBeO and θ is the angle measured from the molecular axis of RgBeO. The grid points are in the range of 2 to 8 Å and 0 to 180 degrees with a spacing of 0.2 Å and 4.5 degrees for r and θ, respectively. The interaction potential energies of Xe-Xe and Ar-Ar are also evaluated in the range of 3 to 20 Å and 2 to 19 Å, respectively, with a grid spacing of 0.1 Å. These energies are tabulated for use in the subsequent Monte Carlo (MC) simulations where the potential energy is evaluated by the Lagrange polynomial interpolation. All *ab initio* calculations are carried out by the MOLPRO2008.1 package.[12]

3-2-2. Potential-Optimized DVR

The vibrational energy levels for the target molecule XeBeO and ArBeO are solved in the presence of surrounding Rg atoms by the discrete variable representation (DVR) method[13] using the Hamiltonian composed of the first, third, and fourth terms in the right-hand side of eq. (1). Since I need to solve this equation in each configuration of Rg atoms which is sampled by the MC method, it is important to reduce the computational cost of this task. For this purpose, I employ the potential-optimized DVR (PO-DVR) method to reduce the size of the basis set.[14] The optimized one-dimensional basis set is obtained by the sinc-DVR method[15] using each normal coordinate of RgBeO with other normal coordinates set to zero. After obtaining these one-dimensional basis sets, the vibrational energy levels for the RgBeO complex in the presence of surrounding Rg atoms are solved using the basis set which is composed of direct products of each optimized one-dimensional basis set.

For RgBeO, there are three normal coordinates which correspond to Be-O stretching (q_1), Rg-Be stretching (q_2), and bending motion (q_3). In obtaining the optimized one-dimensional basis set, the sinc-DVR calculation is first performed for each normal coordinate using 200 grid points in the range of [−1.1, 1.1] , [−1.9, 1.9], and [−2.0, 2.0] Å·(amu)$^{1/2}$ for q_1, q_2, and q_3, respectively. After solving the above equations, I employ the first ten eigenfunctions as an optimized one-dimensional basis set for each q_1, q_2, and q_3. This size of the basis set is large enough to obtain a converged value of fundamental frequency of Be-O stretching motion in both XeBeO and ArBeO. In the MC simulations, I use two normal modes that correspond to Be-O (q_1) and Rg-Be (q_2) stretching motions, and in this case five and three optimized one-dimensional basis functions are employed for q_1 and q_2, respectively, to save computational time. This reduced size of the basis set is still large enough to obtain a converged value when only q_1 and q_2 are used (referred to 2D-DVR below).

3-2-3. Monte Carlo simulation

The MC calculations are performed to obtain vibrational spectra of RgBeO complex in the matrix environment at finite temperatures. The sampling is performed according to the distribution $\rho(\mathbf{R}) \propto \exp(-\beta V(\mathbf{R}))$, where the potential energy is represented by

$$V(\mathbf{R}) = E^0_{\text{qm}}(\mathbf{R}) + \sum_{i<j}^{N} V_{\text{Rg-Rg}}(|\mathbf{R}^{(i)} - \mathbf{R}^{(j)}|). \tag{4}$$

In the above equation, $E^0_{\text{qm}}(\mathbf{R})$ is the vibrational ground state energy in the presence of surrounding Rg atoms, which is obtained as the lowest eigenenergy in the PO-DVR equation. In the conventional MC sampling, the PO-DVR equation must be solved in each step, even if a single Rg atom that is far from the molecule is chosen to move, which gives only slight modification of the potential used for solving the PO-DVR equation.

In order to further enhance the efficiency of MC sampling, I employ the multiple Markov chain method, which is also known as the approximate potential method.[16,17] In this work, an auxiliary MC sampling is performed using the approximate potential defined by

$$V_{\text{ap}}(\mathbf{R}) = \sum_{i=1}^{N} V_{\text{qm-Rg}}(\hat{\mathbf{q}} = 0, \mathbf{R}^{(i)}) + \sum_{i<j}^{N} V_{\text{Rg-Rg}}(|\mathbf{R}^{(i)} - \mathbf{R}^{(j)}|) \tag{5}$$

and after a certain number of steps on this approximate potential, the difference between the original and approximate potential is used as a criterion to restore sampling with respect to the original potential. The acceptance probability in this procedure for a trial move $\mathbf{R} \rightarrow \mathbf{R}'$ is therefore given as

$$
\begin{aligned}
P(\mathbf{R}\to\mathbf{R}') &= \min\left[1,\exp\left\{-\beta\left[\left(V(\mathbf{R}')-V_{\mathrm{ap}}(\mathbf{R}')\right)-\left(V(\mathbf{R})-V_{\mathrm{ap}}(\mathbf{R})\right)\right]\right\}\right] \\
&= \min\left[1,\exp\left\{-\beta\left[\left(E^0_{\mathrm{qm}}(\mathbf{R}')-\sum_{i=1}^{N}V_{\text{qm-Rg}}(\hat{\mathbf{q}}=0,\mathbf{R}'^{(i)})\right)-\left(E^0_{\mathrm{qm}}(\mathbf{R})-\sum_{i=1}^{N}V_{\text{qm-Rg}}(\hat{\mathbf{q}}=0,\mathbf{R}^{(i)})\right)\right]\right\}\right]
\end{aligned}
\tag{6}
$$

With this method, correlation in the Markov chain on the original potential is significantly reduced. The sampling on the approximate potential is much less expensive than the original potential, since one does not need to solve the PO-DVR equation. In fact, when the number of sampling on the approximate potential is N_s = 100, I obtained around 95% acceptance probability in the trial move defined in eq. (6).

I do not investigate the systematic comparison regarding the efficiency in this paper, but from my experience significant computational saving has been achieved.

The vibrational spectra are obtained by the following simple form as

$$
I(\omega) = \int d\mathbf{R}\,\delta(E^1_{\mathrm{qm}}(\mathbf{R})-E^0_{\mathrm{qm}}(\mathbf{R})-\omega)\rho(\mathbf{R}) \tag{7}
$$

where $E^1_{\mathrm{qm}}(\mathbf{R})$ is the first vibrational excited-state energy of Be-O stretching motion in RgBeO complex.

3-3. Results and Discussion

3-3-1. *Ab initio* calculations for BeO, XeBeO, and ArBeO

The potential energy surfaces of BeO, XeBeO, and ArBeO were computed by the CCSD(T) method, and the geometry optimization and vibrational frequency calculations were also performed. Table II summarizes equilibrium bond lengths, harmonic and fundamental frequencies of Be-O stretching motion in BeO, XeBeO, and ArBeO. The binding energy of Xe to BeO was calculated to be 19.65 kcal/mol and it is much stronger than that of the Xe-Xe interaction (0.433 kcal/mol) by two orders of magnitude. The binding energy of Ar to BeO is found to be 11.67 kcal/mol, and it is also quite strong compared to the Ar-Ar interaction (0.238 kcal/mol). The vibrational energy levels were calculated using potential-optimized basis sets, and 1D-DVR represents the calculation using a basis set only for q_1 (Be-O stretching). The results denoted by 2D-DVR were obtained using basis sets for both q_1 and q_2 (Xe-Be or Ar-Be stretching), while 3D-DVR indicates that all three basis sets were employed.

The fundamental frequency for BeO molecule was calculated to be 1459 cm^{-1} and is in good agreement with experimental data of 1464 cm^{-1}.[9] Upon formation of the XeBeO complex, the equilibrium bond length of r_e(Be-O) remains almost unchanged. However, spectral shifts of Be-O stretching motion by 75 cm^{-1} for harmonic frequency and 78 cm^{-1} for fundamental frequency in 2D-DVR calculation are observed. This blue shift can be attributed to the increased charge separation that is caused by the strong charge-induced dipole interaction, as was found in Ref.7. As was pointed out previously, the frequency shift of 78 cm^{-1} is larger than that of 34 cm^{-1} measured experimentally in Xe matrix. The fundamental frequency obtained by 3D-DVR was calculated to be 1535 cm^{-1}, and the difference between the 2D-DVR and 3D-DVR methods is only ~2 cm^{-1}, which means that the inclusion of the bending motion affects the fundamental frequency of Be-O stretching motion only marginally. This leads us to neglect the bending motion in the MC simulations, since it is highly expensive to construct the XeBeO-Rg potential energy surface when all vibrational modes of XeBeO are included. The fundamental frequency for ArBeO is blue-shifted by 80 cm^{-1} from BeO in 2D-DVR calculations, and it is slightly larger than that of XeBeO, which is

consistent with the previous work.[7] This shift is relatively close to the experimental value of 62 cm^{-1}, which was measured in Ar matrix (see Table I), and it may be predicted that the effect of surrounding Ar atoms is small. The bond length of Be-O is again almost unchanged upon formation of ArBeO. From the same reason as above, the MC simulations for ArBeO-Ar_N are performed using 2D-DVR for solving the vibrational energy levels of ArBeO.

Table II. Equilibrium bond lengths (in Å), harmonic and fundamental frequencies (in cm^{-1}) of Be-O stretching motion for BeO, XeBeO, and ArBeO.

	r_e(Be-O)	r_e(Rg-Be)	Harmonic	Fundamental		
				1D-DVR	2D-DVR	3D-DVR
BeO	1.333	—	1483	1459	—	—
XeBeO	1.333	2.350	1558	1543	1537	1535
ArBeO	1.331	2.068	1560	1545	1539	1536
BeO (exp.)[a]	1.331	—	1487[a]	1464[b]		

[a] Reference[9], [b]Fundamental frequency

3-3-1. Potential energy surfaces for XeBeO-Xe, XeBeO-Ar, and ArBeO-Ar

Figure 3 shows the two-dimensional contour plots of the potential energy surfaces for XeBeO-Xe, XeBeO-Ar, and ArBeO-Ar, where the internal coordinates of XeBeO and ArBeO are fixed at the equilibrium values. As can be seen in the figure, three local minima were located for each potential, where two of them are on both side of the molecule in collinear geometry. The binding energies of Xe to XeBeO for these collinear configurations are 0.906 and 1.893 kcal/mol on the Xe (Structure-I) and O sides (Structure-II), respectively. Another minimum is located between and almost equidistant from Be and O atoms with a binding energy of 1.653 kcal/mol (Structure-III). The binding energies of Ar to XeBeO and ArBeO for these three minima are tabulated in Table III. These values at three local minima for XeBeO-Xe (XeBeO-Ar or ArBeO-Ar) are almost in the same order as in the Xe-Xe (Ar-Ar) interaction.

Table III. Binding energies (in kcal/mol) of Xe or Ar to RgBeO.

	XeBeO-Xe	XeBeO-Ar	ArBeO-Ar
Structure-I	0.906	0.481	0.449
Structure-II	1.893	0.761	0.715
Structure-III	1.653	0.752	0.787

The validity of the pairwise-additive description of the potential energy for RgBeO-Rg_N system, as is given in eq. (1), should of course be examined. For this purpose the interaction energy of XeBeO-Xe_6 cluster is compared between the *ab initio* method and pairwise-additive model. I randomly choose several configurations from the MC simulations of XeBeO-Xe_{500} cluster (which will be detailed later) and the nearest six Xe atoms to XeBeO are taken to form XeBeO-Xe_6 clusters. As a result of comparison, differences between the interaction energies by the *ab initio* method and

the pairwise-additive model were calculated to be ~0.1 kcal/mol for all cases, which shows a good agreement with each other. More importantly, the fundamental frequencies were compared between these two potentials and the differences were only ~0.2 cm^{-1} for 2D-DVR calculations, which gives confidence in the reliability of the pairwise-additive model for RgBeO-Rg_N systems.

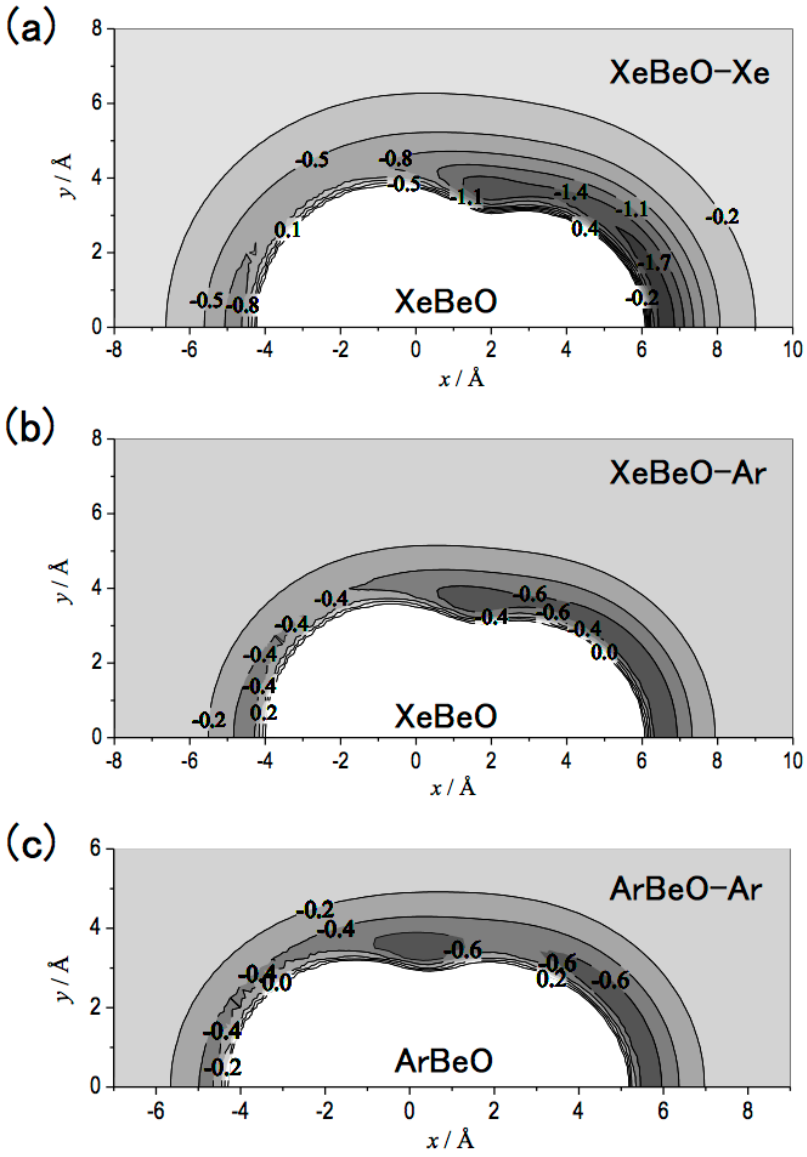

Figure 3. Two-dimensional contour plots of the potential energy surfaces (in units of kcal/mol) for (a) XeBeO-Xe, (b) XeBeO-Ar, and (c) ArBeO-Ar. The internal coordinates of RgBeO (Rg = Xe or Ar) are fixed at the equilibrium values and the origin is set to the center-of-mass of RgBeO. The positions of the Xe, Be, and O are (−0.51, 0.0), (1.84, 0.0), and (3.17, 0.0), respectively, for XeBeO, and those of the Ar, Be, and O atoms are (−1.12, 0.0), (0.94, 0.0), and (2.27, 0.0), respectively, for ArBeO.

3-3-2. Monte Carlo simulations for XeBeO-Xe$_N$, XeBeO-Ar$_N$, and ArBeO-Ar$_N$

The MC simulations were performed for XeBeO in solid Xe and Ar and for ArBeO in solid Ar under the periodic boundary condition (PBC) at temperature of T = 30 K. The fcc lattice was taken as a staring point for the initial configuration and 500 Xe (500 Ar) atoms were placed in a cubic box with a cell length of 30.6 Å (26.6 Å), which yields a density of 3.78 g/cm^3 (1.76 g/cm^3) and is close to the experimental value at the saturated vapor condition.[18] There are several possible sites at which Rg atom(s) can be substituted by RgBeO. As shown in Figure 4, one or two Rg atoms along the three possible orientations were replaced with a single RgBeO and these configurations were used to initiate MC simulations. The number of substituted Rg atoms was determined from a sensible choice based on the distance between the adjacent atoms along each orientation and it is shown in Table IV. After equilibrating the system, a total of 10^6 MC steps were taken to obtain statistical averages. Here, in each MC step, 100 steps were used on the approximate potential that is given in eq. (6).

The MC results are summarized in Table V, where the peak positions of Be-O vibrational spectra of RgBeO are given, along with the full width at half maximum (FWHM) values of the vibrational spectra. I also evaluate the interaction energies between RgBeO and other surrounding Rg atoms in order to compare the stability of each site. The interaction energy is simply defined as

$$\langle V_{\text{int}} \rangle = \langle E^0_{\text{qm}}(\mathbf{R}) \rangle - E^0 \tag{7}$$

where $E^0_{\text{qm}}(\mathbf{R})$ is the vibrational ground state energy of RgBeO that includes the interaction with surrounding Rg atoms, which is given in eq. (4), and E^0 is that in the gas phase. The Rg atoms whose distances from the center-of-mass of RgBeO are within the half of the length of the unit cell are taken into account to calculate the above interaction energies. In an ideal simulation, one could discuss the stability of each site

by exploring all possible configurations in a long MC run, but at this low temperature, once RgBeO is inserted in one site, it is practically impossible to observe the migration between the sites within a routinely used number of MC steps. By using more sophisticated approaches such as the multicanonical algorithms, it may be possible to compare the stability of each site directly, but in this paper I simply use the interaction energy as a measure of the stability.

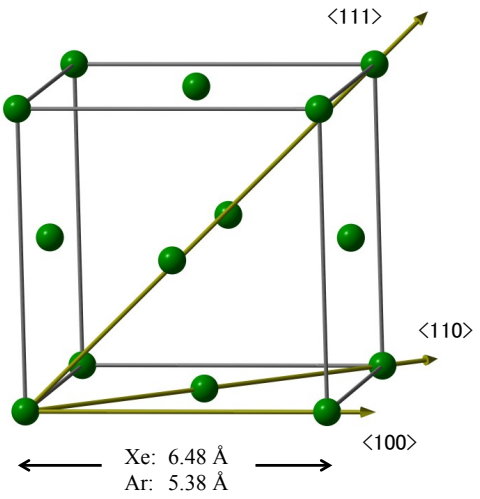

Figure 4. Fcc lattice structure of solid Xe or Ar. The three possible orientations of RgBeO are depicted as <100> (four-atomic window), <110> (nearest neighbor), and <111> (three-atomic window).

Table IV. Peak positions of vibrational spectra (in cm^{-1}) of Be-O stretching motion of RgBeO and interaction energy (in kcal/mol) in solid Xe and Ar under PBC. The FWHM values (in cm^{-1}) of the vibrational spectra are also shown. N_r is the number of rare gas atom(s) replaced with a single RgBeO. The shifts from the gas phase values (1537 cm^{-1} for XeBeO and 1539 cm^{-1} for ArBeO) are shown in the last column.

	N_r	freq.	FWHM	V_{int}	shift
XeBeO in solid Xe					
<100>	1	1543	8	−18.7	+6
<110>	2	1516	3	−20.0	−21
<111>	1	1513	7	−19.2	−24
XeBeO in solid Ar					
<100>	1	1544	7	−11.0	+7
<110>	2	1529	3	−13.1	−8
<111>	1	1538	7	−11.2	+1
ArBeO in solid Ar					
<100>	1	1560	7	−9.6	+21
<110>	2	1531	3	−12.4	−8
<111>	1	(1531)	(3)	(−12.4)	(−8)

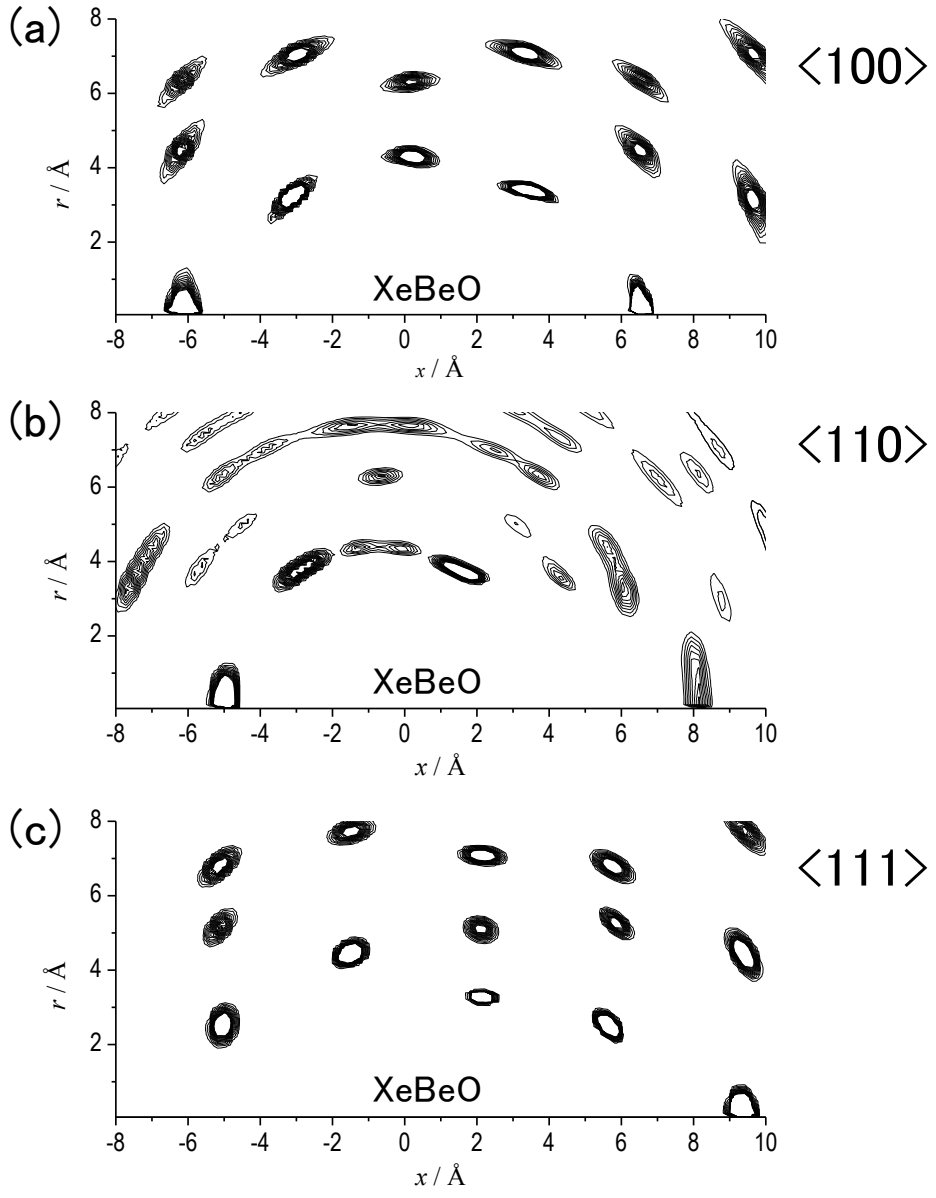

Figure 5. Contour plots of two-dimensional distribution functions of the Xe atoms around XeBeO for the (a) <100>, (b) <110>, and (c) <111> sites. The positions of XeBeO are the same as those in Figure 3.

In order to investigate in more detail how the Rg atoms are distributed around RgBeO during the crystallization, I performed MC simulations for XeBeO-Xe_N, XeBeO-Ar_N, and ArBeO-Ar_N clusters with N = 500. A total of ten independent simulations were performed at T = 30 K. Prior to each simulation, the system was heated up to 150 K under the confinement potential and after a sufficient number of steps at 150 K where the cluster exhibited liquid-like behavior, it was cooled down to 30 K gradually with a decrement of 10 K. The confinement potential has a functional form of $V = (r/R_{conf})^{20}$, where r is the distance of Rg from the center-of-mass of the cluster and R_{conf} is a parameter to determine the size of the confinement potential. Note that this confinement potential is added to prevent the evaporation of Rg atoms at 150 K and is removed at 30 K. At this low temperature of 30 K, once the atomic configurations are determined, the atoms do not change their positions frequently because the clusters are in the solid phase. As expected, the clusters exhibit a somewhat amorphous-like structure, and the configurations of the Rg atoms around RgBeO were different in each simulation due to the technical difficulty of crystallization in MC simulations, also because the existence of the impurity made it more difficult to form the crystal structure around it. Since there are a huge number of stable structures even for clusters with small number of Rg atoms, each MC run is trapped in one of these configurations. Thus, the peak positions of vibrational spectra from different MC runs scattered to some extent, but it was observed that they were within a relatively narrow range, except for two MC runs in the XeBeO-Xe_N clusters.

In Table V the average values of peak positions of vibrational spectra and their standard deviations from ten MC runs are shown. As seen in the table, the standard deviations are small for all three types of clusters. In the simulations of XeBeO-Xe_N clusters, the above-mentioned two MC runs are excluded when calculating the averages. These two runs have peak frequencies of 1544 and 1542 cm^{-1} and interaction energies of -19.0 and -18.9 kcal/mol, and these values are close to the ones at the <100> site. When inspecting the two-dimensional distribution functions for these two runs, it was found that the Xe atom was located around x = 6.5 Å in the collinear geometry, which is typical of the <100> site. For the other eight runs, the vibrational frequencies and interaction energies are close to the ones at the <110> and <111> sites. When I examine the configurations of the Xe atoms around XeBeO, however, it was difficult to

distinguish which sites were formed inside the cluster since in some cases the Xe atoms were not found in collinear geometry of XeBeO as was observed in the simulations of solid Xe. Judging by the distribution functions, some runs could be assigned to the <110> site, but in some other runs, they were found to be more like the <111> site. On the other hand, in the simulations of XeBeO-Ar_N and ArBeO-Ar_N clusters, the average values of frequency and interaction energy are in good agreement with those at the <110> site and the distribution functions of each simulation bear a close resemblance to those of the <110> site. It is safe to say that the <110> site is most likely formed for these clusters. In all three types of clusters, at least it was confirmed that the red shifts were observed, and the interaction energies are close to those at the <110> site. From the above simulations on clusters and also those under PBC, it would be naturally expected that the <110> site would represent a plausible configuration inside the matrices.

Table V. The average values of peak positions of vibrational spectra (in cm^{-1}) and interaction energies (in kcal/mol) from ten independent MC simulations. The standard deviations are shown in parenthesis.

	freq	V_{int}
XeBeO-Xe_N	1513 (1.9)	−20.6 (0.31)
XeBeO-Ar_N	1530 (1.6)	−13.2 (0.15)
ArBeO-Ar_N	1532 (1.3)	−12.5 (0.23)

In summary, the vibrational shift from the isolated BeO was calculated to be 57, 70, and 72 cm^{-1} for XeBeO in solid Xe, XeBeO in solid Ar, and ArBeO in solid Ar, respectively, at the <110> site, and 54, 71, and 73 cm^{-1} from the calculations of clusters (see Table VI). These values are in reasonable agreement with experimental data of 34, 53, and 62 cm^{-1}. I note, however, that these shifts depend strongly on the quality of the potential and it would improve the agreement by performing more accurate *ab initio* calculations. Of course, there is also room for improvement in the methodology. As shown in the gas phase calculation of RgBeO, the inclusion of Rg-Be-O bending motion slightly lower the vibrational frequency, therefore if I perform 3D-DVR MC simulation,

it would predict more closer value to the experimental one. However, given the quality of the interaction potential employed in this study, I believe that it successfully reproduces the experimental observations.

Table VI. Summary of the present work and experimental data on vibrational frequency (in cm^{-1}). The frequencies shown as solid Xe and Ar are taken from the <110> site. The vibrational shifts from the gas phase values of BeO are included in parenthesis.

	BeO	XeBeO	XeBeO in solid Xe	XeBeO in Xe cluster
this work	1459	1537 (+78)	1516 (+57)	1513 (+54)
exp.	1464	—	1498 (+34)	
			XeBeO in solid Ar	XeBeO in Ar cluster
this work			1529 (+70)	1530 (+71)
exp.			1517 (+53)	
		ArBeO	ArBeO in solid Ar	ArBeO in Ar cluster
this work		1539 (+80)	1531 (+72)	1532 (+73)
exp.		—	1526 (+62)	

3-4. Conclusion

In this study I performed mixed quantum-classical simulations for vibrational spectra of BeO in the Xe and Ar matrix environments and investigated the origin of spectral shift in detail. The high-level *ab initio* calculations were carried out to determine the interaction potential needed to construct the total potential of the system, and the MC simulations were performed using this potential in order to obtain vibrational spectra in the presence of surrounding rare gas atoms.

It was found that the BeO molecule forms stable XeBeO or ArBeO complex inside the rare gas matrices, which alone induces the blue shift in the vibrational spectra of 78 cm^{-1} and 80 cm^{-1}. When the effect of other surrounding rare gas atoms is included, the vibrational frequency is red-shifted from that of XeBeO complex by 21 cm^{-1} in solid Xe and 8 cm^{-1} for ArBeO in solid Ar. The calculated shifts were in reasonable agreement with experimental results.

In conclusion, it is already known that the spectral shift due to the formation of RgBeO complex is not negligible, but the vibrational shift originating from the other surrounding rare gas atoms should be carefully taken into account for quantitative description of the spectral shifts, and therefore the observed shifts are the outcome of the competing effects of rare gas atoms in matrix environments. I are now investigating these effects on other molecules and examine whether this finding also applies to other systems. Also, I are interested in vibrational spectroscopy of exotic molecule HXeCl or HXeBr[19-21], where pronounced complexation effects are observed due to the relatively weak bonding and large dipole moments.[22] The peculiar matrix shift of H-Xe stretching motion in HXeCl, which was observed in neon[19], kryption[20], and xenon[20] matrices, is still not well understood, and I are currently working to scrutinize the origin of the matrix shift in these systems.

3-5. References

1. M. F. Zhou, L. Andrews, and C. W. Bauschlicher, Chem. Rev. **101**, 1931 (2001).
2. C. J. Evans and M. C. L. Gerry, J. Chem. Phys. **112**, 9363 (2000).
3. Y. Y. Zhao, Y. Gong, and M. F. Zhou, J. Phys. Chem. A **110**, 10777 (2006).
4. Y. Taketsugu, T. Noro, and T. Taketsugu, J. Phys. Chem. A **112**, 1018 (2008).
5. G. Frenking, W. Koch, J. Gauss, and D. Cremer, J. Am. Chem. Soc. **110**, 8007 (1988).
6. C. A. Thompson and L. Andrews, J. Am. Chem. Soc. **116**, 423 (1994).
7. A. Veldkamp and G. Frenking, Chem. Phys. Lett. **226**, 11 (1994).
8. C. A. Thompson and L. Andrews, J. Chem. Phys. **100**, 8689 (1994).
9. K. P. Huber and G. Herzberg, *Constants of diatomic molecules*. (Van Nostrand Reinhold, New York, 1979).
10. G. Igelmann, H. Stoll, and H. Preuss, Mol. Phys. **65**, 1321 (1988).
11. R. P. White, S. M. Cleary, and H. R. Mayne, J. Chem. Phys. **123**, 10 (2005).
12. MOLPRO, version 2008.1, a package of *ab initio* programs, H.-J. Werner, P. J. Knowles, R. Lindh, F. R. Manby, M. Schütz, and others.
13. J. C. Light, I. P. Hamilton, and J. V. Lill, J. Chem. Phys. **82**, 1400 (1985).
14. J. Echave and D. C. Clary, Chem. Phys. Lett. **190**, 225 (1992).
15. D. T. Colbert and W. H. Miller, J. Chem. Phys. **96**, 1982 (1992).
16. L. D. Gelb, J. Chem. Phys. **118**, 7747 (2003).
17. A. Nakayama, N. Seki, and T. Taketsugu, J. Chem. Phys. **130**, 024107 (2009).
18. G. L. Pollack, Rev. Mod. Phys. **36**, 748 (1964).
19. M. Lorenz, M. Räsänen, and V. E. Bondybey, J. Phys. Chem. A **104**, 3770 (2000).
20. M. Pettersson, J. Lundell, and M. Räsänen, J. Chem. Phys. **102**, 6423 (1995).
21. Z. Bihary, G. M. Chaban, and R. B. Gerber, J. Chem. Phys. **116**, 5521 (2002).
22. L. Khriachtchev, M. Räsänen, and R. B. Gerber, Acc. Chem. Res. **42**, 183 (2009).

4. Vibrational Shifts of HXeCl in Matrix Environments

4-1. Introduction

The noble-gas elements were considered to be chemically inactive for a long time. Since an inspiring suggestion by Pauling[1] and a pioneering work by Bartlett[2] on the discovery of the first noble-gas compound, $Xe^{+}[PtF_6]^{-}$, the noble-gas chemistry has emerged as one of disciplines in chemical sciences. To date, a large number of chemically interesting and unique noble-gas compounds and/or complexes have been experimentally prepared[3-5] (see refs. [6-8] for such examples), and theoretical calculations have served to interpret the origin of the peculiar chemical bonds in these compounds and also to predict new types of noble-gas compounds.

In recent years, there is a revival of interest in noble-gas chemistry mainly due to the discovery of noble-gas hydrides.[9-11] These compounds have a structural form of HNgY, where Ng is a noble-gas atom and Y is an electronegative fragment, and these compounds are formed upon the UV photolysis of the HY precursors in the noble-gas matrix, followed by thermal mobilization of the H atom.[12-14] The unique electronic character of these compounds has been the focus of intensive research, and with the help of high-level *ab initio* quantum chemical calculations it has been demonstrated that these noble-gas hydrides have a strong ion-pair character of the form $(HNg)^{+}Y^{-}$ and that these hydrides exhibit large dipole moments.[15-17] For recent reviews, the reader is referred to previous reports, *e.g.* Ref.[11]. Since these unique electronic characters induce the unusual solvation effects in matrix environments, there have been many attempts to elucidate the solvation mechanisms (*e.g.* HArF in noble-gas matrix[18-19]). One of the interesting observations is that the H-Xe stretching frequency of HXeCl exhibits unusual spectral shifts in noble-gas matrices.[9, 20-21] Because the HXeCl

compound possesses a large dipole moment, it is natural to suppose that vibrational frequency decreases in more polarizable environments. However, the H-Xe stretching vibration exhibits higher frequency in the Kr (1664 cm^{-1})[9] and Xe (1649 cm^{-1})[9, 20] matrices compared to that in the Ne matrix (1612 cm^{-1})[21] and the amount of shifts does not correlate with the polarizability of surrounding noble-gas atoms.

In the preceding paper,[22] I have investigated the vibrational shifts of BeO in Xe and Ar matrices by hybrid quantum-classical simulations and found that a stable XeBeO (or ArBeO) complex is formed inside the noble-gas matrices. The complexation of XeBeO (or ArBeO) alone induces a blue shift in the vibrational spectra of a Be-O stretching motion, but the surrounding noble-gas atoms have a nonnegligible effect on the vibrational frequency, which results in the lowering of the frequency by 21 cm^{-1} for XeBeO in the Xe matrix and 8 cm^{-1} for ArBeO in the Ar matrix. These results imply that the explicit treatment of the surrounding noble-gas atoms is essential to accurately describe the matrix shifts.

In this paper I perform the hybrid quantum-classical simulations of HXeCl in matrix environments in order to investigate the origin of unusual spectral shifts in noble-gas matrices (Ng = Ne, Ar, Kr, Xe) described above. The high-level *ab initio* calculations employing the coupled-cluster singles and doubles including the perturbative contributions of connected triple excitations [CCSD(T)] method are performed to construct the interaction potential energy surfaces between HXeCl and noble-gas atoms, and the configurations of noble-gas atoms around HXeCl are sampled by the Monte Carlo calculations, where the vibrational levels of HXeCl are solved by the discrete variable representation (DVR) approach.

This paper is organized as follows. After presenting the computational details, the results of *ab initio* calculations of HXeCl and vibrational analysis are presented, followed by the features of potential energy surfaces and the vibrational shifts of HXeCl−Ng complexes. Then, the results of MC simulations are given for HXeCl in solid noble-gas matrices under the periodic boundary conditions (PBC) and also in large clusters. Finally, some concluding remarks are offered.

4-2. Computational Details

The hybrid quantum-classical simulations are performed to obtain the vibrational spectra of HXeCl in matrix environments. The computational details are provided in my previous paper.[22] In brief, the total system is divided into quantum and classical parts, where the quantum part consists of HXeCl represented by N_q normal coordinates while the classical part is composed of N surrounding noble-gas (Ng) atoms. The hybrid quantum-classical Hamiltonian of the whole system is then assumed to have the following pairwise-additive form,

$$H = \sum_{i=1}^{N_q} \frac{1}{2} \hat{p}_i^2 + \sum_{i=1}^{N} \frac{1}{2} \mathbf{P}^{(i)} + V_{\text{HXeCl}}(\hat{\mathbf{q}}) + \sum_{i=1}^{N} V_{\text{HXeCl-Ng}}(\hat{\mathbf{q}}, \mathbf{R}^{(i)}) + \sum_{i<j}^{N} V_{\text{Ng-Ng}}(|\mathbf{R}^{(i)} - \mathbf{R}^{(j)}|) \quad (1)$$

where $\hat{\mathbf{q}} = \{\hat{q}_i; i = 1,\text{K}, N_q\}$ and $\hat{\mathbf{p}} = \{\hat{p}_i; i = 1,\text{K}, N_q\}$ represent the normal coordinates and their conjugate momenta of HXeCl, respectively. $\mathbf{R} = \{\mathbf{R}^{(i)}; i = 1,\text{K}, N\}$ and $\mathbf{P} = \{\mathbf{P}^{(i)}; i = 1,\text{K}, N\}$ are the coordinates and momenta of noble-gas atoms (Ng = Ne, Ar, Kr, Xe), respectively. Here the center-of-mass and rotational motions of HXeCl are treated classically and they are not included in the above Hamiltonian. $V_{\text{HXeCl–Ng}}$ is the interaction potential energy between HXeCl and an Ng atom and it is obtained from *ab initio* calculations employing the CCSD(T) method, details of which are provided below. $V_{\text{Ng–Ng}}$ is the interaction potential energy of Ng dimers and this term is also determined by *ab initio* calculations.

4-2-1. *Ab initio* calculations

All *ab initio* potential energies are calculated by the CCSD(T) method. The cc-pVQZ basis sets are used for H and Cl atoms, while the aug-cc-pVQZ basis sets are employed for noble-gas atoms (Ne, Ar, Kr, and Xe). For Kr and Xe, the relativistic pseudopotentials[23] are used. The CCSD(T) method in conjunction with these basis sets is known to yield reliable potential energy curves for Ng dimers, and equilibrium distances and binding energies at this computational level are tabulated in Table I, along with the reported accurate values. The addition of diffuse functions on Cl atom seems to be important since the Cl atom exhibits a large negative charge in the compound, but the effects of diffuse functions are found to be small for structural parameters and binding energies of HXeCl−Ng complexes (see the results section below), and therefore I omit them since it is very computationally demanding to construct the potential energy surfaces with this extensive basis set.

Table I. Equilibrium bond distance r_e (in Å) and binding energy D_e (in kcal/mol) of noble-gas dimer.

	Ne−Ne		Ar−Ar		Kr−Kr		Xe−Xe	
	This work	ref. [24-25]	This work	ref. [25-26]	This work	ref. [25, 27]	This work	ref. [28-29]
r_e	3.093	3.091	3.801	3.757	4.058	4.008	4.453	4.363
D_e	0.095	0.084	0.274	0.285	0.374	0.400	0.489	0.561

The interaction potential energies between HXeCl and an Ng atom are obtained for each normal coordinate of HXeCl (**q**) at predetermined positions of the Ng atom represented by polar coordinates (r, θ, φ), where r is the distance of Ng from the center-of-mass of HXeCl and θ is the polar angle measured from the molecular axis of HXeCl. φ is the azimuthal angle measured from the plane of the bending vibration of HXeCl. The numbers of grid points are 21, 21, and 4 for r, θ, and φ, respectively. The interaction potential energies of noble-gas dimers (*e.g.* Ne−Ne) are also evaluated

using the grid points of 100. These energies are tabulated for use in the subsequent MC simulations and the potential energies are evaluated by the spline interpolation in the MC runs. All *ab initio* calculations are carried out by the MOLPRO2010.1 package.[30-31]

4-2-2. Potential-Optimized DVR and Monte Carlo simulation

The vibrational energy levels of HXeCl are solved in the presence of surrounding Ng atoms by the potential-optimized discrete variable representation (PO-DVR) method[32] and the details are provided in the preceding paper.[22] The normal coordinates of HXeCl are used to represent the optimized basis set, and DVR-1D indicates that the normal coordinate of only the H-Xe stretching vibration ($q_{\text{H-Xe}}$) is employed to solve the DVR equation with the other normal coordinates fixed to zero, while DVR-3D represents that $q_{\text{H-Xe}}$ plus the doubly degenerate bending vibrations ($q^{+}_{\text{H-Xe-Cl}}$ and $q^{-}_{\text{H-Xe-Cl}}$) are included in the DVR equation. The Xe-Cl stretching vibration is not taken into account since the inclusion of this vibration induces the marginal effect on the H-Xe vibrational frequency. In fact, the DVR calculation that employs both the H-Xe and Xe-Cl stretching vibrations lowers the frequency by ~1 cm^{-1}, compared to that of the DVR-1D calculation. The number of optimized basis sets employed are 8, 6, and 6 for $q_{\text{H-Xe}}$, $q^{+}_{\text{H-Xe-Cl}}$, and $q^{-}_{\text{H-Xe-Cl}}$, respectively, and it is confirmed that the H-Xe stretching frequency converges well with respect to the number of optimized basis set.

The MC calculations are performed to sample the configurations of Ng atoms around HXeCl. The sampling is performed according to the distribution $\rho(\mathbf{R}) \propto \exp(-\beta V(\mathbf{R}))$, where $V(\mathbf{R})$ is represented by

$$V(\mathbf{R}) = E^{0}_{\text{qm}}(\mathbf{R}) + \sum_{i<j}^{N} V_{\text{Ng-Ng}}(|\,\mathbf{R}^{(i)} - \mathbf{R}^{(j)}\,|)\,. \tag{2}$$

Here $E^{0}_{\text{qm}}(\mathbf{R})$ is the vibrational ground-state energy of HXeCl obtained by the PO-DVR method, where the first, third, and fourth terms in eq. (1) are used. In the standard MC simulations, this PO-DVR equation must be solved in each step since it includes the interaction between HXeCl and surrounding Ng atoms. It is apparently inefficient especially when a single Ng atom that is far from the molecule is chosen to move, since it yields only the slight modification of the potential energy used for solving the PO-DVR equation. In the preceding paper,[22] I introduced an efficient

scheme to reduce the computational cost in the framework of the approximate potential method[33-34] and this scheme is also employed in the present work. In obtaining the vibrational spectra, the following simple form is employed

$$I(\omega) = \int d\mathbf{R}\delta(E^{1}_{\mathrm{qm}}(\mathbf{R}) - E^{0}_{\mathrm{qm}}(\mathbf{R}) - \omega)\rho(\mathbf{R}), \quad (3)$$

where $E^{1}_{\mathrm{qm}}(\mathbf{R})$ is the energy of the first excited state of H-Xe stretching vibration.

4-3. Results and Discussion

4-3-1. Equilibrium structure and vibrational analysis of HXeCl

The geometry optimization was performed for HXeCl by the CCSD(T) method and it was followed by the vibrational frequency analysis. The equilibrium bond lengths and fundamental frequencies of H-Xe stretching vibration determined by the DVR-1D and DVR-3D methods are given in Table II (see also Figure 1(a) for equilibrium structure). The harmonic frequency is also included in the table, along with those of other vibrational modes. As seen, the inclusion of anharmonicity along the H-Xe normal coordinate (DVR-1D) induces a large red-shift of 117 cm^{-1}. The inclusion of the bending vibrations by the DVR-3D method also causes a further red-shift of 23 cm^{-1}. As described above, the inclusion of the Xe-Cl stretching vibration only slightly lower the frequency by ~1 cm^{-1}. Bihary *et al.*[35] reported a frequency of 1642 cm^{-1} for an isolated HXeCl molecule using cc-VSCF calculations at the MP2 level, which is in good agreement with my result. The natural charges are also calculated and they are found to be (Q_H, Q_{Xe}, Q_{Cl}) = (−0.019, +0.754, −0.735). It is clearly seen that the molecule exhibits a strong ion-pair character of the form $(HXe)^+Cl^-$.

Table II. Equilibrium bond lengths (r_e in Å) and harmonic and fundamental frequencies (in cm^{-1}) of H-Xe stretching vibration for HXeCl. Harmonic frequencies (in cm^{-1}) of Xe-Cl stretching and bending vibrations are also shown.

r_e(H-Xe)	r_e(Xe-Cl)	Harmonic (H-Xe stretching)	Fundamental (DVR-1D) (H-Xe stretching)	Fundamental (DVR-3D) (H-Xe stretching)	Harmonic (Xe-Cl stretching)	Harmonic (bending)
1.703	2.615	1759	1642	1619	274	561

4-3-2. Potential energy surfaces and vibrational frequencies of HXeCl−Ng

Figure 2 shows the two-dimensional contour plot of the potential energy surface of HXeCl−Xe, where the internal coordinates of HXeCl are fixed to its equilibrium structure. It is noted that the intramolecular structure of HXeCl is negligibly perturbed upon formation of HXeCl−Ng complex and in fact the changes of bond lengths of HXeCl between monomer and complexes in fully relaxed configurations are less than 0.004 Å. Three minima are located (see Figure 1(b-d) for structures), two of which are on both side of the molecule in collinear geometry (referred to as the H-side and Cl-side structures hereafter). The strongest binding site is located between and almost equidistant from Xe and Cl atoms with a binding energy of 1.265 kcal/mol (referred to as the bent structure hereafter). The binding energies of the H-side and Cl-side structures are 0.823 and 0.865 kcal/mol, respectively. It is observed that the potential energy surface around these two minima in the collinear geometry is very shallow with respect to the displacement of Xe in the direction perpendicular to the molecular axis (it is noted that the vibrational frequency analysis at these minima indeed reveals only real frequencies). Here the effects of diffuse functions on the Cl atom are examined at these minima, and it is found that the changes of structural parameters upon inclusion of diffuse functions are less than 0.005 Å and the maximum difference in binding energy is only 0.034 kcal/mol (less than 5% in the binding energy, see Table III, which justifies the neglect of diffuse functions on the Cl atom.

For other HXeCl−Ng (Ng = Ne, Ar, Kr) interactions, three minima are also located in the similar geometrical configurations to HXeCl−Xe. The binding energies of the other Ng atoms to HXeCl at these three minima and structural parameters are summarized in Table III and Table IV, respectively. As seen, the bent structure is the strongest binding site for all cases, and in collinear geometry the Ng atom binds slightly stronger to the Cl side than to the H side. These binding energies of each Ng atom are several times stronger than the dimer interactions of the respective Ng atoms (see Table I).

Table III. Binding energies (in kcal/mol) of Ng (= Ne, Ar, Kr, Xe) atoms to HXeCl.

	H-side	Cl-side	Bent
HXeCl−Ne	0.149	0.181	0.327
HXeCl−Ar	0.447	0.496	0.828
HXeCl−Kr	0.618	0.687	1.052
HXeCl−Xe	0.823	0.865	1.265
HXeCl−Xe[a]	0.827	0.899	1.275

[a]with diffuse functions on the Cl atom (aug-cc-pVQZ)

Table IV. Structural parameters (r in Å and θ in degrees) of the minimum energy configurations for HXeCl−Ng (Ng = Ne, Ar, Kr, Xe).

	r(Ng−H) (H-side)	r(Cl−Ng) (Cl-side)	r(Xe−Ng) (Bent)	θ(Ng−Xe−Cl) (Bent)
HXeCl−Ne	2.970	3.609	3.715	70.9
HXeCl−Ar	3.045	3.742	3.952	69.9
HXeCl−Kr	3.091	3.815	4.066	69.0
HXeCl−Xe	3.192	3.952	4.295	68.0

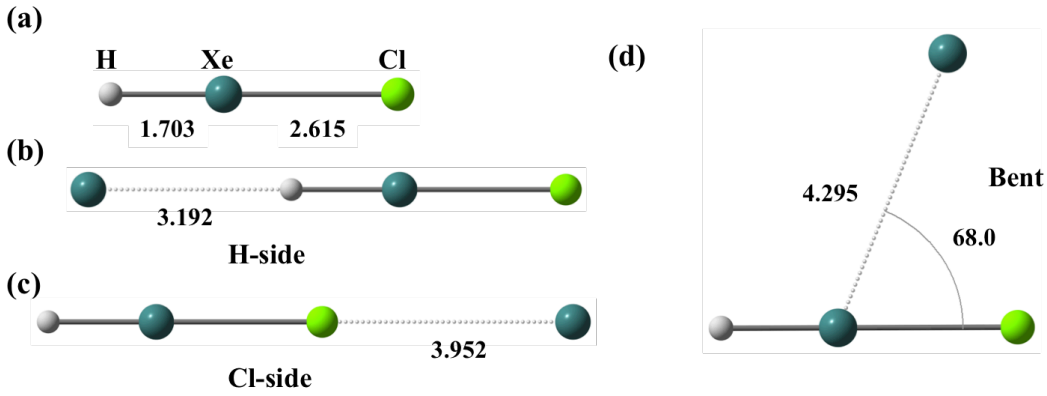

Figure 1. (a) Equilibrium structures of HXeCl. (b-d) Minimum energy configurations of HXeCl−Xe, where the internal coordinates of HXeCl are fixed at the equilibrium values. Lengths are given in units of Å and an angle is given in units of degrees.

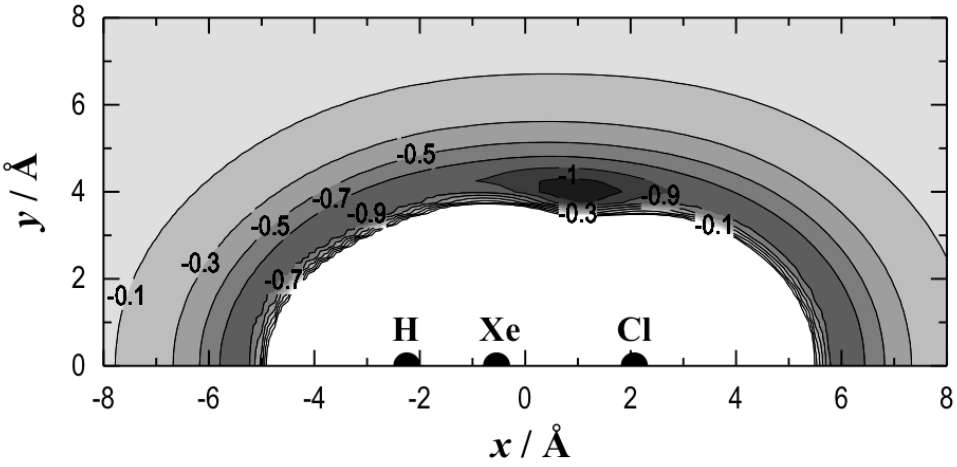

Figure 2. Two-dimensional contour plot of the potential energy surface (in units of kcal/mol) for HXeCl−Xe. The internal coordinates of HXeCl are fixed at the equilibrium values and the origin is set to the center-of-mass of HXeCl. The positions of the H, Xe, and Cl atoms are (−2.245, 0.0), (−0.542, 0.0), and (2.072, 0.0), respectively, and they are shown in filled circles.

At these minima, frequency analysis is made by the DVR-1D and DVR-3D methods, and the results are tabulated in Table V. As expected, the frequencies of H-Xe stretching vibration are most strongly affected at the H-side structures for all HXeCl−Ng complexes. The blue shifts observed in the H-side configuration are due to the repulsive interaction between the Ng and H atoms at the long distance of H-Xe bond length. As seen, the amount of the blue shift in the H-side configuration is increasing as the Ng atom becomes larger (except for a decrease of 1 cm^{-1} in HXeCl−Xe by DVR-3D). These blue shifts are partly in accord with the experimentally observed shifts in matrix environments (Ne: 1612 cm^{-1}, Kr: 1664 cm^{-1}, Xe: 1649 cm^{-1}), but the blue shifts of HXeCl−Kr and HXeCl−Xe are very similar in the calculations (differences of ~1 cm^{-1}), which reveals a discrepancy with the experimental observations. In the following subsection, the MC calculations are performed in order to provide a more realistic modeling of the matrix environments and the vibrational shifts are discussed more quantitatively.

Table V. Fundamental (DVR-1D and DVR-3D) and harmonic frequency (in cm^{-1}) of H-Xe stretching vibration in HXeCl−Ng at the minimum energy structures. The fundamental and harmonic frequencies for isolated HXeCl are 1642 (DVR-1D), 1619 (DVR-3D), and 1759 cm^{-1}, respectively, and the frequency shifts from an isolated HXeCl are also shown.

	H-side		Cl-side		Bent	
	Freq.	Shift	Freq.	Shift	Freq.	Shift
	Fundamental (DVR-1D)					
HXeCl−Ne	1655	+13	1642	+0	1643	+1
HXeCl−Ar	1674	+32	1644	+2	1645	+3
HXeCl−Kr	1677	+35	1644	+2	1647	+5
HXeCl−Xe	1678	+36	1645	+3	1648	+6
	Fundamental (DVR-3D)					
HXeCl−Ne	1631	+12	1619	+0	1620	+1
HXeCl−Ar	1648	+29	1621	+2	1622	+3
HXeCl−Kr	1652	+33	1621	+2	1624	+5
HXeCl−Xe	1651	+32	1621	+2	1625	+6
	Harmonic					
HXeCl−Ne	1765	+6	1759	+0	1759	+0
HXeCl−Ar	1777	+18	1761	+2	1761	+2
HXeCl−Kr	1780	+21	1760	+1	1762	+3
HXeCl−Xe	1780	+21	1759	+0	1768	+9

4-3-3. Monte Carlo simulations for HXeCl−NgN

The MC simulations were performed for HXeCl in solid noble-gas matrices under the periodic boundary condition (PBC) and also for HXeCl−Ng_N clusters in vacuum. In the PBC calculations, the fcc lattice was taken as a starting configuration and 500 Ng atoms are placed in a cubic box. The simulation parameters are tabulated in Table VI, and the size of the unit cell was adjusted to yield the density of experimental values at the saturated vapor condition.[36] A cutoff distance with the half of the length of the unit cell was applied to all interactions. In solving the PO-DVR equations in the MC runs, the DVR-1D approach was taken for computational efficiency. The effects of the bending vibrations on the H-Xe stretching frequency by the DVR-3D approach will be discussed later.

Table VI. Simulation parameters of temperature (in K), length of the unit cell (in Å), and the corresponding density (in g/cm^3).

	Temperature	Length	Density
Ne matrix	5	21.2	1.75
Ar matrix	15	26.6	1.77
Kr matrix	20	28.2	3.10
Xe matrix	30	30.6	3.70

There are several possible sites at which Ng atom(s) can be substituted by HXeCl. As shown in Figure 4, a couple of Ng atoms along the three possible orientations (<100>, <110>, and <111> in Figure 4) were replaced with a single HXeCl, and these configurations were used to initiate MC simulations. The number of substituted Ng atoms (N_r) was determined from a sensible choice based on the distance between the adjacent Ng atoms along each orientation. After equilibrating the system, a total of 10^7 MC steps were taken to obtain statistical averages.

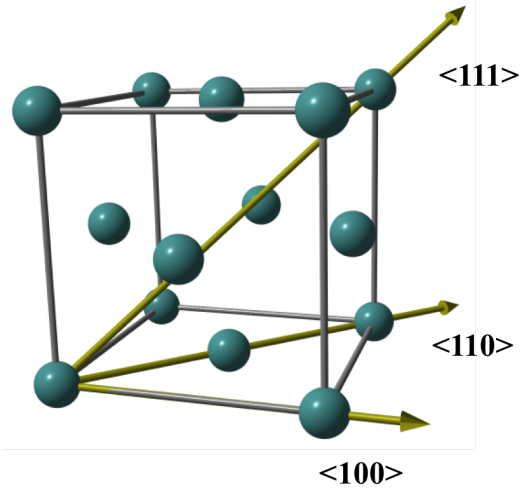

Figure 3. The fcc lattice structure of noble-gas matrix. Three possible orientations are depicted as <100> (four-atomic window), <110> (nearest neighbor), and <111> (three-atomic window).

Table VII shows a summary of the MC simulations, where the peak positions of the H-Xe vibrational spectra are presented. The interaction energy between HXeCl and other surrounding Ng atoms, which is defined as

$$\langle V_{\text{int}} \rangle = \langle E^0_{\text{qm}}(\mathbf{R}) \rangle - E^0 \tag{4}$$

was also calculated to compare the stability of each site. In the above equation, $E^0_{\text{qm}}(\mathbf{R})$ is the vibrational ground-state energy of HXeCl in the presence of surrounding Ng atoms, and E^0 is the corresponding value of the isolated molecule. As seen in the table, the peak positions of the vibrational spectra and interaction energies are different depending on the substituted sites. In all cases, blue shifts from the isolated gas-phase values are observed. The observed blue shifts can be attributed to the packing effect by the surrounding Ng atoms, mainly from Ng atoms that are close to the hydrogen atom.

Table VII. Peak position of the vibrational spectra (in cm^{-1}) of H-Xe stretching motion and interaction energy (in kcal/mol) in solid Ng matrices under PBC. N_r is the number of noble-gas atom(s) substituted with a single HXeCl. Frequency shifts from the isolated gas-phase value (1642 cm^{-1}) are also shown. Simulations for some configurations are not performed (denoted as dashes) since the initial configurations are too packed or too loose to replace with a single HXeCl. The cells shown as "<100>" indicate that after equilibration the configurations become almost identical to the <100> site.

		<100>			<110>			<111>		
	N_r	Freq.	Shift	V_{int}	Freq.	Shift	V_{int}	Freq.	Shift	V_{int}
Ne matrix	2	—			1758	+116	−6.2	1690	+48	−7.1
	3	1728	+86	−6.8	1665	+23	−6.4	—		
Ar matrix	1	1731	+89	−11.5	—			—		
	2	1715	+73	−12.4	1758	+116	−13.8	—		
Kr matrix	1	1770	+128	−12.5	—			1709	+67	−13.8
	2	1708	+66	−14.1	1747	+105	−16.2	—		
Xe matrix	1	1757	+105	−14.6	—			<100>		
	2	—			1730	+88	−17.1	<100>		

When comparing the interaction energies for different substituted sites, the <110> site with N_r = 2 (disubstitutional) exhibits the lowest one except for the Ne matrix, and this <110> configuration would be the most preferred one. The blue shifts of 116, 105, and 88 cm^{-1} are observed in the Ar, Kr, and Xe matrices, respectively, and these shifts are about 2~3 times larger than those estimated from the calculations on isolated HXeCl−Ng complexes (see Table V). In the Ne matrix, the interaction energy is smaller for the disubstitutional <111> site and the blue shift of 48 cm^{-1} is observed, which is the smallest shift among the four matrix environments investigated in this work. The ordering of the amount of blue shifts is now in accord with the experimental observations (Ne < Xe < Kr).

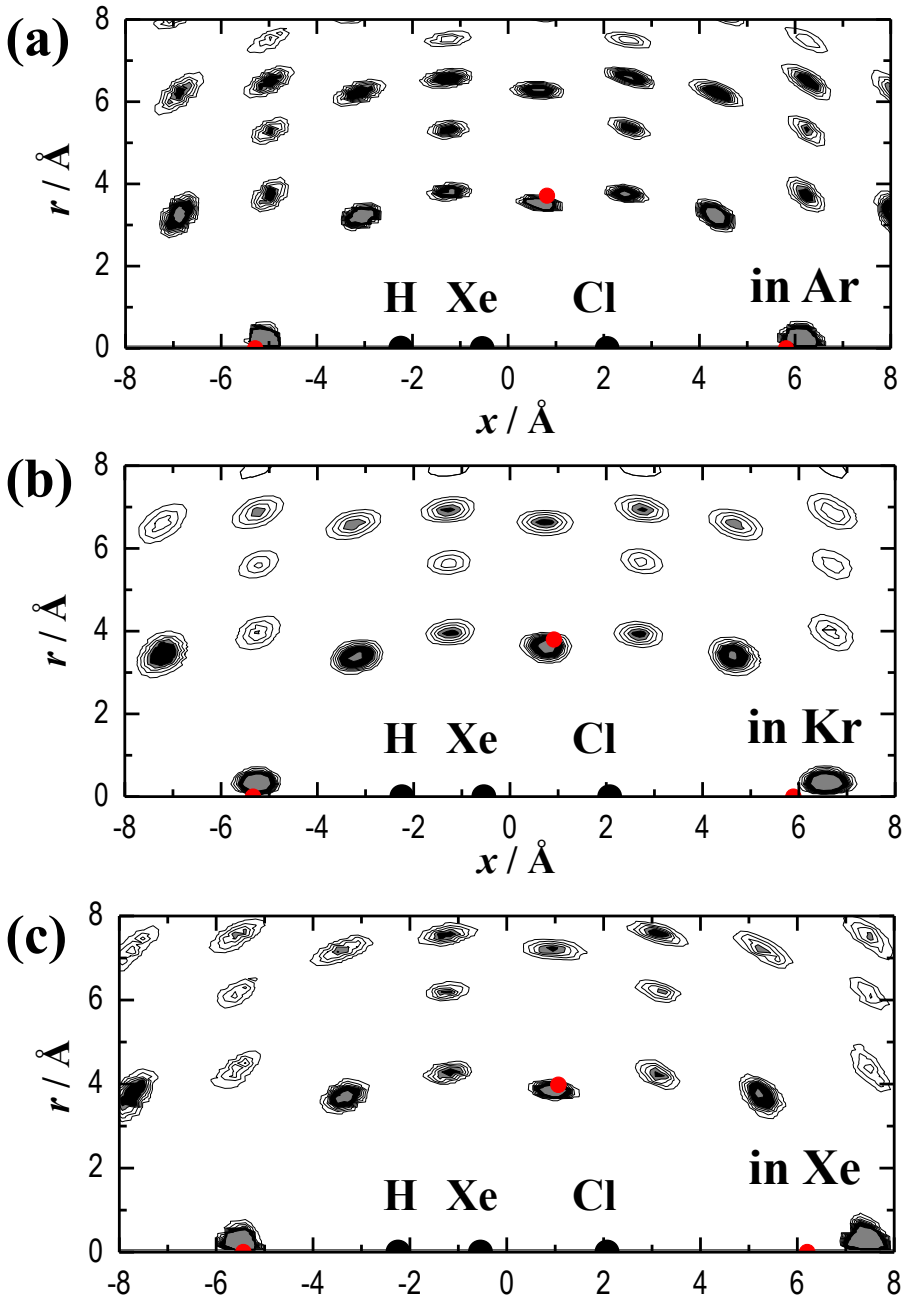

Figure 4. Contour plots of two-dimensional distribution functions of the Ng atoms around HXeCl at the <110> site in the (a) Ar, (b) Kr, and (c) Xe matrices. The *x* and *r* axes are given in unit of Å. The positions of HXeCl are the same as those in Figure 3 (shown as filled circles). The positions of the minimum energy configurations of isolated HXeCl−Ng complexes are shown in (red) filled circles.

Figure 4 shows the contour plots of two-dimensional distribution function of Ng (= Ar, Kr, Xe) atoms around HXeCl for the disubstitutional <110> site, where the *x*-axis is taken as the molecular axis of HXeCl. Here *r* is a radial distance from the *x*-axis and the origin is set to the center-of-mass of HXeCl. Apparently, the positions of the noble-gas atoms are quite localized due to the solid structure of matrices. Recalling the minimum energy structures of the H-side and bent structures of isolated HXeCl−Ng complexes, one can find the Ng atoms at the corresponding configurations in the two-dimensional distribution functions shown in Figure 5. The Cl-side structure is found in the Ar matrix, but it is slightly displaced in the Kr and Xe matrices. As shown in the frequency analysis on the isolated HXeCl−Ng complexes, the H-Xe vibrational frequency is affected by the Ng atoms that are close to the H atom, and the blue shifts are observed at all minimum energy configurations. Since there are several Ng atoms surrounding HXeCl, the calculated large blue shifts in the matrix would be natural consequences. It is interesting to note that in the Ar matrix (Figure 5(a)) the Ar atom in collinear geometry on the H side is located slightly closer to the H atom than that found in the minimum energy structure. This would make the potential energy surface of HXeCl for solving the vibrational energy levels slightly narrower, resulting in further blue shift in the spectrum. This could be partly the reason for the largest blue shift of 116 cm^{-1} observed in the Ar matrix among the other Ng matrices.

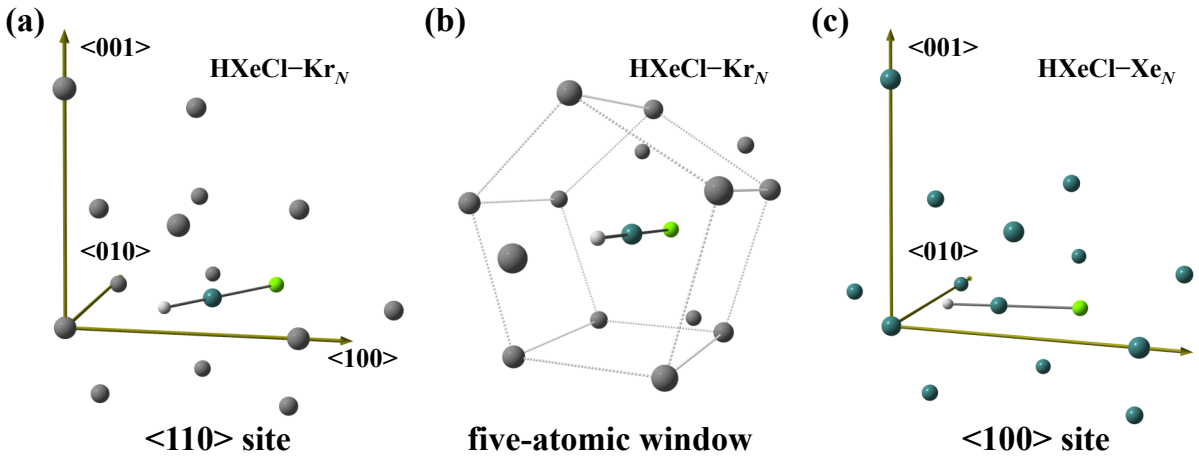

Figure 5. Local structures of (a) the <110> site for HXeCl-Kr$_N$, (b) the five-atomic window site for HXeCl-Kr$_N$, and (c) the <100> site for HXeCl-Xe$_N$.

In order to investigate the distributions of Ng atoms around HXeCl during the crystallization, the MC simulations were also performed for HXeCl−Ng_N (Ng = Ne, Ar, Kr, Xe) clusters with N = 500, as had been done in the previous study.[22] The system temperatures were set to the same values as in the PBC calculations (see Table VI). A total of ten independent simulations were performed for each system. Prior to each simulation, the system was heated up to 150 K under the confinement potential, where the cluster exhibited a liquid-like structure. After a sufficient number of MC steps at 150 K, the cluster was cooled down to the respective system temperature gradually. At these very low temperatures, the cluster was in a somewhat amorphous-like structure, and the configurations of the Ng atoms around HXeCl were different in each simulation due to the technical difficulty of crystallization in MC simulations. The existence of the impurity (i.e. HXeCl) also made it more difficult to form the crystal structure around it. Since there are a huge number of stable structures for clusters even with small number of Ng atoms, each MC run was trapped in one of these configurations. Therefore, the peak positions of vibrational spectra from different MC runs scattered to some extent. Even so, a careful inspection of the configurations around HXeCl made it possible to categorize the results.

Table VIII summarizes the results of MC simulations for vibrational spectra and interaction energies. For the HXeCl−Ar_N, HXeCl−Kr_N, and HXeCl−Xe_N clusters, about half of the MC runs result in the configuration very similar to the <110> site. The vibrational frequency and also interaction energy are close to those obtained under PBC (see Table VII), although the vibrational frequencies are slightly larger (~10 cm^{-1}) for HXeCl−Ar_N and HXeCl−Kr_N than the corresponding values under PBC. For the HXeCl−Ne_N cluster, I were unable to categorize the resulting structures into the specific trapping site in all MC runs since the cluster itself revealed the amorphous structure around HXeCl. Even so, the standard deviations of vibrational frequency and interaction energy of ten independent MC runs are small, which implies that the frequency shift does not depend strongly on the local matrix morphology. For the HXeCl−Ar_N cluster, I were also unable to determine the specific trapping site for the other six MC runs due to the amorphous structure of Ar atoms around HXeCl. For the HXeCl−Kr_N and HXeCl−Xe_N clusters, except for two runs which I could not categorize, the resulting structures are divided into two groups. First, for the HXeCl−Xe_N cluster,

the other trapping site than the <110> site was found to be the <100> site. For the HXeCl−Kr_N cluster, the other trapping site could be referred to as the five-atomic window site, since the five Kr atoms form a ring structure around the molecular axis of HXeCl. The snapshots of typical trapping sites are depicted in Figure 6. Although these multiple configurations are observed for HXeCl−Kr_N and HXeCl−Xe_N, it is safe to say that the <110> site would represent a plausible configuration inside the matrices because of the lower interaction energy.

Table VIII. Average values of peak positions of vibrational spectra (in cm^{-1}) of H-Xe stretching motion and interaction energies (in kcal/mol) for HXeCl−Ng_N clusters from ten independent MC simulations. Frequency shifts from the isolated gas-phase value (1642 cm^{-1}) are also shown. The standard deviations of ten independent MC runs are shown in parenthesis.

	Freq.	Shift	V_{int}	Freq.	Shift	V_{int}	Freq.	Shift	V_{int}
HXeCl−Ne_N	10/10 runs (others)								
	1694 (5.5)	+52	−8.0 (0.16)	—			—		
HXeCl−Ar_N	4/10 runs (<110>)						6/10 runs (others)		
	1771 (15.7)	+129	−13.8 (0.11)	—			1729 (15.8)	+87	−14.0 (0.15)
HXeCl−Kr_N	6/10 runs (<110>)			2/10 runs (five-atomic windows)			2/10 runs (others)		
	1753 (6.9)	+111	−16.5 (0.16)	1798 (0.5)	+156	−16.1 (0.05)	1752 (13.0)	+110	−16.4 (0.10)
HXeCl−Xe_N	4/10 runs (<110>)			4/10 runs (<100>)			2/10 runs (others)		
	1730 (6.4)	+88	−17.4 (0.34)	1751 (4.0)	+109	−15.4 (0.62)	1777 (8.2)	+135	−16.9 (0.31)

For practical consideration of computational cost, the above MC simulations employed the DVR-1D method for solving the vibrational states. As shown in the DVR calculations of an isolated HXeCl, the DVR-3D calculation reduces the vibrational frequency by 23 cm^{-1} in comparison with the DVR-1D calculation. The direct MC simulations by DVR-3D are not practical for available computational resources and therefore I estimate the DVR-3D vibrational frequency by using the configurations of the DVR-1D MC runs. A total of 10^4 configurations are taken from the DVR-1D MC run with equal intervals and the averages of DVR-3D vibrational frequency are calculated.

Table IX summarizes the results of DVR-3D calculations using configurations of DVR-1D MC runs under PBC. It is found that vibrational frequencies decrease by 10~20 cm^{-1} in comparison with the corresponding values of the DVR-1D MC runs, while the shifts from the isolated gas-phase values are similar between DVR-3D and DVR-1D. The decrease in the vibrational frequencies is favorable since they become closer to the experimental values, but the discrepancies in the absolute values with experimental results are still large. The interaction energies are very close to the corresponding values of the DVR-1D runs.

Table IX. Peak position of the vibrational spectra (in cm^{-1}) of H-Xe stretching motion and interaction energy (in kcal/mol) in solid Ng matrices under PBC by the DVR-3D method. N_r is the number of noble-gas atom(s) substituted with a single HXeCl. Frequency shifts from the isolated gas-phase value (1619 cm^{-1}) and the experimental results are also shown.

	Site	N_r	Freq.	Shift	V_{int}	Exp.
Ne matrix	<111>	2	1673	+54	−7.3	1612
Ar matrix	<110>	2	1738	+119	−13.7	—
Kr matrix	<110>	2	1735	+116	−16.3	1664
Xe matrix	<110>	2	1710	+91	−17.1	1649

In summary, the vibrational shifts of H-Xe stretching motion from the isolated HXeCl molecule were calculated to be 116, 105, and 88 cm^{-1} in the Ar, Kr, and Xe matrices at the disubstitutional <110> site under PBC by DVR-1D. The absolute values of the calculated frequencies are overestimated with respect to the experimental ones, even with the inclusion of bending vibrations by DVR-3D. However, when I use the value of 48 cm^{-1} as a blue shift in the Ne matrix (disubstitutional <111> site), the relative blue shifts ($\Delta\nu$ = ν(in Kr matrix) − ν(in Ne matrix) = 57 cm^{-1}, $\Delta\nu$ = ν(in Xe matrix) − ν(in Ne matrix) = 40 cm^{-1}) are quite in good agreement with the corresponding experimental values ($\Delta\nu$ = ν(in Kr matrix) − ν(in Ne matrix) = 52 cm^{-1}, $\Delta\nu$ = ν(in Xe matrix) − ν(in Ne matrix) = 37 cm^{-1}).

Bihary *et al*. reported the red shift of 13 cm^{-1} for H-Xe stretching vibration of HXeCl in Xe matrix by the VSCF approach[35], which is apparently opposite to my calculations. This large discrepancy possibly comes from the different levels of *ab initio* calculations, where the MP2 method was employed in their calculations. simulations employ more reliable level of theory with the CCSD(T) method, and potential energies needed to perform the MC simulations are obtained by the interpolations, while in their work the potential energies between HXeCl and Ng atoms are fitted to some simple analytical functions. It is noted that even complexation with a single noble-gas atom induces a nonnegligible blue shift for the H-Xe stretching vibration. Given the quality of the interaction potential energy surfaces employed in this study, I believe that my simulations successfully reproduce the experimental observations.

Several comments about the improvement of the methodology are in order. First, the quality of the interaction potential can be improved by performing more accurate *ab initio* calculations (e.g. taking the complete basis set limit). As seen, the vibrational shifts depend strongly on the quality of the potential energy. Second, the assumption of the pairwise-additive form for total potential energy should be examined. In the current system, in order to verify this assumption, I compared the interaction energies of a HXeCl−Xe_3 complex between the full *ab initio* calculation and pairwise-additive model, where I placed three Xe atoms at the local minima (H-side,

Cl-side, and bent structures) to form HXeCl−Xe_3. As a result of comparison, differences in the interaction energies between the full *ab initio* calculation and the pairwise-additive model were ~0.003 kcal/mol, and also the H-Xe vibrational frequencies differed only by ~1 cm^{-1} in the DVR-1D approach. Therefore, in the present system the higher-body interactions between HXeCl and Ng atoms would be very small. Of course, the higher-body interactions between Ng atoms should also be examined carefully since it has been reported that the three-body contributions are not negligible in bulk solids ranging from 3% (in neon) to 7% (in xenon) in cohesive energy.[37] The lattice constants, on the other hand, increase only by ~1% with the inclusion of the three-body contributions, which might slightly shift the vibrational frequencies to the red. Finally, quantum effects of noble-gas atoms (e.g. zero-point motions) are not included in the current simulations and in particular quantum nature of neon atoms may not be negligible. The extension of the present work to the quantum treatment of surrounding noble-gas atoms is conceptually straightforward with the use of the imaginary-time path integral formulation of statistical mechanics,[38] provided that the adiabaticity between the vibrational motions of an embedded molecule and lattice vibrations is well maintained. These considerations mentioned above will surely improve the agreement with the experimental results.

4-4. Conclusion

In this study I performed mixed quantum-classical simulations for vibrational spectra of HXeCl in the noble-gas matrix environments (in Ne, Ar, Kr, and Xe) and investigated the origin of spectral shifts in detail. It was found that in all matrix environments the blue shifts of H-Xe stretching vibration with respect to the isolated gas-phase value were observed. The amount of blue shifts was sensitive to local matrix morphology and the ordering of the blue shifts in different matrix environments was in accord with the experimental findings (Ne < Xe < Kr). In my previous work on vibrational shift of XeBeO in Xe and Ar matrices,[22] the red shifts of Be-O vibrational frequency were observed, which was attributed to the attractive interactions between XeBeO and surrounding noble-gas atoms. In the present study of HXeCl, the observed blue shifts would be explained by the packing effects since the vibrational wavefunction of H-X stretching motion is delocalized due to the light mass of hydrogen atom, and therefore it is amenable to the repulsive interactions originating from the surrounding noble-gas atoms.

There are many experimental observations that await a quantitative explanation of the matrix shifts (e.g. unusual matrix shifts of HXeCCH[39]). In many cases, a complexation with a single noble-gas atom cannot explain the observed vibrational shifts. As demonstrated in this work, a realistic modeling of the surrounding matrix environments in conjunction with the high-level *ab initio* calculations will provide a clear physical picture of the matrix effects.

4-5. References

1. L. Pauling, J. Am. Chem. Soc. **55** (5), 1895-1900 (1933).
2. N. Bartlett, Proc. Chem. Soc. (June), 218 (1962).
3. W. Grochala, Chem. Soc. Rev. **36** (10), 1632-1655 (2007).
4. K. O. Christe, Angew. Chem. Int. Ed. **40** (8), 1419-1421 (2001).
5. M. Zhou, L. Andrews and C. W. Bauschlicher, Chem. Rev. **101** (7), 1931-1962 (2001).
6. C. J. Evans and M. C. L. Gerry, J. Chem. Phys. **112** (21), 9363-9374 (2000).
7. Y. Zhao, Y. Gong and M. Zhou, J. Phys. Chem. A **110** (37), 10777-10782 (2006).
8. Y. Taketsugu, T. Noro and T. Taketsugu, J. Phys. Chem. A **112** (5), 1018-1023 (2008).
9. M. Pettersson, J. Lundell and M. Räsänen, J. Chem. Phys. **102** (16), 6423-6431 (1995).
10. L. Khriachtchev, M. Pettersson, N. Runeberg, J. Lundell and M. Räsänen, Nature **406** (6798), 874-876 (2000).
11. L. Khriachtchev, M. Räsänen and R. B. Gerber, Acc. Chem. Res. **42** (1), 183-191 (2008).
12. A. Cohen, M. Y. Niv and R. B. Gerber, Faraday Discuss. **118** (0), 269-280 (2001).
13. R. Baumfalk, N. H. Nahler and U. Buck, J. Chem. Phys. **114** (11), 4755-4758 (2001).
14. N. H. Nahler, M. Fárník and U. Buck, Chem. Phys. **301** (2–3), 173-182 (2004).
15. J. Lundell, G. M. Chaban and R. B. Gerber, Chem. Phys. Lett. **331** (2–4), 308-316 (2000).
16. J. Lundell, G. M. Chaban and R. B. Gerber, J. Phys. Chem. A **104** (34), 7944-7949 (2000).
17. A. Lignell, L. Khriachtchev, M. Pettersson and M. Räsänen, J. Chem. Phys. **118** (24), 11120-11128 (2003).
18. S. Jolkkonen, M. Pettersson and J. Lundell, J. Chem. Phys. **119** (14), 7356-7364 (2003).
19. A. V. Bochenkova, D. A. Firsov and A. V. Nemukhin, Chem. Phys. Lett. **405**

(1–3), 165-171 (2005).

20. J. Ahokas, K. Vaskonen, J. Eloranta and H. Kunttu, J. Phys. Chem. A **104** (42), 9506-9511 (2000).
21. M. Lorenz, M. Räsänen and V. E. Bondybey, J. Phys. Chem. A **104** (16), 3770-3774 (2000).
22. A. Nakayama, K. Niimi, Y. Ono and T. Taketsugu, J. Chem. Phys. **136** (5), 054506-054508 (2012).
23. K. A. Peterson, D. Figgen, E. Goll, H. Stoll and M. Dolg, J. Chem. Phys. **119** (21), 11113-11123 (2003).
24. R. A. Aziz and M. J. Slaman, Chem. Phys. **130** (1–3), 187-194 (1989).
25. J. F. Ogilvie and F. Y. H. Wang, J. Mol. Struct. **273** (0), 277-290 (1992).
26. R. A. Aziz, J. Chem. Phys. **99** (6), 4518-4525 (1993).
27. A. K. Dham, A. R. Allnatt, W. J. Meath and R. A. Aziz, Mol. Phys. **67** (6), 1291-1307 (1989).
28. A. K. Dham, W. J. Meath, A. R. Allnatt, R. A. Aziz and M. J. Slaman, Chem. Phys. **142** (2), 173-189 (1990).
29. J. F. Ogilvie and F. Y. H. Wang, J. Mol. Struct. **291** (2–3), 313-322 (1993).
30. H.-J. Werner, P. J. Knowles, G. Knizia, F. R. Manby, M. Schütz and others.
31. H.-J. Werner, P. J. Knowles, G. Knizia, F. R. Manby and M. Schütz, WIREs Comput. Mol. Sci. **2** (2), 242-253 (2012).
32. J. Echave and D. C. Clary, Chem. Phys. Lett. **190** (3–4), 225-230 (1992).
33. L. D. Gelb, J. Chem. Phys. **118** (17), 7747-7750 (2003).
34. A. Nakayama, N. Seki and T. Taketsugu, J. Chem. Phys. **130** (2), 024107-024110 (2009).
35. Z. Bihary, G. M. Chaban and R. B. Gerber, J. Chem. Phys. **116** (13), 5521-5529 (2002).
36. G. L. Pollack, Rev. Mod. Phys. **36** (3), 748-791 (1964).
37. K. Rościszewski, B. Paulus, P. Fulde and H. Stoll, Phys. Rev. B **60** (11), 7905-7910 (1999).
38. R. P. Feynman, *Statistical Mechanics*. (Addison-Wesley, Redwood City, 1972).
39. H. Tanskanen, L. Khriachtchev, J. Lundell and M. Räsänen, J. Chem. Phys. **125** (7), 074501-074510 (2006).

5. Matrix Site Effects on Vibrational Frequencies of HXeCCH, HXeBr, HXeI, and HXeH: A Hybrid Quantum-Classical Simulation

5-1. Introduction

The last two decades have witnessed a rebirth of interest in the field of noble-gas chemistry mainly due to the discovery of noble-gas hydrides.[1-7] These compounds have a structural formula of HNgY, where Ng is a noble gas atom and Y is an electronegative fragment. The UV photolysis of the HY precursors in the noble-gas matrix produces these HNgY compounds, and a unique electronic character and also the formation process of the HNgY compounds has been the focus of intensive research. The preparation of the noble-gas compounds in large Xe clusters by UV photolysis[8-11] and also by fast electrons and X-ray irradiation in Xe matrix[12, 13] have been reported in the literature as well.

Since these noble-gas hydrides have a strong ion-pair character of the form $(HNg)^{+}Y^{-}$, the resulting large dipole moment and also the weak bonding of these compounds induce sometimes unique solvation effects.[7, 14-16] For example, the vibrational spectroscopic measurements of HXeCl in various noble-gas matrices exhibited the unusual vibrational shift of the H-Xe stretching frequency. The order of the vibrational frequency was observed to be ν(Ne) < ν(Xe) < ν(Kr) < ν(Ar), and it is a non-monotonous function of the matrix dielectric constant.[1, 17-19] These results are in contrast to the "normal" order observed for HCl: ν(Xe) < ν(Kr) < ν(Ar) < ν(Ne) <

ν(gas).[20, 21] The vibrational spectroscopic measurements of HXeCCH and HXeBr in various noble-gas matrices also revealed the unusual vibrational shifts of the H-Xe stretching frequency in the order ν(Ne) < ν(Xe) < ν(Kr) < ν(Ar),[1, 17, 22-25] which is the same as that observed for HXeCl.

There have been several attempts to explain these unique features of the matrix shifts. First, it has been reported that simple calculations of neither HXeY with the polarizable continuum model (PCM) nor single-atom complex HXeY−Ng can reproduce the order of the vibrational shifts.[24-26] Very recently, Kalinowski et al. performed quantum chemical calculations by MP4(SDQ) for HXeCl embedded in a single noble-gas layer cage and successfully reproduced the order of the experimentally observed vibrational shifts.[19] They discussed these calculated shifts in terms of the size available for HXeCl in the cages and its implications for the stresses acting on the embedded HXeCl compound. Curiously, the vibrational frequencies of single-layer calculations by Ne atoms were strongly red-shifted from that of the isolated HXeCl; the shifts were −50 cm^{-1} and −192 cm^{-1} for harmonic and anharmonic calculations, respectively, which are the largest among the single-layer cages of four Ng atoms (Ng = Ne, Ar, Kr, and Xe). This is in contrast to the general observations that the interaction of an embedded compound with Ne atoms is the weakest and that the vibrational frequency in a Ne matrix should be closest to the situation in the gas phase.[27]

At almost the same time as the work of Kalinowski et al.,[19] we have performed the hybrid quantum-classical simulations on the vibrational shift of HXeCl, where the interaction energy between HXeCl and surrounding Ng atoms is modeled by the pairwise-additive form and the pair-interaction energies are determined by high-level quantum chemical calculations.[28] I demonstrated that the experimentally observed vibrational shifts are well reproduced by the simulations and that the local matrix morphology is an important factor affecting the vibrational shifts. The largest shifts were predicted in Ar matrix by my simulation and at that time we were not aware of the experimental results of Ar matrix, but the very recent experimental results are in accord with my prediction.[19] It is noteworthy that two different approaches of Kalinowski et al.,[19] and mine predict the same order of vibrational frequency for HXeCl embedded in four noble-gas matrices.

This paper presents an application of my simulation method to another interesting noble-gas hydrides, HXeCCH, HXeBr, and HXeI in order to provide further information on the matrix shifts. The H-Xe stretching frequencies of HXeCCH[22-25] and HXeBr[1, 17, 25] have recently been reported in four different Ng matrices, and, therefore, a comparison can be made with my simulations. The spectroscopic measurements of HXeI and its complexes with various molecules (i.e. HXeI···HI, HXeI···H_2O) have been reported in Xe matrix before,[1, 29, 30] and very recently the vibrational frequencies of HXeI have been measured in Ar and Kr matrices.[31] It has been shown that the vibrational frequency of HXeI exhibits the order ν(Xe) < ν(Ar) < ν(Kr) and it is slightly different from those observed for HXeCCH, HXeCl, and HXeBr (the experimental results are summarized in Table I). In that paper, we have performed the simulations for HXeI in Ar, Kr, and Xe matrices, and the calculated order is also in accord with the experimental data.[31]

Table I. Experimental H−Xe Stretching Frequencies (in cm^{-1}) of HXeCCH, HXeCl, HXeBr, and HXeI in Various Noble-gas Matrices.[a]

	HXeCCH		HXeCl		HXeBr		HXeI	
	freq.	ref.	freq.	ref.	freq.	ref.	freq.	ref.
Ne matrix	1453	25	1612	17	1453	1, 25	—	—
Ar matrix	1531 (+78)	24	1675 (+63)	19	1541 (+88)	25	1238	31
Kr matrix	1519 (+66)	22	1664 (+52)	1	1527 (+74)	25	1239	31
Xe matrix	1486 (+33)	23	1648 (+36)	1, 18	1504 (+51)	17, 25	1193	1, 31

[a]The shifts, ν(X) − ν(Ne) (X = Ar, Kr, and Xe), were shown in the parentheses.

5-2. Computational Details

The vibrational spectra of HXeCCH, HXeBr, and HXeI in noble-gas (Ng) matrices are computed by the hybrid quantum-classical simulations. The computational methodology is essentially the same as that employed in my previous studies; see refs [28, 32] for details. In its implementation, the total potential energy is represented by the pairwise-additive form,

$$V_{\text{total}} = V_{\text{HXeY}}(q) + \sum_{i=1}^{N} V_{\text{HXeY-Ng}}(q, \mathbf{R}^{(i)}) + \sum_{i<j}^{N} V_{\text{Ng-Ng}}\left(\left|\mathbf{R}^{(i)} - \mathbf{R}^{(j)}\right|\right) \quad (1)$$

where Y = (CCH, Br, or I) and **q** are the normal coordinates of HXeY. $\mathbf{R}^{(i)}$ is the coordinate of *i*-th Ng atoms (Ng = Ne, Ar, Kr, and Xe). $V_{\text{HXeY–Ng}}$ is the interaction potential energy between HXeY and an Ng atom, and $V_{\text{Ng–Ng}}$ is that of Ng dimer. In the simulations, the normal coordinate corresponding to the H-Xe stretching motion, *q*(H-Xe), is only exploited to represent V_{HXeY}, and the other normal coordinates are fixed to zero (denoted as DVR-1D hereafter). The inclusion of the doubly degenerate bending vibrations is only considered for the vibrational analysis of HXeY and HXeY−Ng (denoted as DVR-3D hereafter). In my previous work on HXeCl[28], it has been shown that the inclusion of Xe-Cl stretching vibration causes a negligible effect on the H-Xe stretching frequency (~1cm^{-1}). Also it has been shown that the inclusion of bending motion by DVR-3D reduces the H-Xe stretching frequency by 20-30 cm^{-1} in comparison to DVR-1D, but the frequency shifts from the gas-phase values are close to each other. In a recent paper,[31] we have reported the simulation results of HXeI in Ar, Kr, and Xe matrices and the vibrational frequencies have been calculated by the DVR-3D method. In the present paper, we provide the simulation results by the DVR-1D method and also add the results of HXeI in Ne matrix, and comparative investigation of matrix shifts of HXeCCH, HXeCl, HXeBr, and HXeI in four different Ng matrices is carried out.

In obtaining potential energy surfaces of V_{HXeY} and also pair interaction energies of $V_{\text{HXeY–Ng}}$ and $V_{\text{Ng–Ng}}$, the electronic structure calculations employing the coupled-cluster singles and doubles including the perturbative contributions of

connected triple excitations [CCSD(T)] method are performed. For Kr, Xe, Br, and I atoms, the relativistic pseudopotentials[33] are employed. The cc-pVQZ basis sets are used for H, C, Br, and I atoms, while the aug-cc-pVQZ basis sets are employed for Ng atoms. It is known that the equilibrium distances and binding energies of Ng dimers with these basis sets yield quite reliable values (see ref. [28] for details) and these basis sets were employed in my previous study on HXeCl. All *ab initio* calculations are carried out by the MOLPRO2010.1 package.[34]

The interaction potential energies between HXeY and an Ng atom ($V_{HXeY-Ng}$) are obtained at each point of the normal coordinate of q(H-Xe). The position of the Ng atom is represented by polar coordinates (r, θ), where r is the distance of Ng from the center-of-mass of HXeY and θ is the polar angle measured from the molecular axis of HXeY. The numbers of grid points are 25 and 21 for r and θ, respectively. These potential energies are tabulated for use in the subsequent Monte Carlo (MC) simulations, and in the MC runs the potential energies are evaluated by the interpolation. The number of grid points for the normal coordinate of the H-Xe stretching vibration corresponds to the number of optimized basis set for representing the vibrational wavefunction in the framework of the potential-optimized discrete variable representation (PO-DVR) method.[35] In this work, the optimized basis set is constructed from the solution of the sinc-DVR method[36] for HXeY in the gas phase, and the number of optimized basis set is determined to be 8, where the convergence of the H-Xe fundamental frequency with respect to the number of optimized basis set is confirmed from the preliminary calculations.

The MC simulations are carried out under the periodic boundary condition, and 500 Ng atoms are first placed in a cubic box with the fcc lattice structure. Then, the HXeY compound is inserted into this fcc lattice by removing a couple of Ng atoms. There are several possible sites at which Ng atom(s) can be substituted by HXeY. Three possible orientations in the fcc structures are considered for the insertion of HXeY: <110> (nearest neighbor), <100> (four-atomic window), and <111> (three-atomic windows). The number of substituted Ng atoms (N_r) is determined by a sensible choice based on the distance between the adjacent Ng atoms along each orientation. The simulation parameters are tabulated in Table II, and the size of the

unit cell has been adjusted to yield the density of experimental values at the saturated vapor condition.[37] A cutoff distance with the half the length of the unit cell is applied to all interactions. After equilibrating the system, a total of 10^7 MC steps are taken to obtain statistical averages.

Table II. Simulation Parameters of Temperature (in K), Length of the Unit Cell (in Å), and the Corresponding Density (in g/cm^3).

	temperature	length	density
Ne matrix	5	21.2	1.75
Ar matrix	15	26.6	1.77
Kr matrix	20	28.2	3.10
Xe matrix	30	30.6	3.70

The stability of different sites is compared by using the stabilization energy that is defined as

$$\Delta E = \left\langle E^0 + \sum_{i<j}^{N} V_{\text{Ng-Ng}}\left(\left|\mathbf{R}^{(i)} - \mathbf{R}^{(j)}\right|\right)\right\rangle - E^0_{\text{gas}} - N\mu_{\text{Ng}}, \qquad (2)$$

where E^0 is the vibrational ground-state energy of H-Xe stretching motion in the presence of surrounding Ng atoms that is obtained by the PO-DVR method and E^0_{gas} is the corresponding value in the gas phase. $\langle\ \rangle$ indicates the ensemble average over MC configurations, and μ_{Ng} is the chemical potential of Ng atoms. In order to obtain μ_{Ng}, the MC simulations of pure solid Ng atoms (500 atoms) have been performed and μ_{Ng} is obtained by dividing the ensemble average of total potential energy by the number of Ng atoms in the system.

The vibrational spectra are obtained from the following simple form:

$$I(\omega) = \int d\mathbf{R}\delta(E^1 - E^0 - \omega)\rho(\mathbf{R}) \tag{3}$$

where E^1 is the vibrational first excited-state energy of H-Xe stretching motion in the matrices, and $\rho(\mathbf{R})$ represents the distribution function of the surrounding Ng atoms, which is generated by the MC simulation.

5-3. Results and Discussion

5-3-1. Equilibrium Structures and Vibrational Analysis of HXeCCH, HXeBr, and HXeI

The geometry optimizations were performed for HXeCCH, HXeBr, and HXeI by the CCSD(T) method, and the vibrational frequency analysis followed it. The structural parameters at equilibrium geometries and the harmonic and fundamental frequencies of H-Xe stretching vibration are summarized in Table III and Table IV, respectively (see also Figure 1 for equilibrium structures). The results of HXeCl are also shown in the tables for reference.[28] As seen in the table, the inclusion of anharmonicity induces large red shifts of 85, 137, and 179 cm^{-1} for HXeCCH, HXeBr, and HXeI, respectively. The inclusion of the bending motions by DVR-3D further reduces the frequencies by 16, 28, and 44 cm^{-1} for HXeCCH, HXeBr, and HXeI, respectively, with respect to those by DVR-1D. The natural charge and dipole moments of these compounds are given in Table V, where one can clearly see that the compound exhibits a strong ion-pair character of the form $(HXe)^{+}Y^{-}$, in particular, for HXeCl, HXeBr, and HXeI.

Table III. Equilibrium Bond Length (r_e in Å) of HXeCCH (= H-Xe-C_A-C_B-H), HXeCl, HXeBr, and HXeI.

	r_e(H–Xe)	r_e(Xe–Y)[a]	r_e(C_A-C_B)	r_e(C_B-H)
HXeCCH	1.767	2.350	1.222	1.066
HXeCl[b]	1.703	2.615	—	—
HXeBr	1.723	2.780	—	—
HXeI	1.769	3.001	—	—

[a] Y = C_A, Cl, Br, and I for HXeCCH, HXeCl, HXeBr, and HXeI, respectively

[b] from ref. [28]

Table IV. Harmonic and Fundamental Frequencies (in cm^{-1}) of H-Xe Stretching Vibration for HXeCCH (= H-Xe-C_A-C_B-H), HXeCl, HXeBr, and HXeI.[a]

	harmonic	fundamental (DVR-1D)	fundamental (DVR-3D)
HXeCCH	1582 (H-Xe stretching) 308 (Xe-C_A stretching) 635 (bending)	1497 (H-Xe stretching)	1481 (H-Xe stretching)
HXeCl[b]	1759 (H-Xe stretching) 274 (Xe-Cl stretching) 561 (bending)	1642 (H-Xe stretching)	1619 (H-Xe stretching)
HXeBr	1625 (H-Xe stretching) 192 (Xe-Br stretching) 533 (bending)	1488 (H-Xe stretching)	1460 (H-Xe stretching)
HXeI	1354 (H-Xe stretching) 154 (Xe-I stretching) 491 (bending)	1175 (H-Xe stretching)	1131 (H-Xe stretching)

[a]Harmonic frequencies of Xe-Y (Y = C_A, Cl, Br, and I) stretching and bending vibrations are also shown.

[b]from ref. [28]

Table V. Natural Charges (Q) and Dipole Moments (μ in Debye) of HXeCCH (= H-Xe-C_A-C_B-H_B), HXeCl, HXeBr, and HXeI.

	Q(H)	Q(Xe)	Q(Y[a])	Q(C_B)	Q(H_B)	μ
HXeCCH	−0.151	+0.795	−0.518	−0.344	+0.218	3.19
HXeCl[b]	−0.019	+0.754	−0.735	—	—	6.98
HXeBr	−0.012	+0.710	−0.699	—	—	7.23
HXeI	−0.028	+0.669	−0.642	—	—	7.08

[a]Y = C_A, Cl, Br, and I for HXeCCH, HXeCl, HXeBr, and HXeI, respectively

[b]from ref. [28]

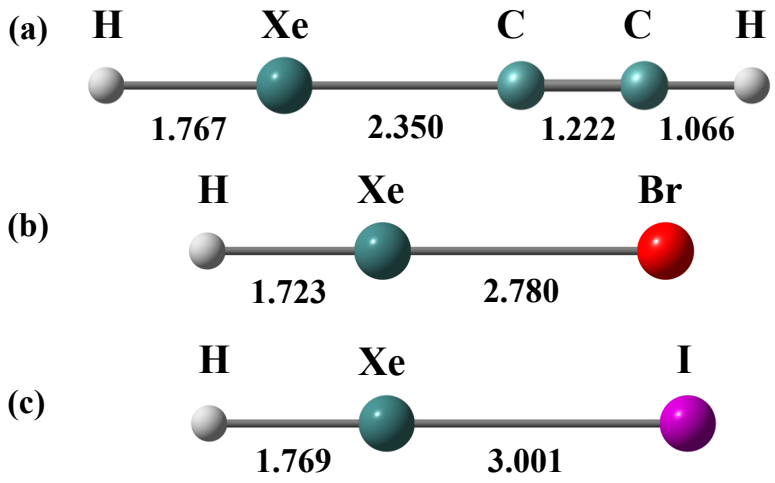

Figure 1. Equilibrium structures of (a) HXeCCH, (b) HXeBr, and (c) HXeI. Bond lengths are given in units of Å.

5-3-2. Equilibrium Structures and Vibrational Analysis of HXeCCH−Ng, HXeBr−Ng, and HXeI−Ng (Ng = Ne, Ar, Kr, Xe)

In this subsection, the equilibrium structures, binding energies, and vibrational frequencies of HXeY−Ng (Y = CCH, Br, I) complexes are examined. Here, the internal coordinates of HXeY are fixed at their equilibrium values of monomer (given in Table III). In fact, the intramolecular structures of HXeY are negligibly perturbed upon formation of HXeY−Ng complexes, and the changes of bond lengths of HXeY between monomer and complexes in the fully relaxed configurations are less than 0.003 Å for all complexes. As expected from the previous works,[28, 38] three minima have been located for all complexes. Two of them are on both sides of HXeY in collinear geometry (H-side and Y-side structures) and the third one is located between and almost equidistant from Xe and Y (bent structure); see Figure 2 for equilibrium structures of HXeCCH−Xe. The structural parameters and binding energies of an Ng atom at these minima are given in Table VI and Table VII, respectively. The strong binding site is the bent structure for all complexes, and in collinear geometry the Y-side structure exhibits a slightly stronger binding energy than the X-side structure, except for HXeCCH−Kr and HXeCCH−Xe. Note that these binding energies are several times larger than those of Ng dimer, where they are 0.095, 0.274, 0.374, and 0.489 kcal/mol for Ne_2, Ar_2, Kr_2, and Xe_2, respectively.[28] Figure 3 shows the two-dimensional contour plot of the potential energy surface of HXeCCH−Xe, where the internal coordinates of HXeCCH are fixed at its equilibrium values of monomer. One can see that the potential energies at the two minima in the collinear geometry are very shallow with respect to the displacement of Xe in the direction perpendicular to the molecular axis.

In Table VII, it is seen that for each Ng the binding energies to HXeY in the bent structure are very similar to each other. Also we find that for each Ng the binding energies in the H-side and Y-side structures are very close to each other for HXeCl−Ng,

HXeBr−Ng, and HXeI−Ng, and it slightly decreases as the halogen atom becomes larger. The binding energies of HXeCl−Ng, HXeBr−Ng, and HXeI−Ng are generally larger than those of HXeCCH−Ng, and it could be explained by the differences in the dipole moment of monomers (see Table V).

Table VI. Structural Parameters (r in Å; θ in deg.) of the Minimum Energy Structures for HXeY−Ng (Y = CCH, Cl, Br, I; Ng = Ne, Ar, Kr, Xe)

Ng	H-side	Y-side	bent	
	r(Ng−H)	r(Y−Ng)	r(Ng−Xe)	θ(Ng−Xe−Y)
HXeCCH−Ng				
Ne	3.176	2.692[a]	3.734	69.2
Ar	3.266	2.995[a]	3.971	67.9
Kr	3.314	3.109[a]	4.088	67.3
Xe	3.443	3.311[a]	4.300	66.3
HXeCl−Ng[b]				
Ne	2.970	3.609	3.715	70.9
Ar	3.045	3.742	3.952	69.9
Kr	3.091	3.815	4.066	69.0
Xe	3.192	3.952	4.295	68.0
HXeBr−Ng				
Ne	3.013	3.758	3.685	77.7
Ar	3.074	3.888	3.954	72.3
Kr	3.107	3.955	4.067	71.8
Xe	3.199	4.092	4.256	71.6
HXeI−Ng				
Ne	3.124	3.979	3.960	71.4
Ar	3.159	4.091	3.962	75.2
Kr	3.180	4.149	4.074	74.7
Xe	3.257	4.281	4.261	74.7

[a]Distance from the nearest H atom.

[b]from ref. [28]

Table VII. Binding Energies (in kcal/mol) of an Ng (Ng = Ne, Ar, Kr, Xe) Atom to HXeY (Y = CCH, Cl, Br, I).

Ng	H-side	Y-side	bent
HXeCCH−Ng			
Ne	0.106	0.176	0.317
Ar	0.314	0.355	0.800
Kr	0.425	0.422	1.010
Xe	0.549	0.478	1.210
HXeCl−Ng[a]			
Ne	0.149	0.181	0.327
Ar	0.447	0.496	0.828
Kr	0.618	0.687	1.052
Xe	0.823	0.865	1.265
HXeBr−Ng			
Ne	0.139	0.167	0.311
Ar	0.434	0.493	0.822
Kr	0.608	0.659	1.049
Xe	0.824	0.837	1.272
HXeI−Ng			
Ne	0.120	0.152	0.283
Ar	0.387	0.466	0.821
Kr	0.551	0.631	1.055
Xe	0.759	0.810	1.286

[a]from ref. [28]

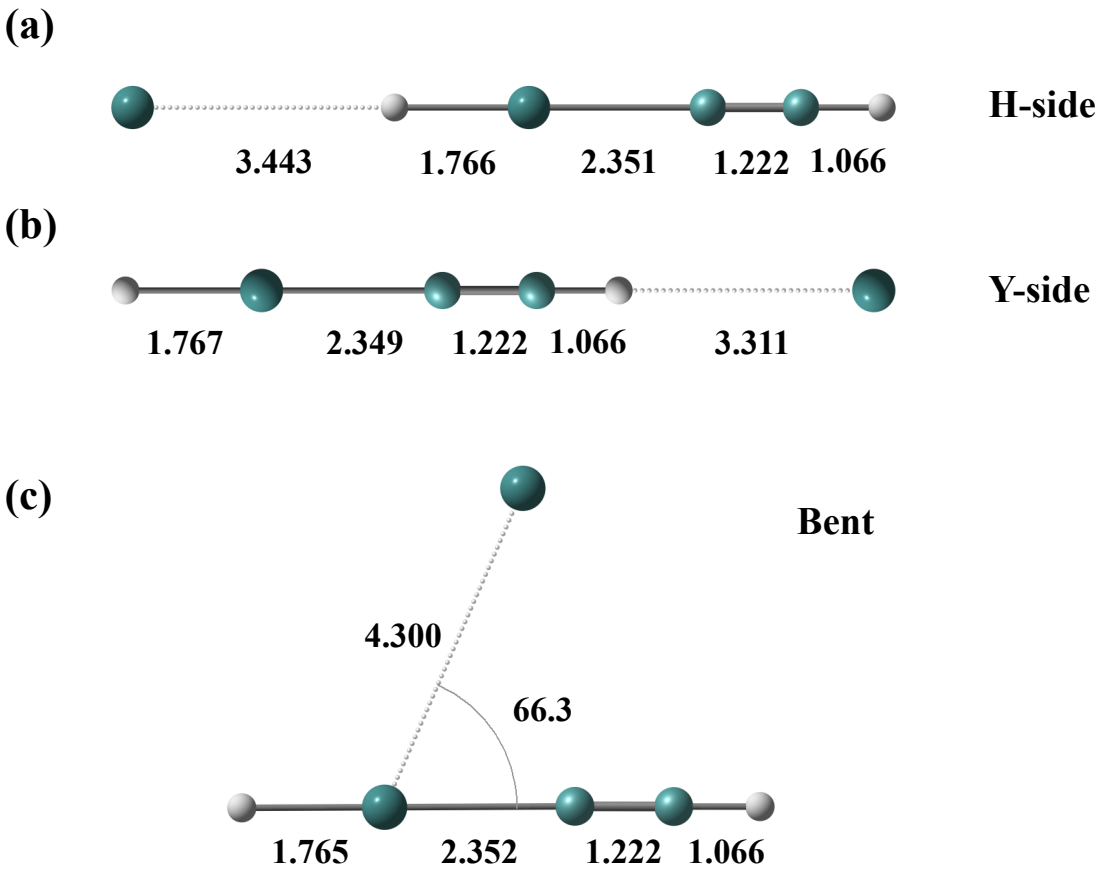

Figure 2. (a-c) Minimum energy structures of HXeCCH−Xe, where the internal coordinates of HXeCCH are fixed at the equilibrium values. Bond lengths are given in units of Å and an angle is given in units of degrees.

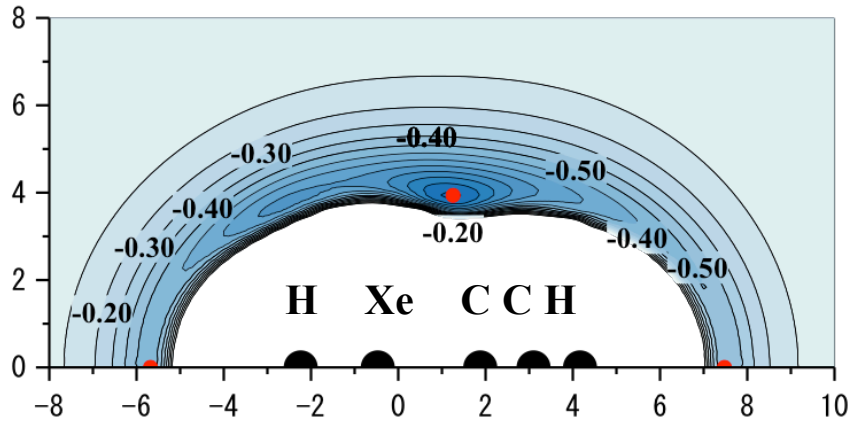

Figure 3. Two-dimensional contour plot of the potential energy surface (in units of kcal/mol) for HXeCCH−Xe. The internal coordinates of HXeCCH are fixed at the equilibrium values in the gas phase, and the origin is set to the center-of-mass of HXeCCH. The positions of the H, Xe, C, C, and H atoms are (−2.237, 0.0), (−0.470, 0.0), (1.879, 0.0), (3.101, 0.0), and (4.167, 0.0), respectively, and they are shown in filled circles. The positions of Xe atoms in the minimum energy structures of the isolated HXeCCH−Xe complex are given in red filled circles.

The frequency analysis is made at these minimum energy structures, and the results are shown in Table VIII. Note that harmonic frequencies are calculated at fully relaxed configurations and that the fundamental frequencies are obtained by fixing the position of Ng atom at the respective minima. As seen in the table, the frequencies of the H-Xe stretching vibration are most strongly affected at the H-side structures, whereas the Y-side and bent structures have a negligible effect on the H-Xe stretching frequency. For the H-side structures, the blue shifts are observed and this shift increases with the Ng size. These blue shifts were previously explained by the enhanced charge separation $(HXe)^{+}Y^{-}$ upon complex formation.[39] The inclusion of anharmonicity induces large red shifts with respect to the harmonic frequencies, but it is also noted that the frequency shifts from the gas-phase values become larger in the anharmonic calculations. The inclusion of the bending motion by DVR-3D further reduces the frequencies, but the frequency shifts from the gas-phase values are very

similar in DVR-3D and DVR-1D calculations with the difference of ~2 cm^{-1}.

The order of H-Xe stretching frequency is ν(Ne) < ν(Ar) < ν(Kr) < ν(Xe) for HXeY−Ng complexes, which is a monotonous function of the matrix dielectric constants, and it is in disagreement with the experimental results in the matrices. The PCM calculations[25] for HXeCCH and HXeBr also predicted the same order of ν(gas) < ν(Ne) < ν(Ar) < ν(Kr) < ν(Xe), simply indicating that the H-Xe stretching frequency becomes higher in matrices with larger dielectric constants, but again, this PCM model cannot explain the experimental observations. As already demonstrated in my previous work,[28] these results indicate that a more realistic modeling of the matrix environments is necessary also for HXeCCH, HXeBr, and HXeI.

Table VIII. Harmonic and Fundamental (DVR-1D and DVR-3D) Frequencies (in cm^{-1}) of H-Xe Stretching Vibration for HXeY−Ng (Y = CCH, Cl, Br, I; Ng = Ne, Ar, Kr, Xe) at the Minimum Energy Structures[a]

Ng	H-side		Y-side		bent	
	freq.	shift	freq.	shift	freq.	shift
HXeCCH−Ng						
harmonic (monomer: 1582 cm^{-1})						
Ne	1585	+3	1583	+1	1584	+2
Ar	1592	+10	1580	−2	1582	0
Kr	1594	+12	1581	−1	1586	+5
Xe	1595	+13	1581	−1	1587	+6
fundamental (DVR-1D) (monomer: 1497 cm^{-1})						
Ne	1504	+7	1498	+1	1497	0
Ar	1514	+17	1496	−1	1499	+2
Kr	1518	+21	1496	−1	1500	+3
Xe	1519	+22	1496	−1	1501	+4

fundamental (DVR-3D) (monomer: 1481 cm^{-1})						
Ne	1488	+7	1481	0	1482	+1
Ar	1498	+17	1481	0	1483	+2
Kr	1501	+20	1481	0	1484	+3
Xe	1502	+21	1481	0	1485	+4
HXeCl−Ng[b]						
harmonic (monomer: 1759 cm^{-1})						
Ne	1765	+6	1759	+0	1759	+0
Ar	1777	+18	1761	+2	1761	+2
Kr	1780	+21	1760	+1	1762	+3
Xe	1780	+21	1759	+0	1768	+9
fundamental (DVR-1D) (monomer: 1642 cm^{-1})						
Ne	1655	+13	1642	+0	1643	+1
Ar	1674	+32	1644	+2	1645	+3
Kr	1677	+35	1644	+2	1647	+5
Xe	1678	+36	1645	+3	1648	+6
fundamental (DVR-3D) (monomer: 1619 cm^{-1})						
Ne	1631	+12	1619	+0	1620	+1
Ar	1648	+29	1621	+2	1622	+3
Kr	1652	+33	1621	+2	1624	+5
Xe	1651	+32	1621	+2	1625	+6
HXeBr−Ng						
harmonic (monomer: 1625 cm^{-1})						
Ne	1633	+8	1625	0	1626	+1
Ar	1648	+23	1625	0	1629	+4
Kr	1653	+28	1626	+1	1630	+5
Xe	1656	+31	1626	+1	1632	+7
fundamental (DVR-1D) (monomer: 1488 cm^{-1})						
Ne	1504	+16	1488	0	1490	+2
Ar	1529	+41	1489	+1	1493	+5
Kr	1537	+49	1490	+2	1494	+6
Xe	1541	+53	1490	+2	1497	+9

fundamental (DVR-3D) (monomer: 1460 cm^{-1})						
Ne	1474	+14	1460	0	1461	+1
Ar	1497	+37	1461	+1	1464	+4
Kr	1506	+46	1461	+1	1466	+6
Xe	1510	+50	1461	+1	1468	+8
HXeI−Ng						
harmonic (monomer: 1354 cm^{-1})						
Ne	1363	+9	1354	0	1353	−1
Ar	1382	+27	1354	0	1360	+6
Kr	1391	+37	1355	0	1362	+8
Xe	1400	+45	1353	−1	1365	+11
fundamental (DVR-1D) (monomer: 1175 cm^{-1})						
Ne	1194	+19	1175	0	1176	+1
Ar	1231	+56	1177	+2	1182	+7
Kr	1247	+72	1177	+2	1184	+9
Xe	1262	+87	1176	+1	1187	+12
fundamental (DVR-3D) (monomer: 1131 cm^{-1})						
Ne	1148	+17	1131	0	1132	+1
Ar	1185	+54	1133	+2	1138	+7
Kr	1202	+71	1133	+2	1140	+9
Xe	1217	+86	1132	+1	1144	+13

[a]Frequency shifts from monomer HXeY are also shown.

[b]from ref. [28]

5-3-3. Hybrid Quantum-Classical Simulations of Vibrational Spectroscopy in Matrix Environments

Table IX shows a summary of the MC simulations, where the peak positions of the vibrational spectra of H-Xe stretching motion are listed. As noted above, the DVR-1D method is employed for solving the vibrational Schrödinger equation in the MC runs. For each orientation of the substitution site, the MC simulations were initiated with different N_r, and we show only the results for the case of lower stabilization energy. As seen in the table, the <110> site exhibits the lower stabilization energy in all cases, and therefore the <110> site would be energetically favored. For the simulations in the Ne matrix, we found that the configurations of Ne atoms around HXeY become rather structureless after equilibration, and therefore the classification by the orientation in the fcc structure is somewhat vague. On the other hand, the configurations of Ar, Kr, and Xe atoms in the matrices are highly structured. For the MC simulations starting from the <110> or <100> site, the HXeY compound does not change its orientation, and the lattice structure of Ar, Kr, and Xe atoms surrounding HXeY is almost maintained. However, when the simulations are initiated from the <111> site, in most cases the compound changes its orientation and the configurations of Ar, Kr, and Xe atoms become almost identical to those of the <100> site after equilibration.

Table IX. Peak Positions of the Vibrational Spectra (in cm^{-1}) of H-Xe Stretching Motion and Stabilization Energy (in kcal/mol) in the Solid Ng Matrices Based on the DVR-1D method[a]

	<110>				<100>				<111>				exp.[c]
	N_r	freq.	shift	ΔE	N_r	freq.	shift	ΔE	N_r	freq.	shift	ΔE	freq.
HXeCCH (gas: 1497 cm^{-1})													
Ne matrix	**3**	**1509**	**+12**	**−0.8**	3	1571	+74	+0.6	2	1557	+60	+0.4	1453
Ar matrix	**2**	**1605**	**+108**	**−9.0**	2	1554	+57	−5.9	2	<100>			1531
Kr matrix	**2**	**1603**	**+106**	**−10.3**	2	1550	+53	−5.2	2	<100>			1519
Xe matrix	**2**	**1564**	**+67**	**−9.5**	1	1590	+93	−4.7	2	<100>			1486
HXeCl[b] (gas: 1642 cm^{-1})													
Ne matrix	**3**	**1665**	**+23**	**−1.1**	3	1728	+86	+6.5	2	1690	+48	+1.1	1612
Ar matrix	**2**	**1758**	**+116**	**−10.2**	2	1715	+73	−5.6	2	<100>			1675
Kr matrix	**2**	**1747**	**+105**	**−11.0**	2	1708	+66	−4.5	2	1709	+67	−4.9	1664
Xe matrix	**2**	**1730**	**+88**	**−9.7**	1	1757	+115	−8.1	2	<100>			1648
HXeBr (gas: 1488 cm^{-1})													
Ne matrix	**3**	**1508**	**+20**	**+0.4**	3	1580	+92	+0.6	2	1544	+56	+0.7	1453
Ar matrix	**2**	**1630**	**+142**	**−10.1**	2	1572	+84	−5.4	2	<100>			1541
Kr matrix	**2**	**1622**	**+134**	**−11.3**	2	1569	+81	−4.3	2	<100>			1527
Xe matrix	**2**	**1599**	**+111**	**−10.5**	1	1647	+159	−6.4	2	<100>			1504
HXeI (gas: 1175 cm^{-1})													
Ne matrix	**3**	**1208**	**+33**	**+2.3**	3	1296	+121	+3.3	2	1300	+125	+3.7	—
Ar matrix	**2**	**1388**	**+213**	**−8.9**	2	1303	+128	−5.1	2	<100>			1238
Kr matrix	**2**	**1392**	**+217**	**−11.1**	2	1306	+131	−4.5	2	<100>			1239
Xe matrix	**2**	**1354**	**+179**	**−11.2**	1	1436	+261	−3.3	2	<100>			1193

[a] N_r is the number of the noble-gas atom(s) substituted with a single HXeY. Frequency shifts from the isolated gas-phase value are also shown. The cells shown as "<100>" indicate that after equilibration the configurations of Ng atoms become almost identical to those of the <100> site.

[b] from ref. [28]

[c] see Table I for references of the experimental data

In all cases shown in Table IX, blue shifts from the isolated gas-phase values are observed. The observed blues shifts are about 2-3 times larger than those estimated from the calculations of isolated HXeY−Ng complexes (see the fundamental frequencies by DVR-1D given in Table VIII). The order of H-Xe stretching frequencies is ν(Ne) < ν(Xe) < ν(Kr) < ν(Ar) for HXeCCH and HXeBr in the <110> site, which is in accord with the experimental observations.[1, 17, 22-25] The same order has been seen for HXeCl in my previous work.[28] The observed order is slightly different for HXeI in the <110> site, where it is ν(Ne) < ν(Xe) < ν(Ar) < ν(Kr), and this order is also in accord with the experiment.[1, 31] It is noted that the order of frequencies is different between the <110> and <100> sites.

The contour plots of two-dimensional distribution functions of Ng (= Ar, Kr, Xe) atoms around HXeCCH and HXeBr are shown in Figure 4 in the <110> site. Here the *x*-axis is taken as the molecular axis of HXeY and *r* is the radial distance from the *x*-axis, and the origin is set to the center-of-mass of HXeY. Due to the highly structured configurations of solid matrices, the positions of the Ng atoms are quite localized. In the same figure, the positions of Ng atoms in the three minimum energy structures of the isolated HXeY-Ng complexes (H-side, Y-side, and bent structures) are also plotted.

As already seen in the frequency analysis of isolated HXeY−Ng complex, the blue shifts are observed in all minimum energy structures of HXeY−Ng, and since there are several Ng atoms surrounding HXeY, the calculated larger blue shifts in the matrix environments are naturally expected. The larger blue shifts are observed in Ar and Kr matrices than in Xe matrix, and this could partly be explained by the observations (Figure 4) that the Ar or Kr atom in collinear geometry on the H-side is found slightly closer to the hydrogen atom than that found in the minimum energy structures of HXeY−Ng, in comparison to the situation in Xe matrix. Similar observations have been seen for HXeCl and HXeI in my previous studies.[28, 31] As shown above in the frequency analysis of HXeY−Ng, the H-Xe stretching frequency is strongly affected by Ng atoms that are close to the hydrogen atom. In this situation, a displacement of the Ng atom toward the hydrogen atom results in a blue shift because the potential energy curve is quite repulsive when the Ng atom is located closer to the hydrogen atom.

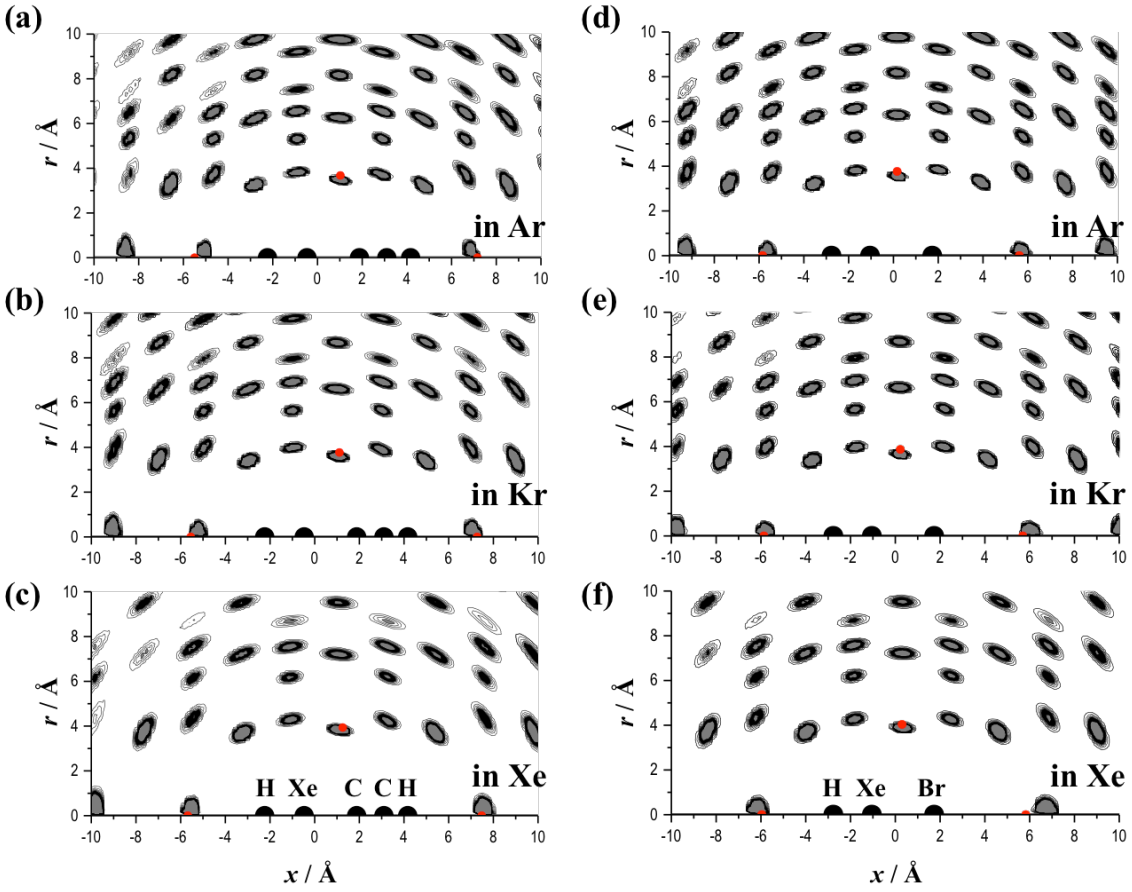

Figure 4. Contour plots of two-dimensional distribution functions of the Ng atoms around (a-c) HXeCCH and (d-f) HXeBr at the <110> site in Ar, Kr, and Xe matrices. The positions of HXeCCH and HXeBr in the minimum energy structure in the gas phase are plotted for reference (shown by black filled circles), where the coordinates of HXeCCH are the same as those in Figure 3 and the positions of the H, Xe, and Br atoms of HXeBr are (−2.761, 0.0), (−1.039, 0.0), and (1.742, 0.0), respectively. The positions of the Ng atoms at the minimum energy structures of isolated HXeCCH−Ng and HXeBr−Ng complexes are also plotted in the figure by red filled circles.

In matrix environments, we find that four Ng atoms are located in the position of the bent structure of HXeY−Ng complex, forming a ring around the molecular axis. Since the bent structure exhibits the strongest binding energy to HXeY (see Figure 3

and Table VII), it is plausible that HXeY adjusts its coordinate along the molecular axis to have these surrounding four Ng atoms at the position of the bent structure. As a result of this, an Ng atom in the collinear geometry on the H-side can be close to the hydrogen atom in the case of Ar or Kr matrix, causing the large blue shifts. Of course, the Ng atom cannot be too close to the hydrogen atom, since there is a quite repulsive potential between the Ng and hydrogen atoms. Therefore, the location of HXeY in matrix environments depends on the delicate balance among stabilization and destabilization arising from the interactions between HXeY and the surrounding Ng atoms. As an another explanation of larger blue shifts in Ar or Kr matrix, which is somewhat related to the above arguments, the Ar cage would be too tight for HXeY, while the Xe cage would be rather relaxed due to the difference in the lattice constants. The Ne matrix exhibits the shortest lattice constant, but the Ne matrix is "soft" due to the weak interaction between Ne atoms, and therefore HXeY would be mildly surrounded by Ne atoms. This is reflected in the small stabilization energies of ca. −1 to 2 kcal/mol in Ne matrix in comparison to those in other matrices (from −9 to −11 kcal/mol) and also in the small frequency shifts from the gas-phase values (from +10 to +30 cm^{-1}). The stress acting on HXeY would be an important factor affecting the vibrational shifts, which was also suggested by Kalinowski et al.[19] I note in passing that the small stabilization energies in Ne matrix (sometimes positive values) can be related to the rather structureless configurations of Ne atoms around HXeY. Also, as pointed out in the previous work,[31] it may be the reason for a failure to prepare HXeI in Ne matrix experimentally.

It is also interesting to note that the frequency shifts from the gas-phase values exhibit a trend $\Delta\nu$(HXeCCH) ≈ $\Delta\nu$(HXeCl) < $\Delta\nu$(HXeBr) < $\Delta\nu$(HXeI) in the same Ng matrix environments. The binding energies of an Ng atom to HXeCl, HXeBr and HXeI are very similar to each other in HXeY−Ng complex and also the stabilization energies are quite close to each other for these compounds in the same Ng matrix, but there are appreciable differences in the frequency shifts. This trend is in agreement with the experiments (see Table I), and it is consistent with the chemical intuition that the matrix effects are stronger for more weakly bound molecules.

Finally, we comment on the reliability of my calculations. First, the potential

energy surfaces of embedded compounds and also the pair interaction potentials are determined by the CCSD(T) method with the (aug-)cc-pVQZ basis sets, which is known to be quite accurate, but of course further improvement would be possible (e.g., taking the complete basis set limit). I speculate that discrepancies in absolute values of frequencies between experiments and my calculations (50-150 cm^{-1}) stem from mainly the quality of potentials. The large discrepancies were found for HXeI, and this might be related to the weakness of the chemical bond of this compound. Second, the higher-body interactions between Ng atoms should be examined carefully because it has been reported that the three-body contributions are not negligible in bulk solids ranging from 3% (in Ne) to 7% (in Xe) in cohesive energy.[40] The inclusion of the three-body contributions also increases the lattice constants by ~1%, which might slightly shift the vibrational frequencies to the red. Lastly, the present MC simulations are performed using the DVR-1D method for practical consideration of computational cost. The vibrational frequencies of isolated HXeY−Ng complexes show that the H-Xe stretching frequencies decrease by ~20 cm^{-1} with the inclusion of the bending motions by DVR-3D, but the shifts from the gas-phase values are very similar in DVR-1D and DVR-3D calculations with the difference of at most 4 cm^{-1} (see Table VIII). In my previous study of HXeCl,[28] the MC simulations employing DVR-3D have predicted the frequencies of 1738, 1735, and 1710 cm^{-1} in Ar, Kr, and Xe matrices, respectively, and therefore the shifts from the gas-phase values are +119, +116, and +91 cm^{-1}, which is close to the results by DVR-1D shown above. For HXeI, the shifts from the gas-phase values in DVR-3D calculations were +226, +230, and +196 cm^{-1} in Ar, Kr, and Xe matrices,[31] respectively, and these shifts are slightly larger than those by DVR-1D calculations (see Table IX). I expect that the differences in relative shifts between DVR-1D and DVR-3D are smaller for HXeCCH and HXeBr than HXeI considering the trend in the vibrational frequencies of these compounds, and the order of the vibrational frequency will be almost certainly unchanged.

5-4. Conclusions and Outlook

The hybrid quantum-classical simulations are performed to investigate the unusual vibrational spectral shifts of noble-gas hydrides, HXeCCH, HXeBr, and HXeI in matrix environments (in Ne, Ar, Kr, and Xe matrices). It is demonstrated that the H-Xe stretching frequencies are blue-shifted from the isolated gas-phase values in all matrix environments and that the amounts of blue shifts are a non-monotonous function of the matrix dielectric constants. The calculated results reproduce the experimentally observed shifts quite successfully.

My calculations have clarified that the local matrix morphology is an important factor affecting the vibrational shifts and that a realistic modeling of the surrounding matrix environments is essential to reproduce the unusual vibrational shifts observed in the experiments. The orders of the H-Xe stretching frequencies are ν(Ne) < ν(Xe) < ν(Kr) < ν(Ar) for HXeCCH and HXeBr and ν(Ne) < ν(Xe) < ν(Ar) < ν(Kr) for HXeI, and therefore the order of the matrix shifts depends on the embedded compound. Also my calculations have shown that the matrix shifts from the gas-phase values exhibit the trend $\Delta\nu$(HXeCCH) ≈ $\Delta\nu$(HXeCl) < $\Delta\nu$(HXeBr) < $\Delta\nu$(HXeI) in the same Ng matrix environments. This is consistent with the experimental results and also with the speculation that the stronger matrix effects are observed for more weakly bound molecules.

The theoretical investigations on vibrational spectra in other matrices such as N_2 or CO_2 will further enhance my understanding of the matrix shifts. In N_2 or CO_2 matrices, the large matrix shifts were observed experimentally due to the dipole-quadrupole interactions between HXeY and matrix molecules.[41] The elucidation of these shifts is also an exciting future challenge.

5-5. References

1. M. Pettersson, J. Lundell, and M. Räsänen, *J. Chem. Phys.*, 1995, **102**, 6423-6431.
2. V. I. Feldman and F. F. Sukhov, *Chem. Phys. Lett.*, 1996, **255**, 425-430.
3. M. Pettersson, J. Lundell, and M. Räsänen, *Eur. J. Inorg. Chem.*, 1999, **1999**, 729-737.
4. L. Khriachtchev, M. Pettersson, N. Runeberg, J. Lundell, and M. Räsänen, *Nature*, 2000, **406**, 874-876.
5. L. Khriachtchev, M. Pettersson, A. Lignell, and M. Räsänen, *J. Am. Chem. Soc.*, 2001, **123**, 8610-8611.
6. R. B. Gerber, *Annu. Rev. Phys. Chem.*, 2004, **55**, 55-78.
7. L. Khriachtchev, M. Räsänen, and R. B. Gerber, *Acc. Chem. Res.*, 2009, **42**, 183-191.
8. R. Baumfalk, N. H. Nahler, and U. Buck, *J. Chem. Phys.*, 2001, **114**, 4755-4758.
9. N. H. Nahler, M. Fárník, and U. Buck, *Chem. Phys.*, 2004, **301**, 173-182.
10. U. Buck and M. Fárník, *Int. Rev. Phys. Chem.*, 2006, **25**, 583-612.
11. V. Poterya, O. Votava, M. Fárník, M. Ončák, P. Slavíček, U. Buck, and B. Friedrich, *J. Chem. Phys.*, 2008, **128**, 104313.
12. V. I. Feldman, F. F. Sukhov, A. Y. Orlov, and I. V. Tyulpina, *J. Am. Chem. Soc.*, 2003, **125**, 4698-4699.
13. V. I. Feldman, A. V. Kobzarenko, A. Y. Orlov, and F. F. Sukhov, *Low Temp. Phys.*, 2012, **38**, 766-773.
14. J. Lundell, G. M. Chaban, and R. B. Gerber, *Chem. Phys. Lett.*, 2000, **331**, 308-316.
15. J. Lundell, G. M. Chaban, and R. B. Gerber, *J. Phys. Chem. A*, 2000, **104**, 7944-7949.
16. A. Lignell, L. Khriachtchev, M. Pettersson, and M. Räsänen, *J. Chem. Phys.*, 2003, **118**, 11120-11128.
17. M. Lorenz, M. Räsänen, and V. E. Bondybey, *J. Phys. Chem. A*, 2000, **104**, 3770-3774.
18. J. Ahokas, K. Vaskonen, J. Eloranta, and H. Kunttu, *J. Phys. Chem. A*, 2000, **104**, 9506-9511.

19. J. Kalinowski, R. B. Gerber, M. Räsänen, A. Lignell, and L. Khriachtchev, *J. Chem. Phys.*, 2014, **140**, 094303.
20. A. J. Barnes, H. E. Hallam, and G. F. Scrimshaw, *Trans. Faraday Soc.*, 1969, **65**, 3159-3171.
21. A. J. Barnes, in *Vibrational Spectroscopy of Trapped Species*, ed. H. E. Hallam, John Wiley and Sons, London, 1973, pp. 133-177.
22. L. Khriachtchev, H. Tanskanen, J. Lundell, M. Pettersson, H. Kiljunen, and M. Räsänen, *J. Am. Chem. Soc.*, 2003, **125**, 4696-4697.
23. H. Tanskanen, L. Khriachtchev, J. Lundell, and M. Räsänen, *J. Chem. Phys.*, 2004, **121**, 8291-8298.
24. H. Tanskanen, L. Khriachtchev, J. Lundell, and M. Räsänen, *J. Chem. Phys.*, 2006, **125**, 074501-074510.
25. M. Tsuge, A. Lignell, M. Räsänen, and L. Khriachtchev, *J. Chem. Phys.*, 2013, **139**, 204303.
26. G. Liu, Y. Zhang, Z. Wang, Y. Wang, X. Zhang, and W. Zhang, *Comput. Theor. Chem.*, 2012, **993**, 118-124.
27. M. E. Jacox, *Chem. Soc. Rev.*, 2002, **31**, 108-115.
28. K. Niimi, A. Nakayama, Y. Ono, and T. Taketsugu, *J. Phys. Chem. A*, 2014, **118**, 380-387.
29. M. Tsuge, S. Berski, M. Räsänen, Z. Latajka, and L. Khriachtchev, *J. Chem. Phys.*, 2013, **138**, 104314.
30. M. Tsuge, S. Berski, M. Räsänen, Z. Latajka, and L. Khriachtchev, *J. Chem. Phys.*, 2014, **140**, 044323.
31. C. Zhu, K. Niimi, T. Taketsugu, M. Tsuge, A. Nakayama, and L. Khriachtchev, *J. Chem. Phys.*, 2015, **142**, 054305.
32. A. Nakayama, K. Niimi, Y. Ono, and T. Taketsugu, *J. Chem. Phys.*, 2012, **136**, 054506.
33. K. A. Peterson, D. Figgen, E. Goll, H. Stoll, and M. Dolg, *J. Chem. Phys.*, 2003, **119**, 11113-11123.
34. H.-J. Werner, P. J. Knowles, G. Knizia, F. R. Manby, M. Schütz, and others, *MOLPRO, version 2010.1, a package of ab initio programs*.
35. J. Echave and D. C. Clary, *Chem. Phys. Lett.*, 1992, **190**, 225-230.
36. D. T. Colbert and W. H. Miller, *J. Chem. Phys.*, 1992, **96**, 1982-1991.

37. G. L. Pollack, *Rev. Mod. Phys.*, 1964, **36**, 748-791.
38. L. Khriachtchev, A. Lignell, J. Juselius, M. Räsänen, and E. Savchenko, *J. Chem. Phys.*, 2005, **122**, 014510-014517.
39. A. Lignell and L. Khriachtchev, *J. Mol. Struct.*, 2008, **889**, 1-11.
40. K. Rościszewski, B. Paulus, P. Fulde, and H. Stoll, *Phys. Rev. B*, 1999, **60**, 7905-7910.
41. M. Tsuge, S. Berski, R. Stachowski, M. Räsänen, Z. Latajka, and L. Khriachtchev, *J. Phys. Chem. A*, 2012, **116**, 4510-4517.

6. HXeI and HXeH in Ar, Kr, and Xe Matrices: A Hybrid Quantum-Classical Simulation

6-1. Introduction

Noble-gas hydrides have the general form HNgY (Ng is a noble-gas atom and Y is an electronegative group). These electronic state are characterized by an ion-pair character $(HNg)^+Y^-$, which results in a strong IR absorption intensity (~1000 km mol^{-1} or higher) of the H–Ng stretching mode.[1] As an exception, the HXeH molecule does not contain an electronegative fragment.[2] These metastable molecules can be prepared through the reaction of the neutral fragments H + Ng + Y → HNgY, which are initiated by UV photolysis of an HY precursor in a Ng matrix and subsequent thermal mobilization of the H atoms. Due to weak bonding and large dipole moments, the HNgY molecules are strongly affected by interaction with other species (N_2, CO_2, H_2O, *etc*.). All experimentally prepared HNgY complexes exhibit blue shifts of the H–Ng stretching mode as compared to the monomers because of an increase of the $(HNg)^+Y^-$ charge separation.[3]

In most cases, the HNgY molecules have been studied in Ng matrices (with the same Ng).[1] However, in some studies, the HNgY molecules were synthesized in "foreign" matrices, of a different material Ng′ (see Table I).[4-9] It makes sense to assume that the H–Ng stretching frequency increases with the strength of the interaction of HNgY with the environment. From this point of view, the relatively high frequencies of this mode observed in N_2 and CO_2 matrices are expectable due to the dipole-quadrupole interactions between HNgY and matrix molecules. The lowest frequencies are observed in a Ne matrix, and this can be owing to a weak interaction of the embedded molecules with the Ne atoms, which is well accepted in matrix isolation.[10] More intriguing is the

situation with Ar, Kr, and Xe matrices where the frequency order ν(Xe) < ν(Kr) < ν(Ar) has been observed, which is anomalously dependent on the dielectric constants of the noble-gas solids. Intuitively, the opposite order of the frequencies should take place; at least, the polarizable continuum model (PCM) predicts the opposite order, indeed.[8] The calculations of the 1:1 complexes do not solve the problem either.[6] It becomes clear that the bigger HNgY@Ng′$_n$ systems and more sophisticated computational methods are required for the adequate description of the matrix effect. Concerning HXeH, Tsuge *et al*. have recently suggested based on the experiments in an N_2 matrix that the matrix effect on this molecule should be relatively weak due to the symmetric structure of this molecule.[8]

The first positive theoretical results have been recently obtained for noble-gas hydrides in different environments. The DFT (B3LYP-D) study done by Cohen *et al.* has been focused on simulations of HXeBr in CO_2 and Xe matrices, and a good agreement with the experimental vibrational spectra has been found for clusters containing 17 matrix particles.[11] Kalinowski *et al.* have performed MP4(SDQ) calculations of HXeCl in noble-gas clusters, and the obtained order of the H–Xe stretching frequencies ν(Ne) < ν(Xe) < ν(Kr) < ν(Ar) is in agreement with the experiment.[9] Kalinowski *et al.* have suggested that the reason for the frequency order ν(Xe) < ν(Kr) < ν(Ar) is in different stress states of the molecules in the cages due to the different cage sizes. The H−Xe stretching frequencies of HXeCl in all matrix environments are surprisingly found to be red-shifted from the value obtained in vacuum. In another study, Niimi *et al.* have reported hybrid quantum-classical simulations on the vibrational shift of the same molecule HXeCl in different matrices (Ne, Ar, Kr, and Xe) where the interaction energy between HXeCl and surrounding Ng atoms is modeled by the pairwise-additive form.[12] It has been found that the order of the H–Xe stretching frequencies agrees with the experimental order ν(Ne) < ν(Xe) < ν(Kr) < ν(Ar). On the other hand, the H−Xe stretching frequencies are calculated to be blue-shifted from the isolated gas-phase value in all matrix environments, which is in contrast to the results by Kalinowski *et al.* It is interesting to note that the two different approaches of Kalinowski *et al.* and Niimi *et al.* lead to the same order of the H–Xe stretching frequency for HXeCl embedded in the four noble-gas solids. The difference between the results of these two studies is the matrix shift with respect to the molecule

in vacuum. Summarizing the experimental and theoretical data existing before the present work, this order of frequencies ν(Ne) < ν(Xe) < ν(Kr) < ν(Ar) seems to be common for noble-gas hydrides.

The present work intends to develop the recent experimental and theoretical success in studies of noble-gas hydrides in foreign matrices. The target molecule in this research is HXeI and HXeH in Ar, Kr and Xe matrices. These molecules are interesting in several respects. HXeI has one of the weakest chemical bonding among the noble-gas hydrides so that a very strong matrix effect can be expected. HXeH is, in fact, a specific noble-gas hydride because of the absence of the electronegative fragment Y, and the expectations of the matrix effect on this molecule are unclear. In the present work, the vibrational properties of these systems are successfully modeled by hybrid quantum-classical simulations.

Table I. Experimental frequencies of the H–Xe stretching mode (in cm−1) of noble-gas hydrides in different matrices.[a]

	Ne	Ar	Kr	Xe	N_2	CO_2
HXeCl	1612	1675	1664	1648	-	-
HXeBr	1453	1541	1527	1504	1625	1646
HXeCCH	1453	1531	1519	1486	1529.5	-
HXeH	-	-	-	1166	1175	-
HKrCl	-	1482.5	1476	-	-	-

[a] Data from Refs. 2,4-9**.** The strongest bands are presented.

6-2. Computational Details

The computational methodology used in the present study is essentially the same as that employed in my previous studies, and the details can be found elsewhere.[12,13] The total potential energy of the system is represented as a pairwise additive form and is given by

$$V_{\text{total}} = V_{\text{HXeY}} + \sum_{i=1}^{N} V_{\text{HXeYL Ng}} + \sum_{i<j}^{N} V_{\text{NgL Ng}} \quad (1)$$

where V_{HXeY} is the potential energy of HXeY (Y = I or H) and N is the number of surrounding Ng atoms, $V_{\text{HXeY...Ng}}$ is the interaction potential energy between HXeY and an Ng atom, and $V_{\text{Ng...Ng}}$ is that of Ng dimers. The normal coordinates of HXeY are utilized to represent the potential energy of V_{HXeY}, and the interaction energy of $V_{\text{HXeY...Ng}}$ is determined at each point of the normal coordinates of HXeY. For HXeI, three normal coordinates corresponding to the H−Xe stretching and the doubly degenerate bending vibrations are exploited to represent V_{HXeY}. The Xe−I stretching motion is neglected, and the corresponding normal coordinate is fixed to zero. It has been found that the inclusion of the Xe−I stretching vibration causes a negligible effect on the H−Xe vibrational frequency (~1 cm^{-1}); see also my previous work on HXeCl.[12] For HXeH, the normal coordinates of the asymmetric and symmetric vibrational modes are used, while the bending motion is neglected. The inclusion of the bending motion is of course preferable, but it is computationally demanding to perform simulations with this approach since four vibrational modes are involved. In my previous work on HXeCl, the inclusion of bending motion reduces the H−Xe vibrational frequency by 20-30 cm^{-1} in comparison to the case that neglects the bending motion, but the frequency shifts from the gas-phase values are very similar between these two cases.[12] I expect a similar trend for the simulations of HXeH.

Ab initio calculations by the coupled-cluster singles and doubles including the perturbative contributions of connected triple excitations [CCSD(T)] method are performed to obtain the potential energy surface of V_{HXeI} and also pair interaction energies of $V_{\text{HXeI...Ng}}$ and $V_{\text{Ng...Ng}}$. For HXeH, the CCSD(T) method provides a poor description at long distances in the symmetric stretching modes; therefore, the complete active space second-order perturbation theory (CASPT2) method is used to calculate the

potential energy surface of V_{HXeH}. The active space for a reference state-averaged complete active space self-consistent field (SA-CASSCF) wavefunction is composed of 10 electrons and 9 orbitals, and the active orbitals include all valence orbitals (H: 1s and Xe: 5s, 5p) and three virtual orbitals belonging to the Xe atom. Note that the pair interaction $V_{HXeH\cdots Ng}$ is determined by the CCSD(T) method. The cc-pVQZ basis sets are used for H and I atoms, and the aug-cc-pVQZ basis sets are employed for Ng atoms (Ng = Ar, Kr, and Xe). For Kr, Xe and I atoms, the relativistic pseudopotentials are employed.[14] All *ab initio* calculations have been carried out by the MOLPRO2010.1 package.[15]

In the calculations of the potential energy surfaces of $V_{HXeY\cdots Ng}$, the position of the Ng atom is represented by polar coordinates (r, θ, φ), where r is the distance of Ng from the center-of-mass of HXeY, θ is the polar angle measured from the molecular axis of HXeY, and φ is the azimuthal angle measured from the plane of the bending vibration (φ is required only for the HXeI···Ng interaction because the bending motion is neglected for HXeH). The numbers of grid points are M_r = 25, M_θ = 21, and M_φ= 4 for HXeI, and M_r = 27 and M_θ = 21 for HXeH.

The potential-optimized discrete variable representation (PO-DVR) method is used to solve the vibrational Schrödinger equations of HXeY in the presence of surrounding Ng atoms.[16] The numbers of optimized basis sets, which are obtained by the solution of the sinc-DVR method for HXeY in the gas phase, are 8 and 6 for H–Xe stretching and bending motions of HXeI, respectively, and 8 and 6 optimized basis sets are used for asymmetric and symmetric vibrational motions, respectively, for HXeH. The convergence of the fundamental (anharmonic) frequency of the H–Xe stretching vibration with respect to the number of optimized basis sets was confirmed by the preliminary calculations.

The simulations of the noble-gas hydrides in matrices are carried out under the periodic boundary condition, and 500 Ng atoms were first placed in a cubic box with the *fcc* lattice structure. Then, the HXeI and HXeH molecules are inserted into this *fcc* lattice by removing a couple of Ng atoms. Three possible orientations in the *fcc* lattice structures are considered for the insertion of HNgY: <100> (four-atomic window), <110> (nearest neighbor), and <111> (three-atomic windows). The number of substituted Ng atoms (N_r) was determined from a sensible choice based on the distance

between the adjacent Ng atoms along each orientation. After equilibrating the system, a total of 10^7 MC steps were taken to obtain statistical averages. The temperatures were set to 15, 20, and 30 K for Ar, Kr, and Xe matrixes, respectively, following my previous studies.[12] These temperatures are slightly different from the experimental conditions considered above, but I have found that the peak positions of the H–Xe stretching frequencies do not change significantly as long as the surrounding Ng atoms keep a solid structure.

The stability of different sites was compared by using the stabilization energy defined as

$$\Delta E = \left\langle E^0 + \sum_{i<j}^{N} V_{\text{Ng-Ng}} \right\rangle - E^0_{\text{gas}} - N\mu_{\text{Ng}} \tag{2}$$

where E^0 is the vibrational ground-state energy of the embedded molecule in the presence of surrounding Ng atoms obtained by the PO-DVR method, and $\langle \text{L} \rangle$ indicates the ensemble average over MC configurations, E^0_{gas} is the vibrational ground-state energy of the embedded molecule in the gas phase, and μ_{Ng} is the chemical potential of Ng atoms. In order to obtain μ_{Ng}, the MC simulations of pure solid Ng atoms (500 atoms) have been performed and μ_{Ng} is calculated by dividing the ensemble average of total potential energy by the number of Ng atoms in the system.

For each orientation of the substitution site, the MC simulations were initiated with different N_{r}, and I show only the results for the case of a lower stabilization energy. I have also found that the simulations starting from the <111> site result in the configurations which are almost identical to those of the <100> site after equilibration; therefore, only the results for the <110> and <100> sites are presented below.

6-3. Results and Discussion

6-3-1. HXeY monomers and the HXeY···Ng complexes (Y = I and H; Ng = Ar, Kr, and Xe)

The structural parameters of the equilibrium geometries and the harmonic and fundamental (anharmonic) frequencies of the H–Xe stretching vibration are summarized in Table II (see Figure 1 for the equilibrium structures). For the harmonic frequency of HXeI, good agreement is found with the CCSD(T) calculations by Tsuge *et al.* (1327.2 cm^{-1}).[17] The anharmonic calculation by the DVR approach decreases the H–Xe vibrational frequency by ~200 cm^{-1}. For HXeH, the equilibrium bond length is in good agreement with the previous calculations,[17-19] but the vibrational frequencies are scattered to some extent depending on the computational methods. I find that the asymmetric vibrational frequency is decreased by ~80 cm^{-1} by the treatment of anharmonic vibrational motion.

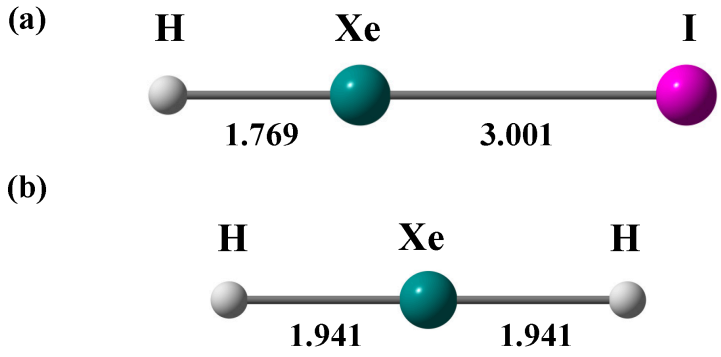

Figure 1. Equilibrium structures of (a) HXeI and (b) HXeH. The bond lengths are given in Å.

Table II. Equilibrium bond lengths (Å), harmonic and fundamental (anharmonic) frequencies (in cm^{-1}) of HXeI and HXeH.

	Bond lengths	Harmonic	Fundamental
HXeI	1.769 (H–Xe) 3.001 (Xe–I)	1354 (H–Xe stretching) 154 (Xe–I stretching) 491 (bending)	1131 (H–Xe stretching)
HXeH	1.941 (H–Xe)	1211 (asymmetric) 1095 (symmetric) 721 (bending)	1138 (asymmetric)

Next, I investigate the HXeY···Ng (Y = I and H) complexes with fixed internal coordinates of HXeY. In fact, the intramolecular structures of HXeY are negligibly perturbed upon formation of the HXeY···Ng complexes and the changes of the bond lengths of HXeY between the monomer and complexes in the fully relaxed configurations are less than 0.003 Å for all complexes. As expected from the previous works,[12,20] three minima have been located for HXeI (Figure 2a-c). In two cases, the Ng atom is located at the sides of HXeI in a collinear geometry (H-side and I-side structures) and in the third structure, it is located between and almost equidistant from the Xe and I atoms (bent structure). For the minimum energy structures of the HXeH···Ng complex, the collinear and bent configurations are obtained (see Figure 2d,e). The structural parameters and the binding energies of these complexes are given in Table III and Table IV. In all cases, the strongest interaction is observed for the bent structures. These binding energies are larger than those of Ng dimers (0.274, 0.374, and 0.489 kcal mol^{-1} for the Ar_2, Kr_2, and Xe_2 dimers, respectively).[12] The binding energies of Ng atoms to HXeCl are slightly larger (by 5 to15 %) than those to HXeI for the H-side and Y-side structures. For the bent structure, the binding energies of the HXeI···Ng and HXeCl···Ng complexes are very similar. Figure 3 shows two-dimensional contour plots of the potential energy surfaces of the HXeI···Xe and HXeH···Xe complexes where the internal coordinates of HXeI or HXeH are fixed to

those of their monomer structures.

The frequency analysis is done for the HXeH···Ng complexes by fixing the positions of Ng atoms at the structures described above, and the results are shown in Table V. The frequencies of the H–Xe stretching vibration are most strongly affected in the H-side structures, whereas the I-side and bent structures have a very small effect on the H–Xe stretching frequency. For the H-side structures, the blue shifts are observed, and this shift increases with the Ng size, and apparently the order of the frequency (ν(Ar) < ν(Kr) < ν(Xe)) is in disagreement with the experimental results obtained in the matrices. Obviously, larger clusters should be considered for the adequate description, as stated also previously.[6,8]

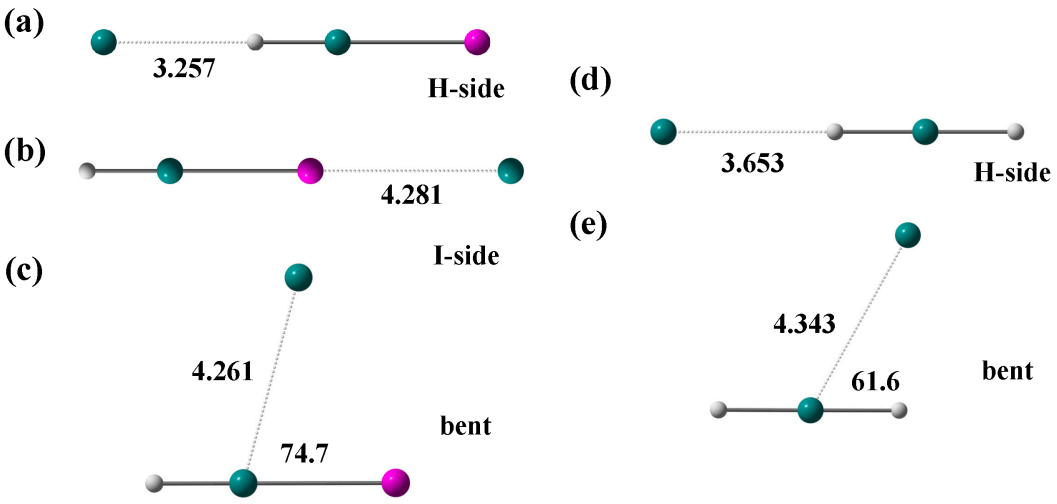

Figure 2. Minimum energy structures of (a-c) HXeI···Xe and (d,e) HXeH···Xe complexes where the internal coordinates of HXeI or HXeH are fixed at the equilibrium values. The bond lengths are given in Å and the angles are given in degrees.

Table III. Structural parameters (r, Å; θ, deg) of the minimum energy structures of the HXeI···Ng and HXeH···Ng complexes (Ng = Ar, Kr, and Xe).

	H-side	I-side	Bent	
	r(Ng···H)	r(I···Ng)	r(Ng···Xe)	θ(Ng···Xe−Y)[a]
HXeI···Ar	3.159	4.091	3.962	75.2
HXeI···Kr	3.180	4.149	4.074	74.7
HXeI···Xe	3.257	4.281	4.261	74.7
HXeH···Ar	3.487	–	4.033	63.9
HXeH···Kr	3.530	–	4.147	62.7
HXeH···Xe	3.653	–	4.343	61.6

[a]Y = I or H

Table IV. Binding energies (kcal mol^{-1}) of an Ng atom (Ng = Ar, Kr, and Xe) to HXeI and HXeH in the 1:1 complexes.

	H-side	I-side	Bent
HXeI···Ar	0.387	0.466	0.821
HXeI···Kr	0.550	0.631	1.055
HXeI···Xe	0.759	0.810	1.286
HXeH···Ar	0.248	–	0.516
HXeH···Kr	0.339	–	0.643
HXeH···Xe	0.436	–	0.761

Table V. Fundamental (anharmonic) frequencies (in cm^{-1}) of the H–Xe stretching frequencies of the HXeI···Ng and HXeH···Ng complexes (Ng = Ar, Kr, and Xe).[a]

	H-side		I-side		Bent	
	Freq.	Shift	Freq.	Shift	Freq.	Shift
HXeI···Ar	1185	+54	1133	+2	1138	+7
HXeI···Kr	1202	+71	1133	+2	1140	+9
HXeI···Xe	1217	+86	1132	+1	1144	+13
HXeH···Ar	1145	+7	–	–	1138	0
HXeH···Kr	1147	+9	–	–	1138	0
HXeH···Xe	1148	+10	–	–	1139	+1

[a]The fundamental frequencies of HXeI and HXeH in vacuum are 1131 and 1138 cm^{-1}, and the frequency shifts from these values are also shown.

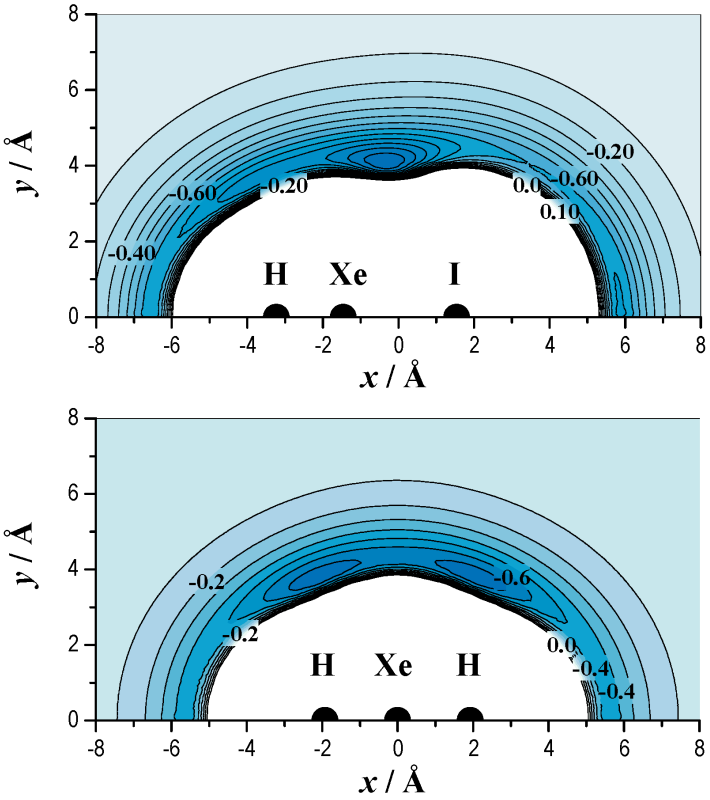

Figure 3. Two-dimensional contour plots of the potential energy surface (in kcal mol^{-1}) for the HXeI···Xe and HXeH···Xe complexes. The internal coordinates of HXeI and HXeH are fixed at the equilibrium values, and the origins are set to the center-of-mass of HXeI and HXeH. The *x* and *y* axes are given in units of Å. For HXeI, the coordinates of the H, Xe, and I atoms are (−3.232, 0.0), (−1.462, 0.0), and (1.539, 0.0), respectively. For HXeH, the coordinates of the H, Xe, and H atoms are (−1.941, 0.0), (0.0, 0.0), and (1.941, 0.0), respectively

6-3-2. HXeI and HXeH in Matrix Environments

Hybrid quantum-classical Monte Carlo simulations were performed for HXeI and HXeH in Ng matrixes. The <110> site is lower in energy for HXeI in all matrices. For HXeH, the <110> site is lower in energy only in an Ar matrix, whereas in Kr and Xe matrices the <100> site is energetically favorable. Table VI shows the peak positions of the H–Xe stretching frequencies calculated for different matrices. In all cases, blue shifts from the frequencies obtained in vacuum are observed. These blue shifts can be attributed to the packing effect by the surrounding Ng atoms, mainly from Ng atoms that are close to the hydrogen atom. The observed shifts are significantly larger than those obtained from the calculations on the 1:1 HXeI···Ng and HXeH···Ng complexes (see Table V). The shifts for HXeI are larger than those obtained previously for HXeCl (+119, +116, and +91 in Ar, Kr, and Xe matrices, respectively).[12]

The contour plots of the two-dimensional distribution functions of Ng (Ng = Ar, Kr, and Xe) atoms around HXeI in the <110> site and HXeH in the <100> sites are shown in Figure 4. Here the *x*-axis is taken as the molecular axis of HXeY and *r* is the radial distance from the *x*-axis. In the same figure, the positions of Ng atoms in the three minimum energy structures of the isolated HXeY···Ng complexes (H-side, I-side, and bent structures) are also shown.

Table VI. Calculated fundamental (anharmonic) H–Xe stretching frequencies (in cm^{-1}) and stabilization energy (in kcal mol^{-1}) of HXeI and HXeH in solid Ng matrices (Ng = Ar, Kr, and Xe). [a]

	<110>				<100>			
	N_r	Freq.	Shift	ΔE	N_r	Freq.	Shift	ΔE
HXeI								
Ar matrix	2	1357	+226	−8.9	2	1278	+147	−5.1
Kr matrix	2	1361	+230	−11.2	2	1277	+146	−4.4
Xe matrix	2	1327	+196	−11.1	1	1414	+283	−3.2
HXeH								
Ar matrix	2	1151	+13	−3.6	1	1190	+52	−3.2
Kr matrix	2	1162	+24	−3.4	1	1177	+39	−4.5
Xe matrix	2	1152	+14	−2.7	1	1154	+16	−5.9

[a] N_r is the number of Ng atoms substituted with HXeI or HXeH. The frequency shifts from the values obtained in vacuum (HXeI: 1131 cm^{-1}, HXeH: 1138 cm^{-1}) are also shown.

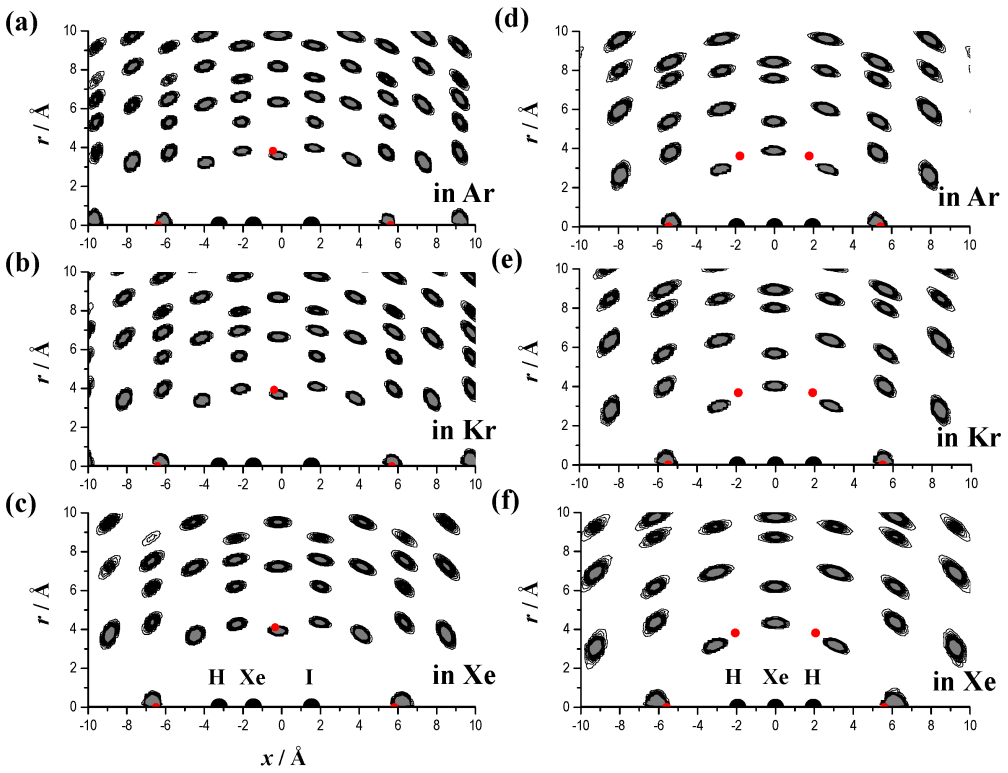

Figure 4. Contour plots of the two-dimensional distribution functions of the Ng atoms around (a-c) HXeI at the <110> site and (d-f) HXeH at the <100> site in the Ar, Kr, and Xe matrices. The *x* and *r* axes are in Å. The positions of HXeI and HXeH are the same as those in Figure 3 (shown by black circles). The positions of the minimum energy structures of isolated HXeI···Ng and HXeH···Ng complexes are shown by red circles.

6-4. Conclusion

I have performed theoretical studies of HXeI and HXeH molecules in Ar, Kr, and Xe matrices. The present calculations successfully describe the main experimental findings. For HXeI, the order of H–Xe stretching frequencies in the <110> (double substitution) site, ν(Xe) < ν(Ar) < ν(Kr), is in accord with the experimental observations, and also the frequency shifts in Ar and Kr matrices from the Xe matrix are well reproduced (experiment: 45 and 46 cm^{-1}; theory: 30 and 34 cm^{-1}). Both in the theory and experiment, the order of these frequencies differ from the case of HXeCl (ν(Xe) < ν(Kr) < ν(Ar));**[12]** thus, the theoretical model is adequate. In addition, the calculations predict for HXeI stronger shifts between Xe and other matrices than for HXeCl,[12] in agreement with experiment.[3,9]

For HXeH, the <100> (single substitution) site is lower in energy only in Kr and Xe matrices. In an Ar matrix, the <110> (double substitution) site is slightly more preferable. If these sites are considered, the order of the vibrational frequency, ν(Ar) < ν(Xe) < ν(Kr), is theoretically obtained, which does not partly agree with the experiments since the highest experimental frequency is observed in an Ar matrix. However, the difference in stabilization energy between the <110> and <100> sites for HXeH in the Ar matrix is relatively small (~0.4 kcal mol^{-1}), compared to those in other matrixes. Therefore, if I assume that the trapping site of HXeH is <100> in all matrixes, the order of frequencies is ν(Xe) < ν(Kr) < ν(Ar), which agrees with the experiments. The frequency shifts obtained in Ar and Kr matrices with respect to a Xe matrix are in quite good agreement with the experiments (experiment: 37.3 and 26.2 cm^{-1}; theory: 36 and 23 cm^{-1}).

The present calculations can explain only the positions of the strongest bands of HXeH whereas the origin of the weaker bands in Xe and Kr matrices are not fully understood. It is tempting to assign the weaker bands to the second matrix sites obtained theoretically; however, this attempt leads to the contradiction with the experimental band positions. I note that the stabilization energy of HXeH in matrices is small due to the weak interaction with surrounding Ng atoms, and therefore, there is the possibility that other trapping sites with similar stabilization energies exit. In fact, in the previous study of HXeCl,[12] the trapping sites that could not be classified by the orientation of the

fcc lattice structure were found although these sites were less stable than the <110> site. If we attempt to assign the weaker bands to other trapping sites, a thorough exploration of the trapping sites is necessary, which is computationally highly demanding. Accurate modelling of matrix sites of HXeH in solid matrices is a challenge for future calculations.

The blue shifts in Ar and Kr matrices with respect to a Xe matrix (~30 cm^{-1}) are obtained in both cases of HXeI at the <110> site and HXeH at the <100> sites. This could partly be explained by the observations that the Ar or Kr atom in the collinear geometry of the H side is found slightly closer to the H atom than that found in the minimum energy structures of the HXeI···Ng or HXeH···Ng complexes whereas the Xe atom is slightly displaced outward (see Figure 4). As stated above in the frequency analysis of the HXeI···Ng or HXeH···Ng complexes, the H–Xe vibrational frequency is strongly affected by Ng atoms that are close to the H atom in the collinear geometry. In this situation, a displacement of the Ng atom toward the H atom results in a blue shift because the potential energy curve is quite repulsive when the Ng atom is located closer to the H atom. A similar explanation was suggested by Kalinowski et al.[9] This effect is due to different sizes of the Ng lattices where the HNgY molecule is accommodated. It follows that the size of the molecule itself can also contribute to the spectral effect. In accord, a different order of the frequencies is obtained here for HXeI in Ar and Kr matrices compared to the previous results on HXeCl. [12]

The present calculations predict blue shifts of the H–Xe stretching frequencies of HXeI and HXeH in the matrices with respect to vacuum. The same qualitative result was obtained previously for HXeCl.[12] The opposite conclusion was obtained by Kalinovski *et al.* for HXeCl (red shift in the matrices with respect to vacuum).[9] I can note here that the PCM calculations predict blue shifts for these molecules in polarizable medium, in agreement with my hybrid quantum-classical simulations.[8] The DFT (B3LYP-D) calculations by Cohen et al. have also featured a blue shift of the H–Xe stretching frequency of HXeBr in a Xe cluster with respect to vacuum.[11] Finally, it is accepted in matrix isolation that the minimal matrix effect (among noble gases) occurs for Ne; [10] thus, the smallest H–Xe stretching frequencies observed for a number of HNgY molecules in Ne matrices (Table I) also suggest blue shifts from the vacuum value for the matrices of the heavier noble gases (Ar, Kr, and Xe). The decisive

conclusion on the sign of this shift can be obtained only after experimental observation of these molecules in the gas phase.

The failure to prepare HXeI in a Ne matrix is worth shortly commenting. I have performed a series of calculations of the stabilization energies of HXeI in different matrices employing only the H−Xe stretching motion (neglecting the bending motions). These calculations result in negative stabilization energies for Ar, Kr, and Xe matrices (from −9 to −11 kcal mol^{-1}), which is similar to the results shown in Table VI. In contrast, the stabilization energy of HXeI in a Ne matrix is positive (about +2 kcal mol^{-1}). This positive value of the stabilization energy may be a reason why this molecule does not appear in the experiments in a Ne matrix. There are additional possibilities for this failure such as intrinsic instability of this molecule and/or a relatively high formation barrier. It should be also mentioned that the calculations in a Ne matrix are difficult because the configurations of Ne atoms around the embedded molecule are rather structureless and the definition of matrix sites is therefore rather vague.

6-5. References

1. L. Khriachtchev, M. Räsänen, and R. B. Gerber, Acc. Chem. Res. **42**, 183 (2009).
2. A. Lignell, and L. Khriachtchev, J. Mol. Struct. **889**, 1 (2008).
3. M. Pettersson, J. Lundell, and M. Räsänen, J. Chem. Phys. **102**, 6423 (1995).
4. M. Pettersson, J. Lundell, and M. Räsänen, J. Chem. Phys. **103**, 205 (1995).
5. M. Lorenz, M. Räsänen, and V. E. Bondybey, J. Phys. Chem. A **104**, 3770 (2000).
6. H. Tanskanen, L. Khriachtchev, J. Lundell, and M. Räsänen, J. Chem. Phys. **125**, 074501 (2006).
7. M. Tsuge, S. Berski, R. Stachowski, M. Räsänen, Z. Latajka, and L. Khriachtchev, J. Phys. Chem. A **115**, 4510 (2012)
8. M. Tsuge, A. Lignell, M. Räsänen, and L. Khriachtchev, J. Chem. Phys. **139,** 204303 (2013).
9. J. Kalinowski, R. B. Gerber, M. Räsänen, A. Lignell and L. Khriachtchev, J. Chem. Phys. **140**, 094303 (2014).
10. M. E. Jacox, Chem. Soc. Rev. **31,** 108 (2002).
11. A. Cohen, M. Tsuge, L. Khriachtchev, M. Räsänen, and R. B. Gerber, Chem. Phys. Lett., **594**, 18 (2014).
12. K. Niimi, A. Nakayama, Y. Ono and T. Taketsugu, J. Phys. Chem. A **118**, 380-387 (2014).
13. A. Nakayama, K. Niimi, Y. Ono, and T. Taketsugu, J. Chem. Phys. **136**, 054506 (2012).
14. K. A. Peterson, D. Figgen, E. Goll, H. Stoll and M. Dolg, J. Chem. Phys. **119**, 11113-11123 (2003).
15. MOLPRO, version 2010.1, a package of *ab initio* programs, H.-J. Werner, P. J. Knowles, G. Knizia, F. R. Manby, M. Schütz, et al.
16. J. Echave and D. C. Clary, Chem. Phys. Lett. **190**, 225 (1992).
17. N. Runeberg, M. Seth and P. Pyykkö, Chem. Phys. Lett. **246**, 239-244 (1995).
18. J. Lundell, G. M. Chaban and R. B. Gerber, J. Phys. Chem. A **104**, 7944-7949 (2000).

19. T. Takayanagi, T. Asakura, K. Takahashi, Y. Taketsugu, T. Taketsugu and T. Noro, Chem. Phys. Lett. **446**, 14-19 (2007).
20. L. Khriachtchev, A. Lignell, J. Juselius, M. Räsänen, and E. Savchenko, J. Chem. Phys. **122**, 014510 (2005).

7. QM/MM-MD study on conformation memory in 193 nm photolysis of formic acid: Excited-state dynamics controlled by the initial electronic state and the cage effect

7-1. Introduction

Remarkable progress in femtosecond laser spectroscopy over the past few decades enables us to directly monitor the nuclear motion of a molecule undergoing chemical reactions[1, 2]. With these techniques, there has been increasing interest in controlling the chemical reactions. Several spectroscopic techniques have already been proposed to realize this aim[3-6], and one of them utilizes the intrinsic molecular feature called conformational memory, where the initial conformer determines the product state. Experimental evidences of conformationally specific photodissociation channels have been reported for gas-phase 1-iodopropane cation ($1\text{-}C_3H_7I^+$)[7] and also for propanal cation ($C_3H_6O^+$)[8-10]. In the former case, the *gauche* and *anti* conformers lead to different $C_3H_7^+$ isomeric products. In order to utilize the features of the conformational memory, selective preparation of isomeric molecules is needed before photo-excitaiton. In the above examples, selective separation of conformers was achieved by utilizing a difference of ionization energies between conformers.

More sophisticated way for the selective separation of comformers is to use the narrowband-IR pumping combined with the matrix-isolation technique[11-20]. The matrix-isolation spectroscopy is widely used to measure various properties of chemical

species at very low temperatures by isolating them in an ideal condition for spectroscopic measurements. [21-23]. The noble-gas atoms are almost exclusively used as a matrix medium, and the inertness of the noble-gas atoms makes them very suitable for the usage of the tunable IR irradiation to selectively excite a specific vibrational mode. This leads to a reaction pathway along the selected mode, thus enabling the preparation of a specific conformer.

Recently, by means of this technique, the conformationally-selective preparation for the formic acid (HCOOH) in Ar matrix have been realized[11-14]. Furthermore, Khriachtchev et al. showed that the photodissociation products revealed the conformation memory[24]. In that experiment, after irradiating two conformers by the UV light (193 nm), the dominant channel was found to be CO + H_2O for *trans*-HCOOH, while it was CO_2 + H_2 for *cis*-HCOOH, and the CO/CO_2 ratios were 5.0 and 0.42 for *trans*-HCOOH and *cis*-HCOOH, respectively. This observation indicated that the photodissociation of HCOOH exhibits the conformational memory.

The detailed mechanism of this process, however, has not been elucidated clearly by theoretical calculations. The molecular dynamics (MD) study on the ground-state (S_0) potential energy surface (PES) showed that the CO + H_2O channel was dominant over the CO_2 + H_2 channel for both conformers. This is because a barrier of *cis-trans* isomerization on the S_0 PES is very small, and therefore the isomerization can easily occur before the dissociation takes places[25, 26]. The surface hopping excited-state MD study in the gas phase after the S_1 excitation starting from the both conformers predicted that HCO + OH is a common dominant product[27], which agrees with the experimental results in the gas phase. However, there is still a quantitative discrepancy in the CO/CO_2 ratio, in contrast to the two cases of 1-$C_3H_7I^+$ and $C_3H_6O^+$ where the theoretical calculations successfully reproduce the experimental findings. In these cases, the excited-state PESs are very characteristic to guide two conformers to different reaction channels.

Very recently, all major reaction pathways of formic acid on S_0, S_1, and the lowest triplet (T_1) PESs have been explored by the automated reaction path search method[28]. It has been shown that the novel pathway originating from the S_2 state exists

for the $CO_2 + H_2$ dissociation channel. In this pathway, after the O-H bond cleavage, the half-dissociated H atom roams around HCOO fragment and attracts the other H atom to form H_2. In this process, one could imagine a non-negligible effect of surrounding Ar atoms in a dynamical picture because the H atom is distant from the remained fragment.

The above considerations imply that the following two factors should be examined carefully to elucidate the mechanism of the conformational memory in HCOOH photolysis in Ar matrix: the initial electronic state and the cage effect from Ar matrix. It has been well recognized that the cage effect plays important roles in the photolysis in noble-gas matrices and sometimes changes the product states depending on noble-gas atoms[21-23, 29-35]. To our knowledge, there have been no theoretical works on the cage effects in the context of conformational memory. In this work, we perform the excited-state QM/MM-MD simulations for the photolysis of HCOOH in Ar matrix and investigate the role of Ar atoms on the conformational memory. In particular, we focus on the reaction starting from the S_2 state since it is a key process for the observation of conformational memory.

This paper is organized as follows. The computational details are given in Sec. 7-2, where the procedure to determine the parameters of the potential energy functions and also the details of QM/MM-MD simulations are provided. The results of the QM/MM-MD simulations are presented in Sec. 7-3. In this section, the possibility of the excitation to the S_2 state is examined first by the ground-state MD simulations for both conformers. Then, the photodissociation dynamics in Ar matrix is studied by the excited-state MD simulations. Finally, conclusions are given in Sec. 7-4.

7-2. Computational details

7-2-1. Determination of the Morse potential parameters for QM/MM simulations.

Before starting the QM/MM-MD simulations, it is necessary to determine the interaction potentials between HCOOH and Ar atoms. In this work, the QM part consists of HCOOH and the surrounding Ar atoms are treated as the MM part. The interaction potential energy between HCOOH and Ar atoms are approximated as a pairwise additive form, where all interactions are decomposed into the atomic-pair interaction and represented as follows.

$$V_{QM/MM} = \sum_{i \in HCOOH} V_{i-Ar} \qquad (1)$$

In order to represent potential energy curves, the functional form of the Morse potential is employed, where it is defined by three parameters (r_e, D_e, a) as follows,

$$V_{i-Ar} = D_e \left[\left\{ 1 - \exp\left(-a\left(r - r_e\right)\right) \right\}^2 - 1 \right] \qquad (2)$$

The parameters are adjusted to reproduce the potential energies obtained by *ab initio* calculations. Specifically, the following procedures are taken. First, an Ar atom is randomly placed in the vicinity of the selected atom in HCOOH and then ab initio calculations are performed at some points along the direction between the selected atom in HCOOH and Ar atom and one-dimensional potential energy curve is obtained. Starting from different configurations of Ar atom and iterating the above procedure, different potential energy curves are prepared. Through least-squared fitting of the averaged one from them, the parameters of the Morse function are estimated.

After obtaining the parameters for all atoms in HCOOH, we notice that the parameters for different O or H atoms are very close to each other, and therefore we use the averaged values for O-Ar or H-Ar interactions. Special care must be taken when the cleavage of the O-H bond occurs. In this event, we find that the parameters for H-Ar is not transferable, and therefore we introduce the switching function to smoothly connect two parameter sets, which is given as

$$V_{H-Ar} = V_{H-Ar}^{HCOOH} + \left(V_{H-Ar}^{solo} - V_{H-Ar}^{HCOOH}\right)\frac{1}{1+e^{-7.0(r_H-2.0)}} \qquad (3)$$

where V_{H-Ar}^{HCOOH} is the interaction potential of H and Ar that is determined from the interaction between HCOOH and Ar. V_{H-Ar}^{solo} is determined from the interaction between an isolated H atom and Ar atom. Here r_H is a distance between H and Ar atom in the simulation.

Regarding the level of *ab initio* calculations, the coupled-cluster singles and doubles including the perturbative contributions of connected triple excitations [CCSD(T)] method is employed and the aug-cc-pVTZ basis sets are used for all atoms. The parameters used in the simulations are listed in Table I.

Table I. Parameters (r_e, D_e, a) of the Morse potential obtained by the fitting of *ab initio* potential energy curves. r_e and D_e correspond to the equilibrium bond length and the well depth of potential energy curve, respectively.

	r_e(Å)	D_e(kJ/mol)	a(Å^{-1})
O-Ar	3.461	-1.942	0.87
C-Ar	3.521	-2.707	0.78
H-Ar	2.829	-2.823	0.88
H_{dis}–Ar	3.611	-0.410	0.77
Ar-Ar	3.800	-1.138	0.88

*H_{dis} stands for a dissociated H atom

7-2-2. Dynamics simulations

The simulations are carried out under the periodic boundary condition and 1372 Ar atoms are first placed in a cubic box with the fcc lattice structure. The length of the unit cell is set to 37 Å, which is adjusted to yield the density of experimental values at the saturated vapor condition (1.77 g/cm^3). The HCOOH molecule is then inserted into this lattice by removing two Ar atoms. A cutoff distance with the half the length of the unit cell is applied to all interactions. Before the dynamics simulations, the Monte Carlo sampling is performed to make initial coordinates of Ar atoms. In this process, the internal coordinates of HCOOH are fixed at the equilibrium values in the gas phase. After equilibrating the system at 100 K, the system temperature is gradually decreased to the experimental temperature of 8 K.

From this configuration, the ground-state QM/MM-MD simulation is next carried out. The initial velocities for HCOOH are determined so that the total kinetic energy amounts to the zero point energy of HCOOH. The initial velocities for Ar atoms are given according to the Boltzmann distribution at 8 K. The Møller-Plesset second-order perturbation (MP2) method with the 6-31+G* basis set is employed for the electronic structure calculations of the QM part (HCOOH). The velocity Verlet algorithm with a time step of 0.5 fs is employed and the ground-state MD simulation is performed for 5 ps. Along this ground-state MD trajectory, the excited-state energies are calculated at every 5 fs, and a total of 1000 configurations are taken for the investigation of vertical excitation energies.

For the excited-state electronic structure calculations, multi-state (MS) complete active space second-order perturbation theory (CAPST2) method is employed. It is already known that the complete active space self-consistent field (CASSCF) method is insufficient to describe the S_2 state accurately[36]. The active space for a reference state-averaged (SA-) CASSCF wavefunction is composed of 8 electrons and 6 orbitals, and the S_0, $S_1[n(O)\rightarrow\pi^*(CO)]$, $S_2[n(O)\rightarrow\sigma^*(OH)]$, and $S_3[\pi(CO)\rightarrow\sigma^*(OH)]$ states (a total of 4 states) are averaged with equal weight. In the subsequent

MS-CASPT2 calculations, the corresponding 4 states are mixed in the perturbation calculations, and it is denoted as MS-CASPT2(8,6) hereafter.

The excited-state MD simulations are performed including the nonadiabatic transitions based on the Tully's fewest switches algorithm[37]. The initial coordinates and velocities are taken from the above-mentioned ground-state MD trajectory, and a total of 100 configurations are picked up with a fixed interval of 50 fs. The excited-state MD simulations are initiated from the S_2 state, and the MS-CASPT2(8,6) method is used for electronic structure calculations. Due to the instabilities in the excited-state energy calculations, the number of mixed states N_{st} is adjusted along the trajectory. Specifically, at first, while the molecule is on the S_2 state, N_{st} is set to 4. After a transition to the S_1 state, and then if the energy difference between S_2 and S_3 becomes larger than a threshold ΔE_{th}, N_{st} is switched to 3. Here we use a threshold value of ΔE_{th} = 200 kJ/mol. Similarly, after a transition to S_0, and then if the energy difference between S_1 and S_2 exceeds ΔE_{th}, we set N_{st} = 2. Also, if the energy difference between S_0 and S_1 becomes larger than ΔE_{th}, we set N_{st} = 1, and this corresponds to the single-state (SS-) CASPT2 method. Furthermore, when the three electronic states (S_0, S_1 and S_2) are degenerated after the O-H bond cleavage, N_{st} is set to 1 after a transition to the S_0 state. This manipulation, though it is tricky, improves the convergence of the electronic structure calculations and also the continuity of the MD trajectory since the inclusion of the higher-lying excited states in the averaging procedure sometimes causes instability. I confirmed that no appreciable discontinuity of the potential energies is found when N_{st} is decreased by this treatment.

In order to evaluate a transition probability along the trajectory, the nonadiabatic coupling vectors are required. At the moment, a module for the analytical evaluation of the nonadiabatic coupling vectors at the CASPT2 level is not available in the current MOLPRO package[38]. Therefore, we employ the efficient numerical scheme proposed by Tao et al.[39] for obtaining the transition probability by additionally performing the electronic structure calculations at slightly displaced points from the MD trajectory. The calculations of the transition probability are performed only when the potential energy difference between the current and adjacent states becomes less than

100 kJ/mol. In this region, the time step for the electronic amplitude is set to 0.05 fs, otherwise 0.25fs.

7-3. Results and discussion

7-3-1. S_0-QM/MM-MD simulations for *cis*-HCOOH and *trans*-HCOOH

Figure 1 shows the S_1 and S_2 vertical excitation energies along the ground-state MD trajectories for both *cis*-HCOOH and *trans*-HCOOH in Ar matrix. The S_1 state corresponds to an excitation from a nonbonding orbital belonging to the O atom to the π*(C=O), while the S_2 states is regarded as an excitation from n(O) to σ*(OH). The photon energy of the radiation field used in the experiment (193 nm, 620 kJ/mol) is also shown in this figure. It is seen that the photon energy is large enough to excite the molecule to the S_1 state for both isomers and that it can also excite *cis*-HCOOH to the S_2 state at some configurations. The S_2 state of *trans*-HCOOH lies about 100 kJ/mol higher than the photon energy.

The vertical excitation energies are calculated at a total of 1000 configurations for both isomers, and we find that for the *cis*-HCOOH the S_2 vertical excitation energy is lower than the photon energy at 138 configurations. On the other hand, no configurations are found for *trans*-HCOOH. From these 138 configurations, we pick up 100 configurations as initial conditions for the excited-state MD simulations from the S_2 state.

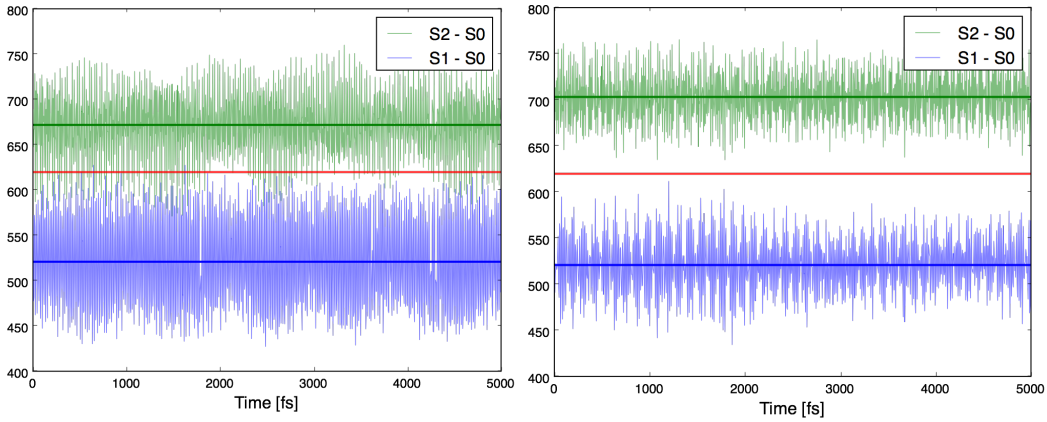

Figure 1. The excitation energy (kJ/mol) for *cis*-HCOOH (left) and *trans*-HCOOH (right) along the trajectory of the dynamics on the S_0 state. The blue and green line indicates the energy necessary to excite HCOOH from S_0 to S_1 and that from S_0 to S_2, respectively. The red horizontal line corresponds to the energy of the radiated light (193

nm, 620 kJ/mol) used in the experiment.

7-3-2. S_2-MD simulations for *cis*-HCOOH

The excited-state MD simulations are performed for *cis*-HCOOH in Ar matrix, starting from 100 different configurations in the S_2 state. In all trajectories, the O-H bond is initially elongated, as expected from the excitation character of the S_2 state, n(O)→σ*(OH).

The trajectories can be categorized into two groups depending on the subsequent structural changes. The first group includes trajectories where the O-H bond is completely broken in the early stage of the dynamics. In this process, the molecule first reaches the region where the S_2 and S_1 states become degenerated, followed by the complete dissociation of the O-H bond where the molecule stays in the S_0 state. (see Figure 2(a)). This group is called "Group A" hereafter and the number of trajectories amounts to 63. In the other 37 trajectories, the O-H bond is not broken. After the deactivation to the S_1 state, some trajectories remain in the S_1 state for a certain time as shown in Figure 2(c), while in the other trajectories the molecule decays to the S_0 state and then the elongated O-H bond shrink back to the equilibrium values, resulting in the original *cis*-HCOOH (see Figure 2 (d) for this process). These 37 trajectories are categorized by "Group B". The difference between "Group A" and "Group B" is whether the O-H bond cleavage occurs or not in the initial relaxation dynamics.

We further continue the classifications of the trajectories based on the subsequent dynamics until 2 ps. In the case of "Group A", after a rapid dissociation of the H atom, the H atom collides with the surrounding Ar atoms. In 38 trajectories out of 63 in "Group A", the H atom roams around the HCOO fragment and then it attracts the other H atom, resulting in the formation of H_2 and CO_2 (this process is illustrated in Figure 2(a) and (b) and details are given below). We group these trajectories to "Group A-a" hereafter. In 16 trajectories out of 63, the dissociated H atom remains as a radical in Ar matrix until 2 ps, and the dissociated products are CO_2 + H + H, and these trajectories are referred to as "Group A-b". In 7 trajectories, the dissociated H atom bounces back to the HCOO fragment, leading to the formation of the original *cis*-HCOOH. These trajectories are tagged as "Group A-c". In addition to those

trajectories, we found two exceptional trajectories. One of which involves a dissociation channel of CO_2 + H_2, where these molecules are formed after the two fragments of HCOO and H react back to HCOOH and then dissociates to CO_2 + H_2 (HCOO + H → HCOOH → CO_2 + H_2). The other one involves the dissociation channel of CO + H_2O. In this process, the HCOO fragment changes its structure to COOH by the translocation of H atom and then it dissociates to CO and OH, followed by the association of OH and dissociated H atom (HCOO + H → COOH + H → CO + OH + H → CO + H_2O).

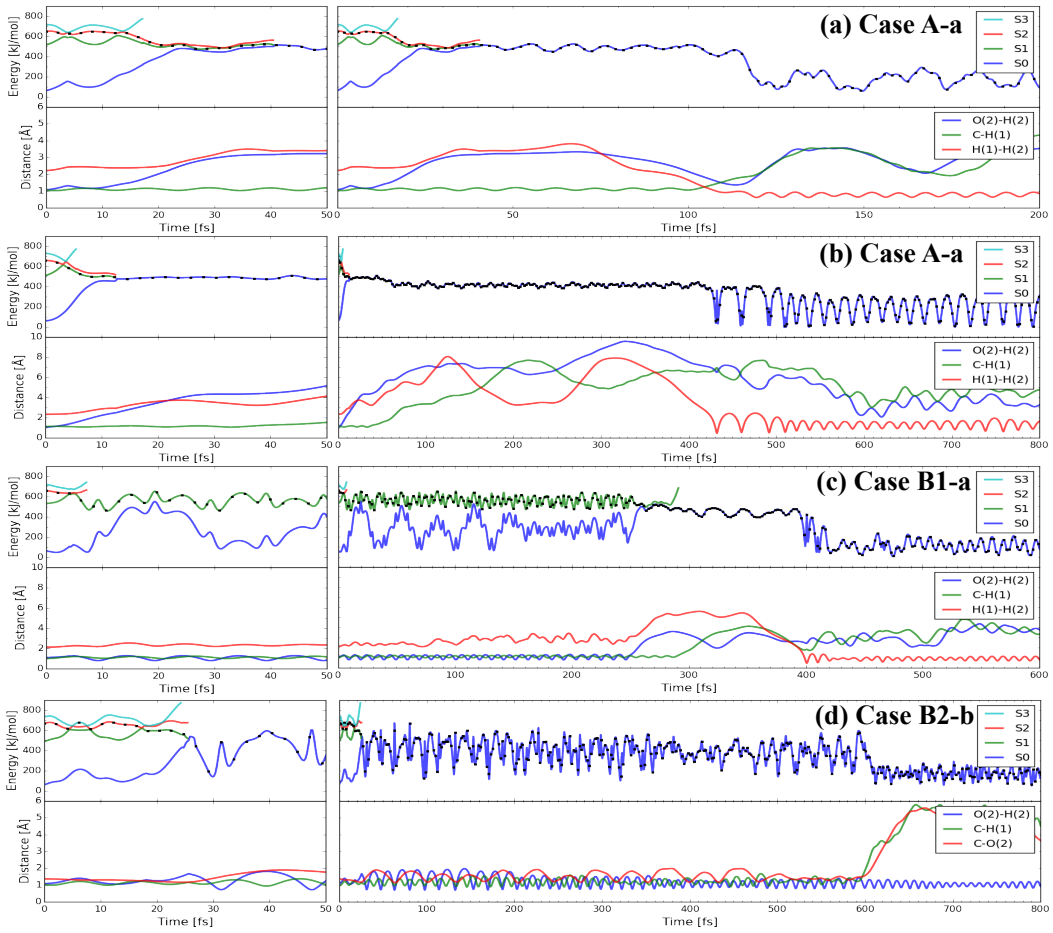

Figure 2. Time evolution of the potential energies of S_0, S_1, S_2 and S_3 state (the upper side) and the bond distances of *cis*-H(1)CO(1)O(2)H(2) (the lower side) just after the S_2 excitation - a typical trajectory for the "Group A-a" ((a) and (b)), the "Group B1-a" (c) and "Group B2-b" (d). The black dots in the potential energy curve indicate the current state of the system. The left box subtracts the dynamics up to 50 fs.

The "Group B" can be further classified into two groups depending on the subsequent dynamics. One group means that the dissociation of the O-H bond eventually happens after HCOOH is deexcited to the S_1 state and stays there for a while, which is called "Group B1". The other is that the dissociation of the O-H bond has never occurred during the simulation and is named "Group B2". The number of trajectories for two cases is 16 and 21, respectively. The "Group B1" is classified in the same manner as the "Group A" and has the further three cases: "Group B1-a" (CO_2 + H_2), "Group B1-b" (CO_2 + H + H) and "Group B1-c" (HCOOH). The number of trajectories for them are 7, 2 and 7, respectively.

The "Group B2" is categorized into two cases: "Group B2-a" means that the structure of HCOOH has been ever retained without the cleavage of any bond and "Group B2-b" indicates the CO + H_2O is produced after the deactivation to S_0. These two cases have 15 and 6 trajectories, respectively. Figure 2(d) illustrates a typical example of "Group B2-b", where HCOOH intramolecularly reacts to CO + H_2O after it is deexcited to the S_0 state about 25 fs and has resides there for long time until around 600 fs. All classifications ever are summarized in Table II and Figure 3.

Table II. Decomposition of groups about the photodeactivation reactions observed in the dynamics simulations of *cis*-HCOOH from the S_2 state. The inside of parenthesis indicates the products when trajectories are categorized.

Group			Trajectory
A (HCOO + H)		A-a (CO_2+H_2)	38
		A-b (CO_2 + H + H)	16
		A-c (HCOOH)	7
		A-d (Exception)	2
B (HCOOH)	B1 (HCOO + H)	B1-a (CO_2 + H_2)	7
		B1-b (CO_2 + H + H)	2
		B1-c (HCOOH)	7
	B2 (HCOOH)	B2-a (HCOOH)	15
		B2-b (CO + H_2O)	6
		Total	100

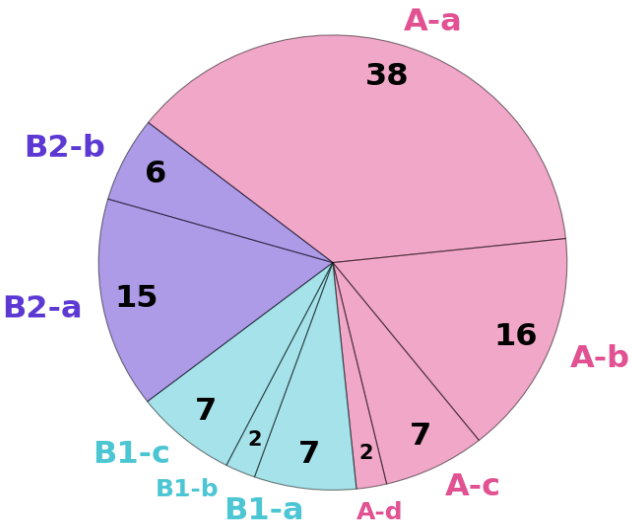

Figure 3. Decomposition of groups about the photodeactivation reactions observed in the dynamics simulations of *cis*-HCOOH from the S_2 state.

All obtained trajectories here can be attributed to the reaction pathways in detailed potential energy profiles presented in the previous literature[28]. Figure 4 shows the simplified version of the reaction route map that includes the critical points, that is, minimum, transition states and minimum energy conical intersections on the S_0 and S_1 state. For all cases, commonly, the formic acid is excited to the S_2 state with its structure distorted from the *cis* equilibrium (signified by the black arrow in Figure 4) and is deexcited to the S_1 state through S_1/S_2-MECI1.

For "Group A", it immediately moves down to the S_0 state through S_0/S_1-MECI1 elongating the O-H bond, resulting in the absolute separation of the H atom. ($S_2 \rightarrow S_1/S_2$-MECI1 $\rightarrow S_0/S_1$-MECI1 $\rightarrow$ HCOO + H). As referred above, "Group B1" also means the H-dissociated structure, however it follows the different route with "Group A": HCOOH reacts to HCOO + H through overcoming the reaction barrier (S_1-TS3) after trapping itself inside the minimum well of S_1 potential energy surface. ($S_2 \rightarrow S_1/S_2$-MECI1 $\rightarrow S_1 \rightarrow S_1$-TS3 $\rightarrow$ HCOO + H).

"Group B2-a" indicates the original structure is maintained. The results of such trajectories show HCOOH has either stayed on the S_1 state until 2 ps or transited to S_0 state on the way, whose trajectories are counted as 10 and 5, respectively.

Furthermore, there are observed two different routes to the S_0 state. On the one way, the molecule follows the same route with "Group A" until reaching S_0/S_1-MECI1, however it goes down to S_0 state without cleaving the extended O-H bonding. ($S_2 \rightarrow S_1/S_2$-MECI1 $\rightarrow S_0/S_1$-MECI1$\rightarrow S_0$-CIS). This process has usually finished soon. On the other, after it has transited to S_1 state through S_1/S_2-MECI1 and stayed there for a while, it has been deexcited to S_0 state through S_0/S_1-MECI2. ($S_2 \rightarrow S_1/S_2$-MECI1 $\rightarrow S_1\rightarrow S_0/S_1$-MECI2 $\rightarrow S_0$-TRANS). Also, such process partially accounts for "Group B2-b", where CO + H_2O is generated through S_0-TS2 after the deactivation to S_0 state.

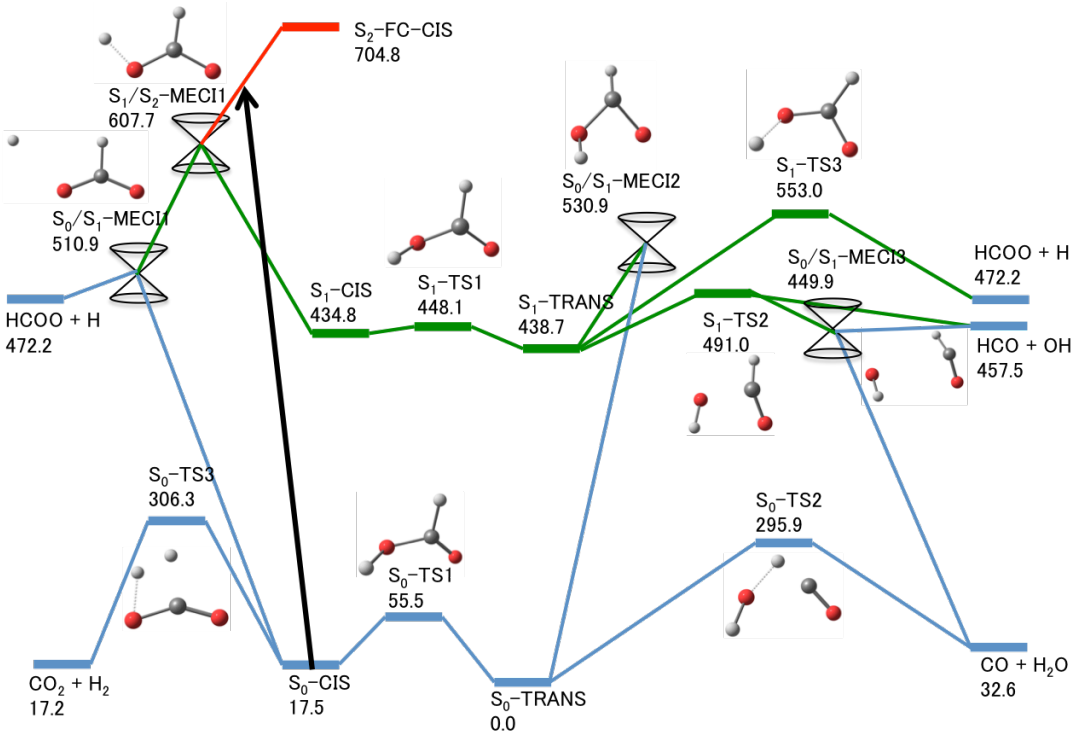

Figure 4. Potential energy profiles for important pathways. Values represent the potential energy (kJ/mol). Connections on the S_0, S_1, S_2 are shown in blue, green and red line. TS and MECI stands for transition state and minimum energy conical intersection, respectively and the image of the structure corresponding to these states are placed nearby.

The consequences of total 100 trajectories obtained by the QM/MM-MD simulations obviously exhibit the excitation to the S_2 state is likely to cause *cis*-HCOOH to cleave the O-H bond, which are found in 79 trajectories ("Group A" and "Group B1"). As shown in the results of the "Group B1" trajectories, this dissociation is

likely to happen on the S_1 state, though it is much less frequently observed in the gas-phase S_1-initiated MD simulations[27]. This is probably because, once the O-H bond is extended close to the dissociation limit during the S_2 stay, the vibration along its stretching mode is so highly excited as to funnel many trajectories into the specific reaction path, in this case, the HCOO + H channel.

The total 46 trajectories from "Group A-a", "Group B1-a" and one of "Group A-d" give CO_2 + H_2 as a final product. Argon matrix plays an important role for this formation. According to Figure 2(a), the H atom is dissociated from the O atom around 10 fs, but by its collision with the near Ar atom, it returns and comes close to the other H atom of the HCOO fragment (see Figure 5), which promotes the cleavage of the H-C bond and simultaneously, the formation of the H-H bond around 110 fs. Such process is named as "Ar-mediated reaction". Also, there is such another way of the H_2 formation that two dissociated H atoms confined inside the cavity shaped by myriad of argon atoms come across and have a bond with each other, which is called "inside-cavity reaction". Figure 2(c) illustrates this process, where the two H atoms connecting with O and C dissociates around 250 fs and 290 fs, respectively and they have drifted inside the cavity until the H_2 is formed at 400 fs. Whereas, the cage effect from Ar matrix is not complete enough to keep all photolysis particles inside the small closed space. Figure 2(b) demonstrates two highly-accelerated H atoms exit out of the cavity, have threaded their ways between argon atoms and finally, the fortunate striking between them results in the formation of H_2 molecule around 400 fs. This type of process is named "outside-cavity reaction". The number of trajectories for "Ar-mediated reaction", "inside-cavity reaction" and "outside-cavity reaction" is 19, 9 and 21, respectively. The cage effect has ever been mainly discussed in the research such as the recombination of alkyl halide or the formation of noble-gas halides in matrix-isolated method. In this research, we discovered the new mechanism for the noble-gas matrix to directly affect the intramuscular reaction process upon the photolysis, which suggests the novel method for regulating chemical outcomes.

There are 18 trajectories representing the CO_2 +H + H channel ("Group A-b" and "Group B1-b"). For all of them, the dissociated H atoms aren't remote over 10 Å away from CO_2. The 29 trajectories indicate the HCOOH channel ("Group A-c",

"Group B1-c" and "Group B2-a"). The CO + H_2O channel appears in 7 trajectories ("Group B2-b" and one of "Group A-d").

Experimentally, the HCO + OH channel is dominant in gas phase but is not observed in matrix-isolated method, which is consistent with our simulation results. Potential energy profiles in Figure 4 indicates that on the S1 state, the generation of HCO + OH is seemed to be more probable path than that of HCOO + H owing to the energy barrier of the corresponding transition state (S1-TS3 vs S1-TS2). For the comparison with the trajectory indicated as "GroupB1-a" in Figure 2(c), we calculated the MD simulation of HCOOH under the same condition but only omitting surrounding noble-gas atoms, where HCO + OH is obtained. This difference of products marks the cage effect of noble-gas matrix has some function either to lower S1-TS3 or heighten S1-TS2, or both. As this reason, we estimated that the separation between HCO and OH cause more significant change of the volume occupied by these fragments than that between H and HCOO and therefore, the cage effect effectively hinder the bulky generation of HCO + OH.

Exceptionally, only one trajectory of "Group B2-a" exhibits HCO + OH is generated once before CO + H_2O is obtained as a final product. However, the H atom of HCO migrates to OH because HCO and OH are not fully separated due to the cage effect. Such a proton transfer under matrix environment was similarly confirmed in the MD simulation for form amide[31]. The summary of the classification depending on the final product is represented in Table III and Figure 6.

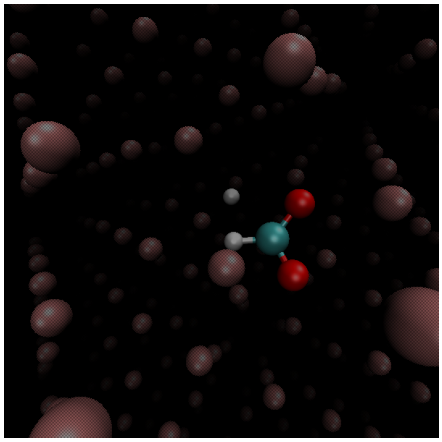

Figure 5. The snapshot at 97.0 fs for the same trajectory in Figure 2(a).

Table III. Decomposition of the final photodeactivation products observed in the dynamics simulations of *cis*-HCOOH from the S_2 state.

Products	Group	Trajectory
CO_2 + H_2	A-a, B1-a, A-d (1)	46
CO_2 + H + H	A-b, B1-b	18
HCOOH	A-c, B1-c, B2-a	29
CO + H_2O	B2-b, A-d (1)	7
	Total	100

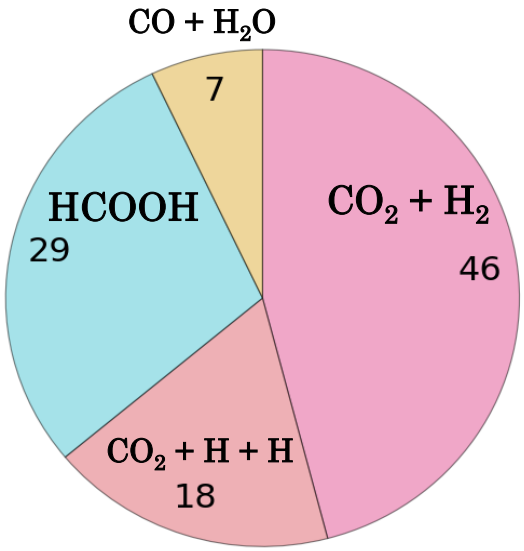

Figure 6. Decomposition of photodeactivation products found at the end of dynamics simulations of cis-HCOOH from the S_2 state.

7-3-3. The ratio of CO/CO_2

Finally, we estimate the CO/CO_2 ratio, particularly for *cis*-HCOOH. Its experimental value is 5.0 for *trans*-HCOOH and 0.42 for *cis*-HCOOH. We have already verified that by the radiation of 193 nm, *trans*-HCOOH is excitable only to the S_1 state but *cis*-HCOOH is both to the S_1 and S_2 state. The excitation probability is linearly dependent on the oscillator strength and the time length of the approachable state. Among 1000 configurations along the S_0-QM/MM-MD trajectory for *cis*-HCOOH, 138 configurations are reachable to the S_2 state, so that they can be regarded as the length of stay on the S_2 state. Because the oscillator strength is proportional to the square of the transition dipole moment, it is calculated as 0.052 $Debye^2$ for the transition from the S_0 state to the S_1 state and 1.310 $Debye^2$ for the transition from the S_0 state to the S_2 state at the optimized structure of *cis*-HCOOH. Therefore, the probability of the excitation to the S_2 state is more than that to the S_1 state by (138*1.310)/(1000*0.05) = 3.62 times. We may assume that the CO/CO_2 ratio for *cis*-HCOOH initiating from the S_1-excitation is as same as that for *trans*-HCOOH and is used as its experimental value, 5.0 because the photolysis of *trans*-HCOOH starts only from the S_1-excitation and the rotational isomerization easily occurs on the S_1 PES. This assumption sounds to be more valid because the S_0-QM-MD simulation reproduces the CO/CO_2 ratio as 5.0 for *cis*-HCOOH and 5.8 for *trans*-HCOOH[25]. The reaction initiating both from the S_0 and S_1 state causes no conformation memory. The CO/CO_2 ratio for *cis*-HCOOH initiating from the S_2-excitation becomes 7/46 by referring to the number of trajectories for both the CO_2 + H_2 and the CO + H_2O channel from the results of S_2-QM/MM-MD simulations. As a result, the CO/CO_2 ratio for *cis*-HCOOH is calculated as follows. Figure 7 helps the readers' comprehension about this estimation.

CO : 3.62 / (1.0 + 3.62) * 7 / (46 + 7) + 1.0 / (1.0 + 3.62) * 5.0 / (1.0 + 5.0) = 0.2839

CO_2 : 3.62 / (1.0 + 3.62) * 46 / (46 + 7) + 1.0 / (1.0 + 3.62) * 1.0 / (1.0 + 5.0) = 0.7161

CO/CO_2 = 0.2839/0.7161 = 0.396

The estimated value is much closed to the experimental one, 0.42. In this, we consider the only trajectories, where the production of CO_2 + H_2 is actually confirmed.

However, there are another 18 trajectories representing the CO_2 product. It is less likely that the diffused H atoms remained trapped into the vacancy of Ar matrix and more likely that they have reaction with the residual fragments or the H atom that comes from another formic acid moving by iterating the tunneling movement.

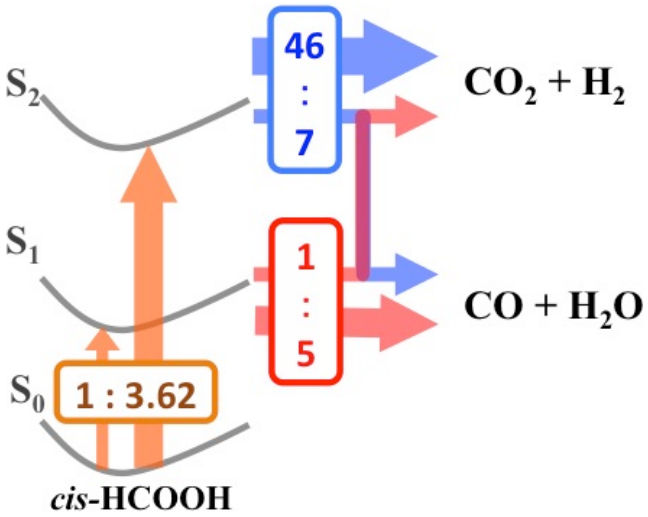

Figure 7. The representative image for the estimation of the CO/CO_2 ratio.

7-4. Conclusions

We performed both the ground state and the double excited state QM/MM-MD simulations and investigated the conformation memory the experiment revealed in the photodissociation of the formic acid in Ar matrix. We calcified the following. The reason for the predominance of the CO_2 + H_2 channel from *cis*-HCOOH is that only *cis*-HCOOH is possible to excite to S_2 by the radiation of 193 nm light. The cage effect from Ar matrix has the significant contribution to the formation of CO_2 + H_2. Among 100 trajectories of the excite-state QM/MM-MD simulation starting from the S_2 state for *cis*-HCOOH, we found 46 trajectories for the CO_2 + H_2 channel. By using this result, we estimated the CO/CO_2 ratio for *cis*-HCOOH and obtained the value of 0.396, which is much close to the experimental value, 0.42.

The mechanism for the conformation memory in this reaction is well explained by the initial electronic state and the cage effect and is entirely different from that in the past examples. To the best of our knowledge, our results in this paper provide the first decisive answer for the origin of the conformational memory in the photodissociation of the formic acid in Ar matrix.

7-5. Reference

1. A. H. Zewail, Journal of Physical Chemistry A **104** (24), 5660-5694 (2000).
2. S. Pedersen, J. L. Herek and A. H. Zewail, Science **266** (5189), 1359-1364 (1994).
3. R. N. Zare, Science **279** (5358), 1875-1879 (1998).
4. N. E. Henriksen, Chemical Society Reviews **31** (1), 37-42 (2002).
5. P. Brumer and M. Shapiro, Annual Review of Physical Chemistry **43**, 257-282 (1992).
6. F. F. Crim, Journal of Physical Chemistry **100** (31), 12725-12734 (1996).
7. S. T. Park, S. K. Kim and M. S. Kim, Nature **415** (6869), 306-308 (2002).
8. M. H. Kim, L. Shen, H. L. Tao, T. J. Martinez and A. G. Suits, Science **315** (5818), 1561-1565 (2007).
9. P. C. Singh, L. Shen, M. H. Kim and A. G. Suits, Chemical Science **1** (5), 552-560 (2010).
10. H. L. Tao, L. Shen, M. H. Kim, A. G. Suits and T. J. Martinez, Journal of Chemical Physics **134** (5), 12 (2011).
11. M. Pettersson, J. Lundell, L. Khriachtchev and M. Rasanen, Journal of the American Chemical Society **119** (48), 11715-11716 (1997).
12. M. Pettersson, E. M. S. Macoas, L. Khriachtchev, R. Fausto and M. Rasanen, Journal of the American Chemical Society **125** (14), 4058-4059 (2003).
13. M. Pettersson, E. M. S. Macoas, L. Khriachtchev, J. Lundell, R. Fausto and M. Rasanen, Journal of Chemical Physics **117** (20), 9095-9098 (2002).
14. E. M. S. Macoas, L. Khriachtchev, M. Pettersson, J. Lundell, R. Fausto and M. Rasanen, Vibrational Spectroscopy **34** (1), 73-82 (2004).
15. M. Rasanen, H. Kunttu and J. Murto, Laser Chemistry **9** (1-3), 123-146 (1988).
16. L. Khriachtchev, J. Lundell, E. Isoniemi and M. Rasanen, Journal of Chemical Physics **113** (10), 4265-4273 (2000).
17. A. K. Knudsen and G. C. Pimentel, Journal of Physical Chemistry **95** (7), 2 823-2832 (1991).
18. J. Pourcin, G. Davidovics, H. Bodot, L. Abouafmarguin and B. Gauthierroy, Chemical Physics Letters **74** (1), 147-151 (1980).

19. S. Coussan, Y. Bouteiller, J. P. Perchard and W. Q. Zheng, Journal of Physical Chemistry A **102** (29), 5789-5793 (1998).
20. S. Sander, H. Willner, L. Khriachtchev, M. Pettersson, M. Rasanen and E. L. Varetti, Journal of Molecular Spectroscopy **203** (1), 145-150 (2000).
21. T. Bally, *Matrix Isolation*. (John Wiley and Sons, London, 2004).
22. H. E. Hallam, *Chapter.4 Infared studies of molecules trapped in low temperature matrices*. (Johan Wiley and Sons, London, 1973).
23. M. E. Jacox, Chemical Society Reviews **31** (2), 108-115 (2002).
24. L. Khriachtchev, E. Macoas, M. Pettersson and M. Rasanen, Journal of the American Chemical Society **124** (37), 10994-10995 (2002).
25. E. Martinez-Nunez, S. A. Vazquez, I. Borges, A. B. Rocha, C. M. Estevez, J. F. Castillo and F. J. Aoiz, Journal of Physical Chemistry A **109** (12), 2836-2839 (2005).
26. H. Y. He and W. H. Fang, Journal of the American Chemical Society **125** (51), 16139-16147 (2003).
27. E. Martinez-Nunez, S. Vazquez, G. Granucci, M. Persico and C. M. Estevez, Chemical Physics Letters **412** (1-3), 35-40 (2005).
28. S. Maeda, T. Taketsugu and K. Morokuma, Journal of Physical Chemistry Letters **3** (14), 1900-1907 (2012).
29. J. Lundell and M. Rasanen, Journal of Molecular Structure **437**, 349-358 (1997).
30. J. Lundell, M. Krajewska and M. Rasanen, Journal of Physical Chemistry A **102** (33), 6643-6650 (1998).
31. M. Eckert-Maksic, M. Vazdar, M. Ruckenbauer, M. Barbatti, T. Muller and H. Lischka, Physical Chemistry Chemical Physics **12** (39), 12719-12726 (2010).
32. A. J. Barnes and Z. Mielke, Journal of Molecular Structure **1023**, 216-221 (2012).
33. V. E. Bondybey, M. Rasanen and A. Lammers, Annual Report on the Progress of Chemistry, Vol 95, Section C: Physical Chemistry **95**, 331-372 (1999).
34. A. I. Krylov and R. B. Gerber, Journal of Chemical Physics **106** (16), 6574-6587 (1997).
35. A. Cohen, M. Y. Niv and R. B. Gerber, Faraday Discussions **118**, 269-280 (2001).

36. J. Novak, M. Malis, A. Prlj, I. Ljubic, O. Kuhn and N. Doslic, Journal of Physical Chemistry A **116** (46), 11467-11475 (2012).
37. J. C. Tully, Journal of Chemical Physics **93** (2), 1061-1071 (1990).
38. MOLPRO, version 2012.1, a package of *ab initio* programs, H.-J. Werner, P. J. Knowles, G. Knizia, F. R. Manby, M. Schütz, et al.
39. H. L. Tao, B. G. Levine and T. J. Martinez, Journal of Physical Chemistry A **113** (49), 13656-13662 (2009).

8. General Conclusions

In this dissertation, I have examined the effects of noble-gas matrices on vibrational spectroscopy and photodissociation dynamics. In order to investigate how the environment of surrounding noble gas atoms affects the vibrational spectroscopy, I have developed a method to estimate the matrix shifts by explicitly taking into account hundreds of noble-gas atoms surrounding an embedded molecule. The simulation results for several noble-gas compounds are in good agreement with the experiments. The present calculations clarified that the amount of shifts depends on the local matrix morphology and that the explicit treatment of surrounding noble-gas atoms is essential to reproduce the experimentally observed matrix shifts.

In Chapter 3, the vibrational spectra of BeO in the Xe and Ar matrices are examined. BeO is known to form a stable Ng-BeO complex (Ng = Ar, Xe) in the noble-gas matrix, and the calculations show that the fundamental frequencies of the Be-O stretching motion upon formation of complex are blue-shifted by 78 cm^{-1} and 80 cm^{-1} for XeBeO and ArBeO, respectively, which are inconsistent with the experimental data. When the effect of other surrounding noble-gas atoms is included, the vibrational frequencies are red-shifted from that of XeBeO complex by 21 cm^{-1} in Xe matrix and by 8 cm^{-1} for ArBeO in Ar matrix. The calculated results are in reasonable agreement with experimental ones, which indicate that the noble-gas matrix can induce nonnegligible shifts in vibrational spectroscopy.

From Chapter 4 to Chapter 6, the vibrational spectra of noble-gas hydrides, HXeCl, HXeBr, HXeI, and HXeCCH, are investigated in noble-gas matrix. The previous experimental reports indicated large matrix shifts due to the large dipole moments and relatively weak bonding of the compounds. It is noteworthy that the unusual trend is observed for the vibrational frequency of the H-Xe stretching motion in

different noble-gas matrices. In the case of HXeCl, HXeBr and HXeCCH, the order of the H-Xe vibrational frequency is ν(Ne) < ν(Xe) < ν(Kr) < ν(Ar), while it is ν(Ne) < ν(Xe) < ν(Ar) < ν(Kr) for HXeI. Apparently, the observed shift is a non-monotonous function of a dielectric constant of the matrix medium. The calculated results reproduce the experimentally observed shifts quite sucessfully, and it is shown that the vibrational frequencies are blue-shifted from the gas-phase values. It is also found that the matrix shifts are $\Delta\nu$(HXeCCH) ≈ $\Delta\nu$(HXeCl) < $\Delta\nu$(HXeBr) < $\Delta\nu$(HXeI) in the same noble-gas matrix, which implies that the weakly bound molecules exhibit large matrix shifts. The noble-gas compound HXeH, which is a subproduct of the formation process of the above-mentioned noble-gas hydrides, is also investigated in a similar manner. It became clear that the vibrational frequencies of HXeH in several noble-gas matrices are also blue-shifted from that of the gas phase, and its order is the same as that of HXeCl. The matrix shift is much smaller than that of the above-mentioned noble-gas hydrides because of its symmetrical structure. The unsual order of the frequency is successfully reproduced by considering the plausible trapping sites of the embedded molecule. The simple calculations neither using the polarizable continuum model (PCM) nor placing a couple of noble-gas atoms around the embedded molecule can explain these orders of vibrational shifts. A realistic modeling of the surrounding matrix environments is essential to describe the unusual matrix shifts accurately.

The results of the simulations reveal that the noble-gas matrix causes the red-shifts of the vibrational frequency of XeBeO and ArBeO, while the blue-shifts are observed for noble-gas hydrides. Such anomalous matrix shifts on vibrational frequencies may be explained by two factors: the charge distribution and the occupied space of the embedded molecule. In the case of XeBeO, the charge of the O atom is substantially negative, and therefore it is dragged by the surrounding noble-gas atoms in its vicinity, which decreases the vibrational frequency of Be-O stretching motion. The Be-O bond does not stretch to the extent that the O atom experiences the repulsion force originating from the adjacent noble-gas atoms. In the case of noble-gas hydrides, only slightly negative charge resides on the H atom. The vibrational wavefunction of H-Xe stretching motion is delocalized due to the light mass of H atom, and therefore it is amenable to the repulsive interactions originating from the surrounding noble-gas atoms. Furthermore, the strengths of packing effects are different depending on the noble-gas

hydrides and surrounding noble-gas atoms, which results in the anomalous order of the matrix shifts.

In Chapter 7, the photodissociation dynamics in matrix environments is theoretically explored. In the photolysis of the formic acid in Ar matrix, the dominant dissociation channel is CO_2 + H_2 for the *cis*-isomer and CO + H_2O for the *trans*-confomer. The results of QM/MM-MD simulations in the electronic ground state indicate that the S_2-excitation is crucial to producing CO_2 + H_2 dominantly and that this channel is only accessible for the *cis*-isomer. The excited-state QM/MM-MD simulations initiated from the S_2 state confirmed the predominance of CO_2 + H_2 over CO + H_2O for the *cis*-isomer. The cage effects of noble-gas matrix has a significant contribution to the production of CO_2 + H_2. Because the dissociated H atom is prevented from diffusion and confined into a small space, it is more likely to collide with each other and react to form an H_2 molecule. The ratio CO/CO_2 is estimated using the simulation results, and it is very close to the experimental result. These results provide the first decisive answer for the origin of the conformational memory in the photodissociation dynamics of HCOOH in Ar matrix.

This thesis is devoted to elucidating the matrix effects on the vibrational spectroscopy and photodissociation dynamics. Since the discovery of the first noble-gas compounds, there has been more interest in the area of noble-gas chemistry. In spite of the high activity in this area, the effects of noble-gas atoms as solvent have not been considered much because it has been assumed that the noble-gas matrix has little effects on the embedded molecule. However, as shown in this work, the noble-gas matrix significantly induces the shift in the vibrational spectra. Also, it can even change the products of photodissociation dynamics. The results presented in this thesis demonstrate that the noble-gas matrix as a solvent should be investigated more than ever both experimentally and theoretically.

Acknowledgment

First of all, I'd like to express my acknowledgements to all members I have shared the time with in the Quantum Chemistry laboratory, including the past and current, students and teachers. Their encouragements and advises helps me so much to conduct the daily research works and to keep my motivation to finish this thesis. The path for the doctorate degree is, in retrospect, the long and tough, which requires ones to fully achieve the research outcomes with both scientific value and novelty. When I had some difficulties in my research, I often went to ask for advisees from teachers and senior students. Without their supports, I can never imagine attaining the Ph.D degree. I also have spent the pleasure time with the members besides the research, for example, chatting idly in the break time, having the regular parties or joining the every-year lab trip. These events last as good and precious ones in my memory. In the following, I leave some remarks particularly on those who I'm owing to in my research.

I would like to represent my sincere gratitude to Professor Tetsuya Taketsugu, the head of the QC lab. Since I belonged there, he has always taken care of my research. Besides this, he has helped me a lot when I prepared my presentation for conferences or wrorte up documents for scientific funds. I have appreciated a great deal for all he has ever done.

I am imbedded to Professor Akira Nakayama, who is the supervisor for my research. The devoted feedback and tolerant advice offered by him makes me finish a couple of themes in my research and submit their papers. The scientific achievements I have ever done since I joined the QC lab and started my research under his guidance are a lot owing to his helpfulness and kindness.

I want to acknowledge Professor Satoshi Maeda. He gave me pertinent remarks on a weekly-based seminar. Moreover, since he hinted a new research topic

around two years ago, I add its result as one chapter of this thesis, which makes my research more meaningful and comprehensive.

I appreciate Professor Takeshi Noro for his invaluable teaching in Quantum Chemistry Theory seminars. For the first year when I joined the QC lab, we held the seminars of reading the introductory textbook with other same-year students. His decent teaching builds up the ground of my understanding in this area.

Finally, I express my appreciation to my father and mother for esteeming my choice to proceed to the doctorate degree. Without their financial and mental supports, it would be impossible to complete this course. I would like to represent my sincere acknowledgement for their priceless cares.